

Radboud University Nijmegen

MASTER THESIS

PTF1108ag
A new eclipsing Red dwarf - White dwarf binary

Author:

J.C.J. VAN ROESTEL

Supervisor:

Prof. Dr. P.J. GROOT

*A thesis submitted in fulfillment of the requirements
for the degree of Master of Science*

in the

Department of Astrophysics



September 2013

Joannes Christiaan Josephus van Roestel
Radboud University Nijmegen
Department of Astrophysics (IMAPP)
Heijendaalseweg 135
6525 AJ Nijmegen
The Netherlands
j.vanroestel@astro.ru.nl

© J.C.J van Roestel, 2013

All Rights Reserved. No part of this book may be reproduced or utilized in any form or by any means, electronic or mechanical, including photocopying, recording, or by any information storage and retrieval system, without permission in writing from the author.

Version: April 2014

Radboud University Nijmegen

IMAPP

Department of Astrophysics

Master of Science

PTF1108ag

A new eclipsing Red dwarf - White dwarf binary

by J.C.J. VAN ROESTEL

Abstract

PTF1108ag is a new eclipsing white dwarf - red dwarf binary star which features a flat-bottom primary eclipse and variation due to reflection. High cadence followup photometry is obtained with Ultracam and the Hale telescope is used to get phase resolved spectroscopy. The combined analysis of this data is carried out in order to determine the system parameters of the binary star. PTF1108ag has an orbital period of $0.10602724 \pm 1.3 \cdot 10^{-7} d$, with measured radial velocities of 85 ± 15 km/s and 215 ± 6 km/s for the white dwarf and red dwarf respectively. The temperature of the white dwarf is 26000 ± 4000 K, which is in agreement with the colors. The red dwarf spectral type is $M4 \pm 1$ and shows some variation on the orbital period. Modeling of the lightcurves with Lcurve allows the relative radii and inclination to be determined. Combined with the radial velocity, the result is a low mass white dwarf, $0.22 \pm 0.03 M_{\odot}$, and a low mass red dwarf, $0.08 \pm 0.02 M_{\odot}$. However, these mass and radii determinations suffer from an unknown systematic error in the radial velocity of the red dwarf due to the reflection effect. In addition, the parameters obtained with the lightcurves suffer from degeneracies. To resolve this higher signal to noise spectra are needed and a better modeling of the reflection effect is required.

Acknowledgements

I would like to thank a number of people how helped and supported me during the course of this research and during the 5 years I studied physics and astronomy at the Radboud University.

First of all I would like to thank my supervisor prof. dr. Paul Groot for his guidance during the master project. His extensive knowledge about observational astronomy and binary stars were a great help during the course of this research. But he also gave me the freedom to explore and make mistakes, which is the best way to learn new skills. I'm also very grateful for the opportunity to visit the Roque de los Muchachos Observatory twice, the Binary summer school in Leuven and the Instrumentation summer school in Toronto. Especially to entrust me with the Isaac Newton Telescope for 7 nights, which were very educational, both professional and personal.

I would also like to dr. David Levitan for the spectra and Thomas Kupfer for his help with the analysis. Thanks to dr. Steven Bloemen for his help with Lcurve and analysis of the photometry and the general feedback about my work. Further, I would like to thank the rest of the astronomy department, especially the binary group, for their useful hints and tips and their feedback about my work. I'm also grateful to prof. dr. P. Groot and prof. dr. F. Verbunt for proof reading my thesis.

This research would not have been possible without the following instruments and programs: computer programs ULTRACAM, Molly and Lcurve by prof. dr. T. Marsh; the instrument Ultracam build by the astronomers and engeneers from of universities of Warwick and Sheffield. The William Herschel Telescope operated by the Isaac Newton Group. The data from the Palomar Transient Factory and the Sloan Digital Sky Survey.

A special mention to my friends, for the laughs and beers we shared; my fellow master students for the warm atmosphere in our office on the 4th floor; and my parents, my brothers and family, for always supporting me when I needed it. Without your help and support I wouldn't be where I am now.

Contents

Abstract	iii
Acknowledgements	iv
1 Introduction	1
1.1 This thesis	1
1.2 Stellar evolution	1
1.3 White dwarfs	4
1.3.1 General characteristics	4
1.3.2 Observations	4
1.4 Red dwarfs	5
1.4.1 General characteristics	6
1.4.2 Observations	6
1.5 Binary stars	8
1.5.1 Theory	8
1.5.2 White dwarf - red dwarf binary evolution	9
1.6 Time keeping	13
2 Methods	15
2.1 Spectra	15
2.2 Lightcurves	16
2.3 Lightcurve fitting: Lcurve	19
3 Data and reduction	23
3.1 Palomar transient factory data	23
3.1.1 Palomar transient factory	23
3.1.2 PTF1108 photometry	24
3.2 Ultracam photometry	24
3.2.1 Ultracam	24
3.2.2 The data	26
3.2.3 Image corrections	26
3.2.4 Aperture photometry	27
3.3 Interloper contamination	28
3.3.1 Calibration	29

3.4 Spectroscopy	31
3.4.1 Double beam spectrograph	31
3.4.2 The data	31
3.4.3 Reduction	33
3.4.4 Wavelength calibration	33
3.4.5 Flux calibration	34
4 Analysis and results	37
4.1 Orbital period and ephemeris	37
4.2 Luminosity and color	40
4.3 White dwarf temperature and red dwarf spectral type and distance	40
4.4 Radial velocity variations	48
4.5 Light curves	54
4.6 Mass and orbital separation	55
4.7 Mass and radius	57
5 Discussion and conclusion	61
5.1 Summary and conclusion	61
5.2 Remaining problems and solutions	62
A ULTRACAM logs	65
B Lcurve	71
 Bibliography	77
List of Figures	77
List of Tables	79
Abbreviations	81
Physical Constants	83

Chapter 1

Introduction

1.1 This thesis

PTF1108ag is a new eclipsing binary consisting of white dwarf and a red dwarf, discovered by the Palomar Transient Factory. The goal of my research is to determine the system parameters of this binary system using high-cadence photometry and phase-resolved spectroscopy.

Chapter 1 gives background information which helps in understanding red dwarf and white dwarf binary stars. A short summary is given of stellar evolution and the structure and characteristics of white dwarfs and red dwarfs are discussed briefly. The general theory of binary evolution is outlined and the evolution of white dwarf red dwarf binary systems is discussed. The last section covers different time standards and their relations, an often overlooked but important subject.

Chapter 2 discusses the methods needed to determine the system parameters of a binary system. Spectroscopy can be used to determine the temperature of both components and allows for a measurement of the velocities. This allows the mass and orbital separation to be determined. The eclipses in the lightcurve can be used to determine the radii of both stars. Lightcurves can show many additional features which are briefly discussed.

Chapter 3 shows the photometry obtained with PTF and Ultracam, and the spectroscopy obtained with the Hale telescope. The data reduction of both the Ultracam data and spectroscopy is explained. The flux calibration of the Ultracam data with a calibration star and stars in the same field of view is shown. The spectroscopy is both wavelength and flux calibrated using the standard procedure using IRAF.

Chapter 4 covers the analysis of the data sets and results. The determination of the orbital period with both PTF and Ultracam data are explained and the results compared. The temperature and spectral type are determined with the spectroscopy by fitting model spectra to the data. The colors of the Ultracam

photometry are compared to models and used as a check. Next, determination of the radial velocity of both stars is explained. Finally the fitting of the results of the lightcurve fits with the Lcurve fitting routine are given.

Chapter 5 discusses the results and shows the mass-radius plots of both the white dwarf and red dwarf. Possible sources of error are pointed out and how these can be resolved in further research.

1.2 Stellar evolution

In figure 1.1 a Hertzsprung-Russel (HR) diagram is shown, which charts stars according to luminosity (L) and effective temperature (T_{eff}). The luminosity is related to temperature and radius:

$$L = 4\pi R^2 \sigma T_{\text{eff}}^4 \quad (1.1)$$

This means that small stars are located on the lower left, and large star are found in the top right. The temperature and radius are related to the total mass, structure, composition of the stars. Since the mass and composition change during the evolution, this plot is a useful tool to track the evolution of a star.¹

Stars are usually born in groups from large clouds, which contract when gravity overcomes the internal pressure. The most important parameter of a star is its mass at birth, which determines the stars further evolution. Stars with a mass of $0.08M_{\odot}$ or more, fuse hydrogen to helium in their core. Stars spend $\sim 90\%$ of their lifetime in this phase and are called 'main-sequence' (MS) stars. main-sequence stars span a large range of different masses, from $\sim 0.08M_{\odot}$ to $\gtrsim 100M_{\odot}$. As can be seen in figure 1.1, the luminosity of main-sequence stars strongly increases with mass ($L \propto M^{3-4}$). This means that more massive stars burn through their hydrogen supply faster, with timescales of a few millions of years, but it takes low-mass stars longer than the age of the universe to burn their hydrogen supply.

When all hydrogen in the core of a star is fused into helium, the core contracts and heat up. This heats up a shell around to core to a high enough temperature to fuse hydrogen. At the same time the outer layers of the star inflates, making the star grow in size, called a red giant (RG). A red giant is a large, but cold star, and thus can be found in the top right of figure 1.1, on the red giant branch (RGB).

The further evolution of the star now depends on its mass. For stars with a mass between $\sim 0.8 - 2.3M_{\odot}$, the helium core becomes degenerate. This means that the main source of pressure is caused by degenerate electrons. This core of degenerate, inert helium, shrinks and slowly gain in mass due to the shell burning. When the core reaches a mass of $\sim 0.48M_{\odot}$, helium fusion starts in the degenerate core resulting in a thermal runaway, called the helium flash². The outer layers of

¹An interactive HRD can be found at <http://www.astro.uni-bonn.de/~javahrd/>

²The helium flash is not visible on the outside as the envelope absorbs all energy.

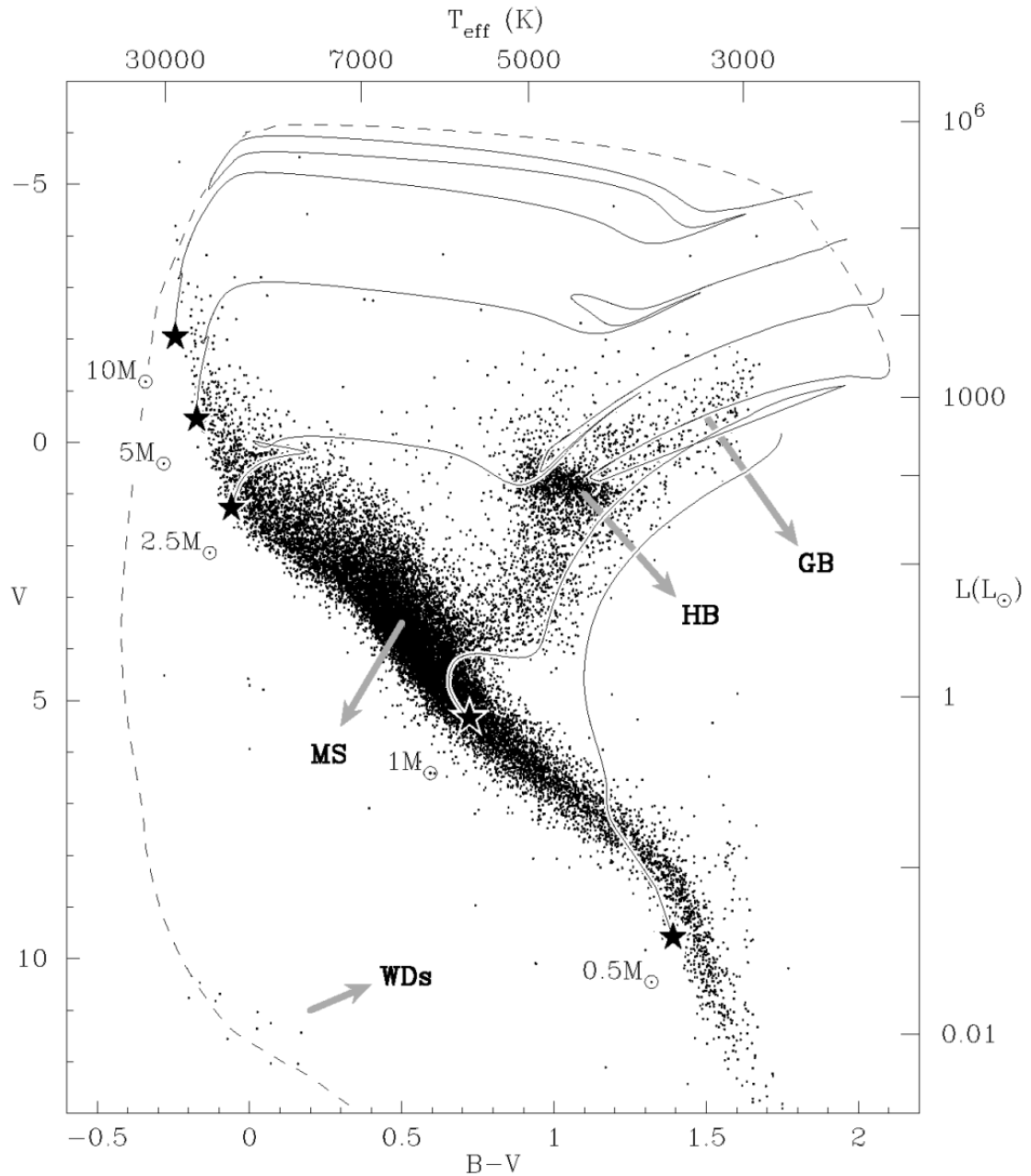


FIGURE 1.1: A Hertzsprung-Russel diagram using Hipparcos data. Effective temperature and color on the horizontal axis and luminosity and V-magnitude on the vertical axis. Indicated are the main-sequence (MS), the Giant Branch (GB), Horizontal branch (HB) and the White Dwarfs (WD). The lines indicate the evolutionary tracks of stars. The dashed line indicates the transition from giant star to white dwarf. Figure taken from van der Sluys [64].

the star shrinks back to a smaller size, moving the star to the horizontal branch (HB) on the HR diagram, stars fusing helium in the core. Stars with a mass between $\sim 2.3 - 9M_{\odot}$ do not go through a stage with a degenerate helium core, but switch to helium fusion calmly.

When all helium in the core is fused into carbon and oxygen, shell burning of hydrogen and helium takes over the energy production. Stars in this stage are found on the asymptotic giant branch (AGB). In this configuration, the helium shell does not burn continuously but only during short intervals. The extinction and re-ignition of the helium shell causes the envelope to pulsate, causing the star to shed its loosely bound envelope due to the high radiation pressure. The ejected material can be observed for a few thousand of years as a planetary nebula. What remains is the inert, degenerate carbon-oxygen core of the star, which is called a white dwarf.

Stars with a mass of $\gtrsim 9M_{\odot}$ are also able to fuse carbon and oxygen, as well as more massive elements. These stars are structured like an onion, with shells of different elements around the core. A problem occurs when the core reaches iron and nickel. Fusing iron and nickel does not produce any energy, and thus the pressure drops. This causes the star to implode, which releases enormous amounts of potential energy, which heats up the outer parts of the star. The star explodes as a supernova and the core either ends up as a neutron star or a black hole.

Stars with a mass less than $\sim 0.8M_{\odot}$ haven't had time yet to evolve from the main-sequence, but when they do, they are not hot enough to fuse helium together. These stars are called red dwarfs, see section 1.4. For a more extended introduction to stellar evolution see Prialnik [49].

1.3 White dwarfs

White dwarfs are the final stage of low-mass stars and are hot and very compact, typical values for mass and radius are $\sim 0.6M_{\odot}$ and $\sim 0.01R_{\odot}$ (Kepler et al. [25], Shipman [58]). White dwarfs do not produce any energy, but only radiate away their thermal energy, slowly cooling down. In this section the structure and observational characteristics of white dwarfs are discussed.

1.3.1 General characteristics

Since a white dwarf does not produce any energy in the core, the ideal gas pressure is insufficient to keep the star from collapsing. The reason that it does not collapse and form a black hole is due to the degenerate electron pressure. This pressure is a result of the Pauli exclusion principle: identical particles cannot occupy the same quantum state. The core of a white dwarf is a plasma of nuclei and free electrons. The free electrons (which are fermions) thus cannot occupy the quantum state of another electron. In a dense environment, electrons gain a higher momentum to

comply with the exclusion principle. These electrons thus have a high velocity (on average), which produces the pressure needed to counter gravity. For a derivation see Prialnik [49, appendix:B]

Degenerate matter has some interesting properties. One is that the pressure does not depend on temperature. White dwarfs are born with a temperature of $\sim 100000\text{K}$ and quickly cool down to lower temperatures. Most observed white dwarfs have an effective temperature between $\sim 10000\text{K}$ and $\sim 30000\text{K}$. Since the degenerate pressure does not depend on temperature, the radius of these white dwarfs does not depend on the temperature. However, white dwarfs have an atmosphere of ideal gas, which does increase in size with temperature. This effect is most important for the low-mass white dwarfs ($0.4M_{\odot}$) and white dwarfs with a thicker outer layer. For a comparison between different white dwarf models, see Panei et al. [44].

What determines the radius is the mass of the white dwarf. For more massive white dwarfs the gravitational pressure on the core increases, which forces the particles closer together. The result is that the radius of degenerate matter decreases with mass, $R \propto M^{-1/3}$. The pressure of the electrons is determined by their velocity, and for a high enough velocities relativistic effects start to play a role. This limits the maximum pressure, and thus sets an upper limit to the mass of a white dwarf, the Chandrasekhar limit, which is $1.44M_{\odot}$. White dwarfs which obtain a mass more than this limit, either by accretion or a merger, explode in a supernova Ia (SNIa), for further information see Nomoto et al. [41].

Despite its importance, the mass-radius relation is not well tested. An example of the mass-radius relation of white dwarfs is given in figure 1.2. Testing the mass-radius relation suffers from multiple problems. Although white dwarfs are very numerous, they are difficult to study because they are very faint. To determine an accurate, but above all, independent mass and radius of white dwarf is extremely difficult. Another problem is that it is not possible to determine the core composition of white dwarfs. Most of the white dwarfs are CO white dwarfs, but if a star loses its outer envelope at a different stage of evolution, helium or neon white dwarfs can be formed. See Panei et al. [44] for a comparison between the different core types.

1.3.2 Observations

What can we learn from observations of white dwarfs? The spectrum of white dwarfs peaks in the blue/UV and has strong, wide absorption lines of hydrogen and/or helium. By comparing overall shape of the spectrum and the absorption lines, the temperature and the surface gravity can be determined. If the spectrum is calibrated, the total flux per wavelength is also known. A more difficult parameter to determine is the distance to the white dwarf. This can be done using the parallax method, but this is only possible for bright, close by white dwarfs. The satellite Hipparcos used this method to determine the distance to ~ 20 nearby white dwarfs. Other distance determinations are possible using stars close to the

white dwarf, like wide binary stars or common proper motion stars, but the distance is difficult to determine. The data points in figure 1.2 use one of these distances to determine the mass and radius of the white dwarf.

If all these parameters are known, they can be used to calculate the mass and radius of the white dwarf, using equation 1.2 and 1.3

$$R = \sqrt{\frac{FD^2}{\sigma T_{eff}^4}} \quad (1.2)$$

$$M = \frac{gR^2}{G} \quad (1.3)$$

The major problem with this method is the dependence of the mass and radius determination, since the calculation of the mass requires a radius. A second problem is the clustering of white dwarfs at $0.6M_\odot$. White dwarfs with a higher or lower mass are rare. In figure 1.2, only one white dwarf has a mass more than $0.8M_\odot$, Sirius B, only 2.6 parsec away (Liebert et al. [34]). Other problems are the unknown core composition and thickness of the outer envelope. These are both not observable, and one has to guess the composition and envelope thickness. See Panei et al. [44] for a comparison between different white dwarf models. For an in depth discussion about measuring white dwarfs masses and radii see Holberg et al. [22].

1.4 Red dwarfs

Red dwarfs are low-mass main-sequence stars which are very faint and live very long. This section discusses the characteristics and the observational features of red dwarfs.

1.4.1 General characteristics

Red dwarfs are the most abundant type of stars in the Galaxy, and contain most of the mass in stars. A census of stars in a 33 pc radius around the sun showed that red dwarfs outnumber all other stars by a factor of three to one (see Lepine [33]). However, they are very faint with $L = 0.0072 - 0.00015L_\odot$, and thus difficult to study. The nearest red dwarf, Proxima Centauri, is only one parsec away, but is already ~ 100 times too faint to be seen by naked eye.

Red dwarfs are grouped historically by presence of TiO emission lines in optical spectrum, with the upper boundary an M0 red dwarf³ corresponding to a $\sim 0.6M_\odot$ star (Kirkpatrick et al. [26]). The lower mass boundary for red dwarfs is set by the hydrogen burning limit. Objects with a mass lower than $\sim 0.08M_\odot$ are not

³Sometimes K5 is used as an upper boundary as this already shows TiO lines in the IR

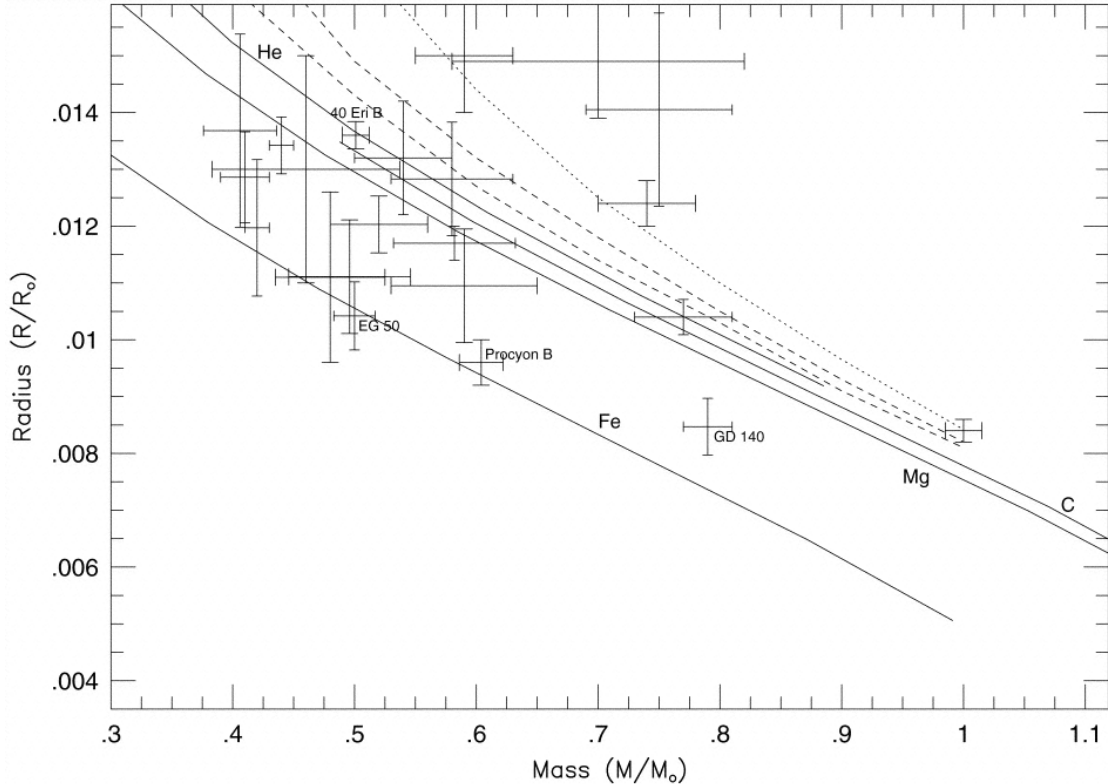


FIGURE 1.2: The mass-radius relation of white dwarfs. The points indicate white dwarfs from the Hipparcos catalog and white dwarfs with a known distance from wide binaries and common proper motion stars. The lines are white dwarf models with different core compositions. From Provencal et al. [50].

massive enough to burn hydrogen, and are called brown dwarfs. Typical values for the mass, radius and temperature of red dwarfs can be found in table 1.1. Note that these values should be regarded as a guideline; a study to determine the relation between mass, temperature and spectral type by Baraffe and Chabrier [3] show large uncertainties in the relation.

The structure of red dwarfs is different than that of the sun. The sun has a small outer layer which is convective, while the rest is radiative. The size of the convective zone increases for lower mass stars, with red dwarfs with a mass smaller than $\sim 0.3M_{\odot}$ are fully convective. For stars more massive than $\sim 0.2M_{\odot}$ the internal pressure is dominated by the ideal gas law for a combination of ions and electron. This results in a mass radius relation of $R \propto M$. But for lower mass red dwarfs the equation of state gets more complex, as partial electron degeneracy and partial ionization have to be taken into account. For an overview of the structure of low-mass stellar objects see Chabrier et al. [11].

TABLE 1.1: Stellar parameters for M-dwarf spectral types. Note that significant deviations are observed, so these values should be used as a guideline only. From Reid and Hawley [53] (quoted from [24]).

Spectral type	Mass [M_{\odot}]	Radius [R_{\odot}]	Luminosity [L_{\odot}]	T_{eff} [K]
M0V	0.60	0.62	0.072	3800
M1V	0.49	0.49	0.035	3600
M2V	0.44	0.44	0.023	3400
M3V	0.36	0.39	0.015	3250
M4V	0.20	0.26	0.0055	3100
M5V	0.14	0.20	0.0022	2800
M6V	0.10	0.15	0.0009	2600
M7V	0.09	0.12	0.0005	2500
M8V	0.08	0.11	0.0003	2400
M9V	0.075	0.08	0.00015	2300

1.4.2 Observations

Because red dwarfs are relatively cool, metal molecules can form in the atmosphere. These metal molecules are visible in absorption lines in the spectra, of which the most prominent are TiO, VO and H₂O and with hydrogen metals like CaH, FeH and MgH. In addition to these molecular lines, Fe, K and H lines are also visible. The molecular lines dominate the whole spectral range, making it difficult to determine the black body continuum.

The current method of classifying red dwarf uses a combination of the molecular lines and the overall shape of the spectrum, see Kirkpatrick et al. [26]. The spectral type thus only says something about how the spectrum looks like (the overall shape and emission/absorption lines), and nothing (directly) about the physical parameters of the star. For most main-sequence stars the spectral type is linked one-to-one with temperature, luminosity, mass and radius (for main-sequence stars). The sun for example, a G2V star, has a similar temperature, luminosity, mass and radius as other G2V stars. However, for red dwarfs there is a considerable scatter between spectral type and luminosity/temperature (Chabrier and Baraffe [10]).

Observations of red dwarfs show many discrepancies between models and measurements. The radius of many red dwarfs seems to be higher than models predict, up to 20%, see figure 4.21. The effective temperature on the other hand seem to be overestimated, see Fernandez et al. [19], Morales et al. [38], Ribas et al. [55]. A theory to explain this is a high rotation rate or large magnetic field of the star which would reduce large scale thermal convection in the core. Active stars also feature more cool stars spots, which could also decrease the temperature and increase the radius, see Chabrier et al. [12], Kraus et al. [30]. To resolve the issue, accurate measurements of stellar parameters of many red dwarfs are needed.

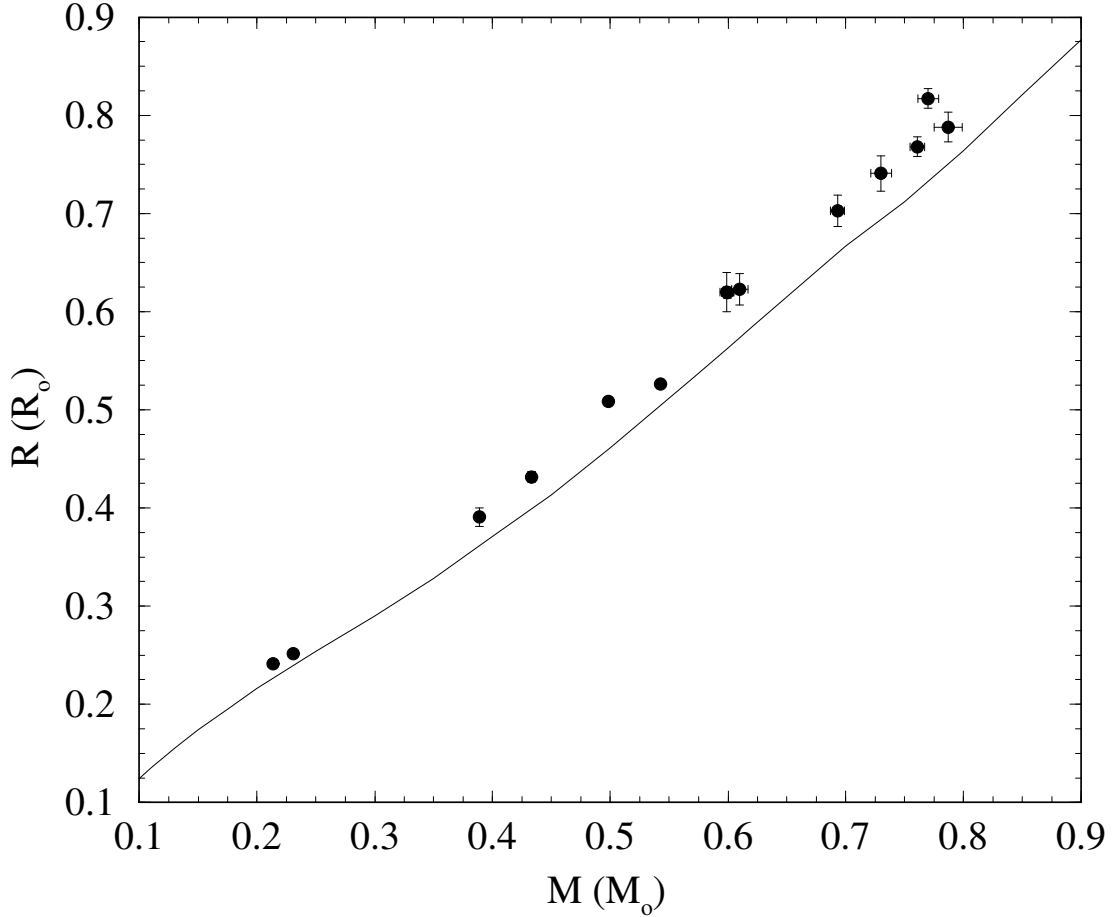


FIGURE 1.3: The mass radius relation for red dwarfs in binary systems. All measurements are consistently higher than the model prediction. Figure taken from Ribas et al. [55].

Red dwarfs have gained a lot of (observational) attention in recent years because of potential habitable planets. Observational benefits are deeper transits compared to larger stars and shorter orbital periods for planets in the habitable zone. Radial velocity measurements of the star induced by the planet are also larger, and thus easier to detect. However, to characterize a planet accurately, the stellar parameters need to be known with high precision. For example the transit method, which is also used by the Kepler satellite, uses assumptions about the stellar mass and radius to determine the planet parameters (e.g. radius, orbital distance).

1.5 Binary stars

Stars are born from giant molecular cloud in groups of thousands or more. While the cloud is collapsing, it fragments, each fragment forming a star. Stars born from these fragments have the same age, and if close enough, are bound by gravity and revolve around a common center of mass. The number of stars which are part of

a binary is a significant fraction, 50% of the stars in our Galaxy are thought to be part of a binary (Abt [2]). This section discusses the evolution and observations of binary stars.

1.5.1 Theory

The angular frequency (ω) or orbital period (P), the mass of both components (m_1, m_2), and the orbital separation (a) of the binary system are related by Kepler's third law:

$$\omega^2 = \left(\frac{2\pi}{P}\right)^2 = \frac{G(m_1 + m_2)}{a^3} \quad (1.4)$$

With G the gravitational constant. For a binary star with masses of $m_1 = m_2 = 1M_\odot$ and a period of 1 day the separation is $a \approx 4R_\odot$.

If the stars are far apart, they can be regarded as two separate stars evolving at their own pace, moving through the Galaxy together. For stars that are closer together, accretion of wind from the companion can become important. Stars even closer feature more severe interactions can take place and can drastically alter the evolution of the stars.

An important concept in binary star structure and evolution is the Roche potential, the gravitational potential in the co-rotating frame. The Roche potential approximates the two stars as point masses in a rotating frame with an angular velocity given by equation 1.4, resulting in a potential given by equation 1.5.

$$\Phi(\mathbf{r}) = -\frac{Gm_1}{|\mathbf{r} - \mathbf{d}_1|} - \frac{Gm_2}{|\mathbf{r} - \mathbf{d}_2|} - \frac{1}{2}|\boldsymbol{\omega} \times \mathbf{r}|^2 \quad (1.5)$$

With \mathbf{r} the distance to the center of mass, $m_{1,2}$ the mass of the stars and $\boldsymbol{\omega}$ the angular frequency vector. This formula can be rewritten into dimensionless form, only depending on the mass ratio $q \equiv (m_2/m_1)$.

$$\Phi_n(\mathbf{r}) = \frac{2}{(1+q)} \frac{1}{|\mathbf{r} - \mathbf{d}_1|} + \frac{2q}{(1+q)} \frac{1}{|\mathbf{r} - \mathbf{d}_2|} + x^2 + y^2 \quad (1.6)$$

The quantity $\Phi_n = -2\Phi/G(m_1 + m_2)$, the normalized potential, \mathbf{d}_1 and \mathbf{d}_2 are distances of the stars to the center of mass, normalized to the separation a . This shows that the shape of the Roche potential depends only on the mass ratio q , and can be scaled to the appropriate size. An example of what such a potential looks like is shown in figure 1.4. Important points in this potential are the Lagrange points, which indicate positions where the potential is flat.

If the stars are small relative to their Roche lobe, the shape of the star remains spherical. However, stars that are comparable in size to their Roche lobe get deformed, and are pear-shaped. If one star is too large for its Roche lobe and the other star is small, mass can flow from one star to the other. This stream of mass is deflected by the Coriolis force as it moves to the accreting star and can form

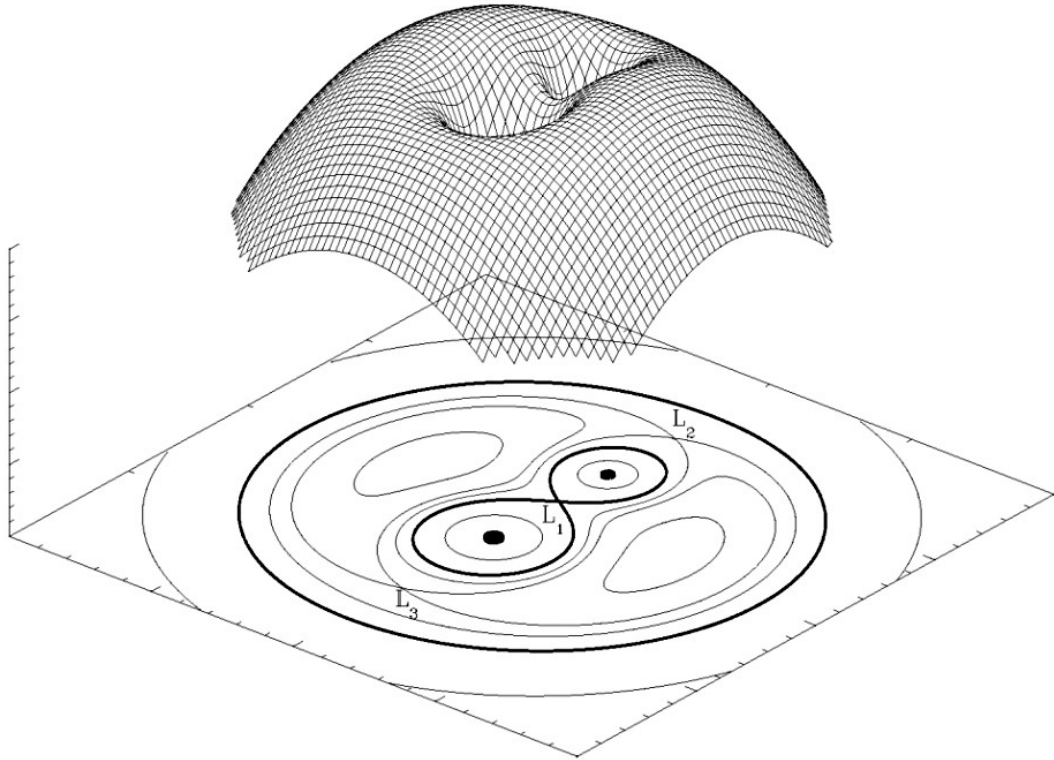


FIGURE 1.4: An example of the Roche potential. The inner-Lagrange points are indicated by an 'L'. Courtesy of M. Heemskerk

an accretion disk. It is also possible that both stars are too large for their Roche lobes, forming a single peanut shaped star. These different types of binaries are called detached, semidetached and contact binaries.

For further discussion, it is useful to define an effective radius of a Roche distorted star. This effective radius is defined as the radius of spherical star with the same volume as the filled part of Roche lobe. The critical effective radius, 'Roche radius', as function of $q = m_2/m_1$, can be approximated with equations 1.7 (Eggleton [18]) and 1.8 (Paczyński [43]).

$$\frac{R_L}{a} \approx \frac{0.49q^{2/3}}{0.6q^{2/3} + \ln(1 + q^{1/3})} \quad 0 < q < \infty \quad (1.7)$$

$$\approx 0.46 \left(\frac{q}{1+q} \right)^{1/3} \quad 0 \lesssim q \lesssim 0.8 \quad (1.8)$$

The first equation is accurate to 1% for all q , the second equation is less accurate, but more convenient analytically. For example, it can be used to estimate the maximum size of a star which fits in the Roche lobe as function of orbital period, the critical orbital period. This is done by combining equations 1.8 with 1.4, and assuming a mass-radius relation of the donor. For low-mass stars, $R/R_\odot \approx M/M_\odot$,

which results in the relation shown in figure 1.5. This already sets a limit for the size of the star for a certain orbital period.

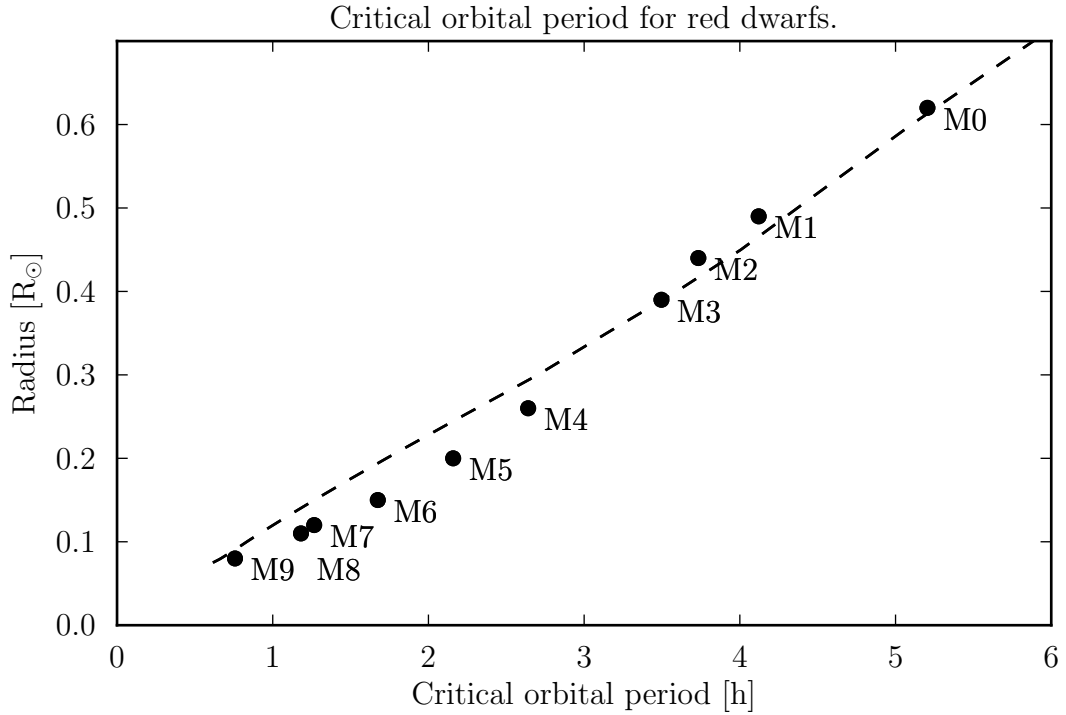


FIGURE 1.5: The maximal radius of secondary as function of critical period for a primary mass of $0.6M_{\odot}$. The line indicates the critical period assuming the mass radius relation for red dwarfs from Baraffe et al. [4]. The dots shows the critical orbital period using the data from table 1.1.

1.5.2 White dwarf - red dwarf binary evolution

As already explained in section 1.3, white dwarf stars are the result of an AGB star which has lost its envelope. Close white dwarf - red dwarf binary stars are only a few solar radii apart, while a AGB star can be as large as $1000R_{\odot}$. This must mean that some interaction must have taken place.

Short period white dwarf - red dwarf binaries start out as a main-sequence star, with an initial mass $M_{1i} \gtrsim 5M_{\odot}$, and a red dwarf. As explained in section 1.2, the more massive star evolves faster. When the massive star becomes a red giant it increases its radius to about $\sim 100R_{\odot}$, and to $\sim 1000R_{\odot}$ when in the AGB phase. Depending on the distance of the red dwarf, it will overflow its Roche lobe in one of these stages. The mass loss of a giant star to a low-mass red dwarf is unstable and keeps accelerating. On the other hand, the red dwarf cannot cool fast enough to accrete all the matter, which piles up on the surface. The result is that a common envelope is formed.

Due to the interaction by the envelope and the red dwarf, the envelope is ejected while the red dwarf spirals inward. This phase lasts only a few thousand years and no binary has been observed in this state. Despite the importance of this stage in binary evolution, it is not understood. The problem is that a lot of different physics is important over different timescales, making it impossible to models correctly. For an extensive review about common envelope evolution see Ivanova et al. [23].

The result of the common envelope phase is a white dwarf and a red dwarf in a very close orbit, called a post common envelope binary (PCEB). The composition of the white dwarf depends on when the common envelope occurred. If the common envelope occurred during the red giant phase, the white dwarf is a helium white dwarf. The mass of this helium core white dwarf can be anywhere between $0.27M_{\odot}$ to $0.46M_{\odot}$, depending on the initial mass. If the Common Envelope occurs during the asymptotic giant branch, the white dwarf has a CO-core, with a mass of at least $0.54M_{\odot}$, up to the Chandrasekhar mass, see Politano [48].

The results is a binary in a very close orbit, $a \approx R_{\odot}$. Tidal effects are strong, which has two results. The orbit of the binary gets circularized; the eccentricity goes to zero. The second effect is that the rotation period of the stars becomes the same as the orbital period. An example of this is the moon, which has an orbit and rotation period 27.3 days. The timescales involved are given by equations 1.9 and 1.10.

$$\tau_{sync} \approx 10^4 \left(\frac{1+q}{2q} \right)^2 P^4 \text{ yrs} \quad (1.9)$$

$$\tau_{circ} \approx 10^6 q^{-1} \left(\frac{1+q}{2q} \right)^{5/3} P^{16/3} \text{ yrs} \quad (1.10)$$

The orbital period P is given in days, and is a strong factor in the timescale. For an orbit of a few hours, both timescales less than one year. This shows that the assumption of a circular, zero eccentricity orbit likely to be valid. Taken from Hilditch [21, p.153].

On longer timescales, the orbit of the binary slowly decreases. The most important angular momentum loss mechanism for wider ($P > 3h$) binaries is magnetic braking, see Rappaport et al. [51]. This process removes angular momentum from the binary by forcing the wind to co-rotate with the red dwarf. The particles in the wind carry away a large amount of angular momentum from the rotation of the red dwarf. Since the rotation period and the orbital period are linked, the orbital period decreases. The magnitude and change as function of orbital period for this process is highly unknown. Many different prescriptions exist, with differences in magnitude of 10^4 , see Knigge et al. [28, p.8] for an overview.

The second mechanism is gravitational radiation, important for the close binaries. Gravitational wave are created due to the quadrupole moment of the binary, and carry away energy and angular momentum. The amount of energy carried away is small, with the timescale given in equation 1.11.

$$\tau = \frac{E}{\dot{E}} \simeq 150 \cdot 10^6 \frac{a^4}{(M_1 + M_2)(M_1 M_2)} \text{ yrs} \quad (1.11)$$

This decrease in orbital separation decreases the Roche lobe of both stars. At some point the red dwarf overfills its Roche lobe and starts to transfer mass to the white dwarf, and the binary is then called a cataclysmic variable (CV). If mass is transferred from a low-mass star to a higher mass star, the orbital separation increases, as mass is moved closer to the center of mass. However, this effect is negated by the angular momentum loss caused by the magnetic braking, resulting in a stable mass transfer. The red dwarf loses mass on timescales similar to the thermal timescale, the time a star needs to adjust its temperature. The result is that the star is slightly inflated (up to 20%), due to a too high temperature for its mass.

The red dwarf continues to lose mass, and when it reaches $0.3M_{\odot}$ (corresponding to an orbital period of ~ 3 hours, see 1.5), the red dwarf becomes fully convective. This disrupts the magnetic field, which is critical to the magnetic braking. The orbital separation of the binary does not decrease anymore, and the mass transfer stops. This causes the star to shrink back to a smaller radius, which was inflated by about 20%, see figure 1.6, taken from Knigge et al. [28]

The binary separation now only shrinks due to gravitational radiation and the red dwarf is again smaller than the Roche lobe. When the orbital period reaches an orbital period of 2 hours, the Roche lobe is again too small to accommodate the red dwarf, and mass transfer resumes. This process continues until the red dwarf becomes too small to burn hydrogen, at an orbital period of $P \sim 80$ minutes. When this happens the red dwarf increases rapidly when losing mass. To accommodate this rapid expansion the binary separation starts to grow again. The final fate of these binaries are a white dwarf - brown dwarf binary with an orbital period in the order of a 1-2 hours, called Period Bouncers. An overview of the size of the secondary versus the mass is given in the upper panel of figure 1.6, see for a full review Knigge [27] and Knigge et al. [28].

The result of this mechanism is that there are a few white dwarf - red dwarf with orbital periods between 2-3 hours which transfer mass, and an excess of non-transferring binaries. The former has indeed been observed and is called the Period Gap and is a corner stone of the physics of cataclysmic variables and magnetic braking. There are however reasons to be skeptical about the period gap. Cataclysmic Variables are generally found because they feature outbursts like novae, explosion of accreted matter on the white dwarf, and dwarf-novae, brightening of the accretion disk due to instabilities. The occurrence of these fusion instabilities is linked to the accretion rate, which again depends on the orbital separation. This could cause a selection effect, with short period Cataclysmic Variables being found by dwarf-novae outbursts, while the longer period systems are found due to dwarf-novae outbursts. This could also result in a lack of systems between 2-3 hours, see e.g. Verbunt [67].

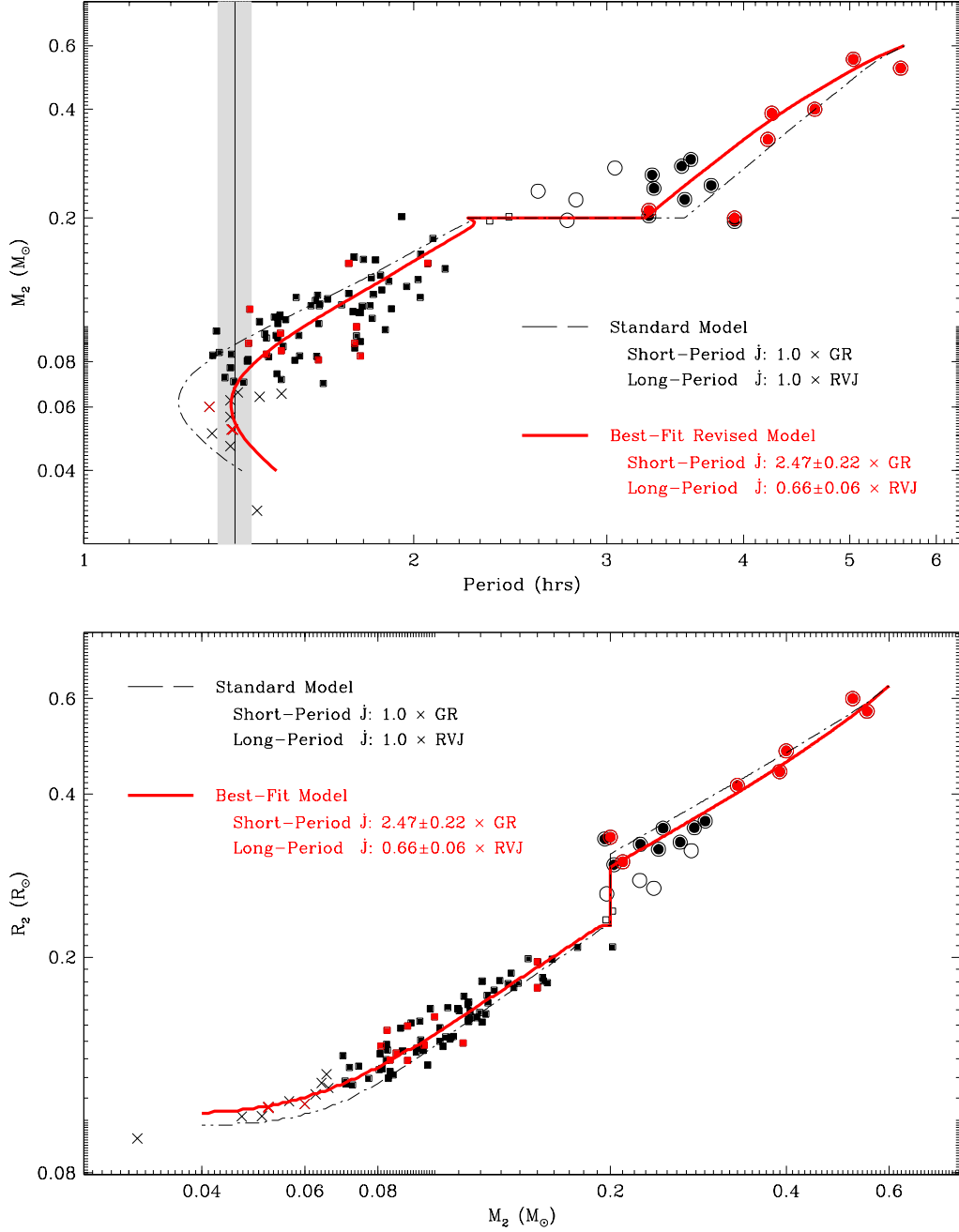


FIGURE 1.6: Model fits to the observed properties of CV donors in the period-mass (top panel) and mass-radius (bottom panel) planes. Data points indicate measurements of CV donors. The black dash-dotted line shows the predicted evolution of donor properties according to the standard model for CV evolution. The red solid line shows the evolution of donor properties along the best-fit model track, see Knigge et al. [28].

1.6 Time keeping

In order to compare different measurements of time variable sources, it is important to use an accurate timing system. Many different timing systems are used on earth, some are used because they are more accurate, other are used because of historical reasons or convenience. A short overview of commonly used time-standards, and how they relate:

- International Atomic Time, TAI: Based on the average of atomic clock around the world, all corrected to run at sea-level at 0K. This time system uses a fixed length for a second, which is 9192631770 cycles of a Cs^{133} atom. It was introduced in 1972.
- Coordinated Universal Time, UTC: Based on the TAI, but leap seconds are added to keep in line with the second based on a solar day (which gets longer due to tidal interaction with the moon). These corrections are not predictable, and can be added or subtracted at half-year intervals. The difference between UTC and TAI time is as time of writing, september 2013, exactly 35 seconds (25 leap seconds and 10 seconds offset from the start). This time is used around the world as *the* time (plus/minus timezone and daylight savings).
- Terrestrial time, TT: as simple offset from the TAI of 32.184s, to keep in line with the Ephemeris time, a time system used by astronomers until 1970.
- Barycentric Coordinate Time: TCB. Time of a clock which is in a co-moving frame with the barycenter of the solar system, but is not affected by time-dilation caused by the gravitational potential. The second in this time standard is slightly longer than the TAI second ($\sim 10^{-8}$), since the atomic clocks on earth are not corrected for the time-dilation caused by the Earths gravitational well. The TCB time will thus slowly get ahead of the TAI time. The goal is to get a time independent of where you measure it, and in order to calculate this time, the theory of general relativity is needed.
- Barycentric Dynamical Time, TDB: Similar to TCB, but ticking a slower rate to match the TT. The difference between TDB and TT is $\sim 30\mu\text{s}$ and are mainly periodic with one year.

Measurements in astronomy can be years apart. For this purpose it is also useful to have a calendar which counts the number of days, the Julian date. In addition, corrections have to be applied for the position and motion of the earth. Here is an overview of often used times in astronomy.

- Julian date, JD: A continuous date, counting the number of days since 1 January 4713 BC ⁴. The start of the day is defined as 12:00, the middle of

⁴Suggested by Joseph Scaliger in 1583. Chosen so all observations are in the positive range

the day. The length of one day depends on the time standard. For example, JD_{UTC} and JD_{TAI} differ in length of a day if a leap second is added and JD_{UTC} and JD_{TT} are offset by $N_{\text{ls}} + 32.184\text{s}$, with N_{ls} the number of leap seconds.

- Modified Julian date,MJD: $\text{JD} - 2400000.5$, used for easier notation and moving the switch between days to midnight.
- Heliocentric Julian date, HJD: The Julian day corrected for the light-travel time from the sun. This correction involves the arrival direction of the light, and the position of the earth. The result is a sine curve with a period of one year and a maximum of about 500 seconds. When papers give a time in HJD, this is usually the HJD_{utc} time, but can also be defined as HJD_{TT} or HJD_{TAI} .
- Barycentric Julian date, BJD: Time corrected for the light-travel time from the barycenter. Similar to the correction of the heliocenter, but also correcting for motion of the planets, which can result in a difference between BJD and HJD of ~ 4 second.

The currently advised time standard by the IAU is the TT, however many papers overlook the issue of correct time keeping and specifying which time standard is used. For further background and discussion see Eastman et al. [16], Hale [20].

Chapter 2

Methods

This chapter discusses the methods used to determine the system parameters of a binary system. The first section discusses the information which can be obtained from spectra, the temperature, surface gravity and radial velocity. The second section discusses the lightcurve of eclipsing binary star and the physics involved. The last section discusses the program used to model the lightcurve, Lcurve, which includes all the different effects on the lightcurve.

2.1 Spectra

Spectra of binary stars are the best way of classifying a binary. The shape of a stars spectrum is pretty straight forward, and thus combinations of two stars can be distinguished. Problems arise when one of the two star outshines the other, or when the stars are very similar, making it look like a single, brighter star. This makes only a few combinations of star easy to identify, for example red dwarfs and white dwarfs. They have a similar brightness, with the white dwarf dominating the blue part of the spectrum en the red dwarf the red part.

By fitting the spectra with model spectra, or spectra of spectral standards, the spectral type of the star can be determined. Determining a spectral type is done by looking at of the overall shape of the spectrum, but also by looking a features like emission or absorption lines which are characteristic for a certain type. This can be a difficult problem since a binary spectrum is a combination of two spectral types, and multiple combinations of spectra can give a good fit to the overall shape. This can be solved by looking a features specific to one spectral type, for example the TiO lines for M-dwarfs.

Sharp features like absorption and emission lines are also useful to determine the shift in the spectra. Due to the relativistic Doppler effect, the wavelength (λ) will change slightly due to orbital velocity ($\Delta\lambda$). Measuring this difference over time gives the orbital period of the binary, but also the velocity of the stars. The relation of redshift and velocity is give by equation 2.1.

$$\frac{\Delta\lambda}{\lambda} = \frac{v_{\text{radial}}}{c} \quad (2.1)$$

If the radial velocity of only one star can be measured (due to causes mentioned above), the mass of both stars cannot be determined. In these cases the mass function is used, which constrains the mass of the star which does not have a radial velocity measurement, see equation 2.2.

$$f(m) \equiv \frac{m_1 \sin(i)^3}{(1+q)^2} = \frac{PK_2^3}{2\pi G} \quad (2.2)$$

With $m_{1,2}$ the mass of the stars, $K_{1,2}$ the radial velocity, q the mass ratio, i the inclination (angle between line of sight and the orbital plane) and P the orbital period.

The situation improves if two radial velocities are available. This gives the mass ratio and constraints the mass for both components, see equation 2.3. By using Keplers law 1.4, the orbital separation can also be calculated. A problem is that the inclination is also required. Determining the inclination of a binary is difficult, and is usually an unknown parameter.

$$m_{1,2} \sin(i)^3 = \frac{1}{2\pi G} (K_1 + K_2)^2 K_{2,1} P \quad (2.3)$$

If the orientation of the orbital plane is nearly 90 degrees, one star may eclipse the other. This is a way to solve the inclination problem, and can also drastically improve the accuracy of the orbital period. In addition, the shape and width of the light curve can be used derive relative radii of both stars. For these reasons eclipsing binaries are extremely valuable, because they offer a way to determine the mass and radius independently from each other. Determining the system parameters from the eclipses is not straightforward, and requires numerical modeling of system. The basic principles and complications are discussed in the next section.

2.2 Lightcurves

First of all, the lightcurve is an excellent tool to determine the orbital period of a binary system. Especially lightcurves with sharp features like eclipses can give very accurate results. A methods often used to determine periodicity is the phase dispersion minimization technique (PDM, Stellingwerf [60], program from T. Kupfer). This method folds the data on a trial orbital period, bins the data and compares the sum of the dispersion per bin to the total dispersion. If the orbital period is correct, the dispersion per bin is low, while an incorrect trial period gives a similar dispersion to the total dispersion. The advantage of this method is that the shape of the lightcurve does not have to be known and can have any shape. To determine the error on the period, the method is applied to the data after moving

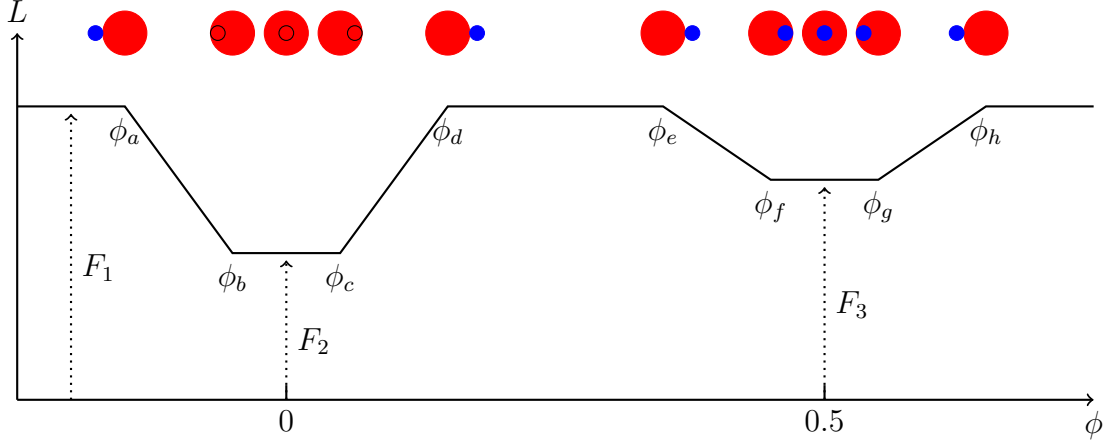


FIGURE 2.1: Schematic representation of a lightcurve and the relative position of the stars, not to scale.

the data points according to their error bars, so-called bootstrapping the data, a method first suggested by Efron [17].

To obtain the other parameters of both stars, a detailed model of the binary is needed. In figure 2.1 a schematic representation of a lightcurve is given. In the following discussion the primary star is the smaller star and the secondary the larger one. The simple lightcurve has three flux levels, F_1, F_2 and F_3 , out of eclipse light, the level of the primary eclipse and the level in the secondary eclipse (see figure 2.1). Equations 2.4, 2.5 and 2.6 show how the flux¹ is related to the radius (R) and temperature (T) of both stars, and the distance to Earth (D).

$$F_1 \cdot 4\pi D^2 = 4\pi R_1^2 \sigma T_1^4 + 4\pi R_2^2 \sigma T_2^4 \quad (2.4)$$

$$F_2 \cdot 4\pi D^2 = 4\pi R_2^2 \sigma T_2^4 \quad (2.5)$$

$$F_3 \cdot 4\pi D^2 = 4\pi R_1^2 \sigma T_1^4 + (4\pi R_2^2 - 4\pi R_1^2) \sigma T_2^4 \quad (2.6)$$

These equations can be rewritten to determine the relative radii and temperatures of both stars:

$$\frac{T_1}{T_2} = \left(\frac{F_1 - F_2}{F_1 - F_3} \right)^{1/4} \quad (2.7)$$

$$\frac{R_1}{R_2} = \left(\frac{F_1 - F_3}{F_2} \right)^{1/2} \quad (2.8)$$

Of course it is not always the case that both eclipses are visible. If the second eclipse is not measurable, $F_1 - F_3 \approx 0$, this means that the radius ratio is very small, and the temperature ratio very high. An example of such a system are white dwarf and red dwarf systems. If only the primary eclipse is measured, this leaves

¹These formulas are for the bolometric flux. Practically lightcurves are measured in some filter band and the flux is only measured at a wavelength band.

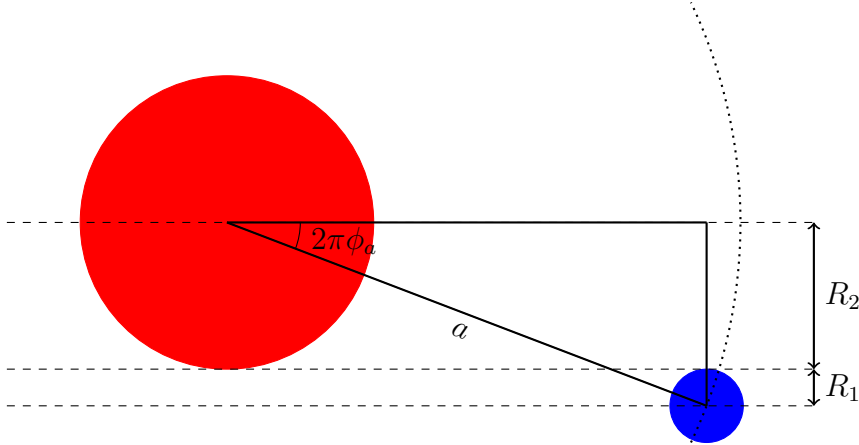


FIGURE 2.2: This shows the top view of a binary ($i = 90^\circ$) just before the ingress.

one degree of freedom more to fit the lightcurve, and the radius and temperature ratios are degenerate.

Besides using the different flux levels to determine the parameters of the binary, the shape of the eclipses can also be used to obtain information. The width (in phase: $\Delta T/P$) of the ingress ($\phi_a - \phi_b$), full eclipse ($\phi_b - \phi_c$), and egress ($\phi_c - \phi_d$) also depends on the radius of both components and orbital separation. Assuming for the moment an inclination of 90 degrees, the phase difference and radii are related by the following equations, see figure 2.2:

$$a \sin 2\pi\phi_a = R_2 + R_1 \quad (2.9)$$

$$a \sin 2\pi\phi_b = R_2 - R_1 \quad (2.10)$$

Which can easily be rewritten as:

$$R_1/a = \frac{1}{2}(\sin 2\pi\phi_a - \sin 2\pi\phi_b) \quad (2.11)$$

$$R_2/a = \frac{1}{2}(\sin 2\pi\phi_a + \sin 2\pi\phi_b) \quad (2.12)$$

An addition complication is the inclination, figure 2.3, which also affects the length of the ingress, full eclipse and egress. The formulas with the inclination included are a simple matter of geometry (see Wood [69]) and depend on the inclination in a complex way.

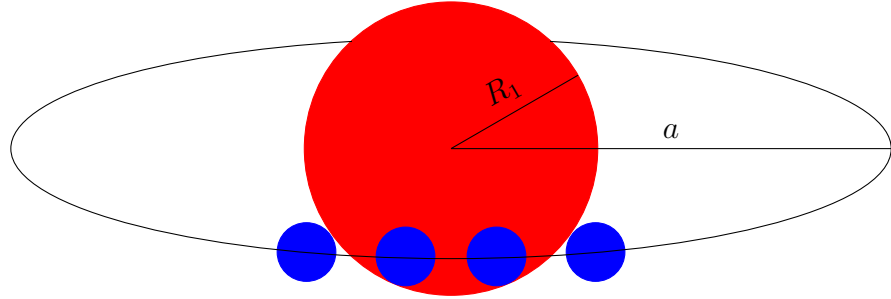


FIGURE 2.3: This figure shows an eclipse with an inclination less than 90 degrees. The result is that the ingress and egress are longer, and the full-eclipse time shorter.

$$\frac{R_1}{a} = \frac{1}{2} \left(\sqrt{\cos^2 i + \sin^2 i \sin^2 2\pi\phi_a} \right) - \frac{1}{2} \left(\sqrt{\cos^2 i + \sin^2 i \sin^2 2\pi\phi_b} \right) \quad (2.13)$$

$$\frac{R_2}{a} = \frac{1}{2} \left(\sqrt{\cos^2 i + \sin^2 i \sin^2 2\pi\phi_a} \right) + \frac{1}{2} \left(\sqrt{\cos^2 i + \sin^2 i \sin^2 2\pi\phi_b} \right) \quad (2.14)$$

This already shows a number of limitations of lightcurve analysis. First is the fact that only the radius relative to the orbital separation can be determined. Second is the degeneracy between inclination and radius, with R_1 increasing and R_2 decreasing for lower inclinations.

Lightcurves show many additional features which require a numerical approach. An effect not specific to binary stars, but important for the limb darkening and gravity darkening. Limb darkening is the effect that when looking at the surface of a star, the star looks slightly fainter on the limb than in the center. This is the result of the viewing angle and optical depth. When looking at an angle, the light has to travel more through the atmosphere compared to radially outward. The result is that the light seen, is emitted farther out in the star which has a lower temperature, and is thus less luminous. Limb darkening is difficult to measure, and is usually calculated and used as input in models. For more information and model parameters see Claret and Bloemen [13].

Gravity darkening is caused by non-uniform gravity. The flux through a surface depends on the local temperature gradient, which in turn depends on gravity. This means that a lower gravity regions are less bright. Gravity can be distorted due to rapid rotation, causing darkening around the equator, or by the distortion of the gravity potential in a binary system. The result is that the poles of the star have a higher flux, while the points closed to the first and second Lagrange points have a lower flux. For 3D modeling of this effect see Lara and Rieutord [31] and for model parameters see Claret and Bloemen [13].

First of all, due to the Roche potential (section 1.5.1), the stars are not spheres, but can be slightly elongated. This effect is important if a star is (almost) filling its Roche Lobe. The results in the lightcurve is a sinusoidal component with a

period half of the orbital period. The reasons for this is the elongated side is seen twice in a rotation. The magnitude of this effect is usually small, but can be used to constrain the mass ratio q (see Zucker et al. [70]). An example of a binary which features these ellipsoidal variations is KPD 1946+4340, see Bloemen et al. [7].

A second effect is the so-called reflection effect. This name is a bit misleading, as the light from one star is not only reflected, but also reprocessed. The reflection effect is most prominent for stars with a very different temperature, for example red dwarfs - white dwarf binaries. A way to view this effect is by defining a new effective temperature of an irradiated surface element, which depends on the unirradiated temperature and irradiation:

$$T_{\text{eff,new}} = T_{\text{eff,2}} \left(1 + \alpha \left(\frac{T_{\text{eff,1}}}{T_{\text{eff,2}}} \right)^4 \left(\frac{R_1}{a} \right)^2 \right)^{1/4} \quad (2.15)$$

with $T_{\text{eff,2}}$ the unirradiated temperature and α the local albedo.

The reflection effect depends thus on the relative size of the irradiator and the ratio between temperatures. A great example is NN Ser, Parsons et al. [46], which consists of a very hot white dwarf ($T = 57000\text{K}$) and a cool red dwarf ($T = 3200\text{K}$), see figure 2.4. If the irradiation effect is very strong, the description given above might not be sufficient. The backside of the irradiated star is completely unaffected in this description, but heat transport could heat it up, increasing the luminosity of unirradiated parts as well. See for example Budaj [9] for an improved description of irradiation.

For very compact systems like white dwarfs, relativistic effects start to play a role. The high density of the compact source curves the space around it, deflecting light. In the lightcurve of an eclipsing binary, the star acts as a lens in front of the second star, temporarily increasing the amount of light reaching the observer. The effect is quite small, but it makes the secondary eclipse shallower. This effect can be used to distinguish between planets and white dwarfs, see for example Muirhead et al. [39].

A second relativistic effect is due to the high velocity of both components, resulting in an effect known as Doppler beaming (also known as Doppler boosting). The emitted light of the star is focused toward the direction of motion. This increases the total amount of light received when the star is moving towards the earth, and decrease when it is moving away. In figure 2.5, all 4 of these effects are required to model the lightcurve.

2.3 Lightcurve fitting: Lcurve

To program used to model the lightcurve is Lcurve, developed by T.R. Marsh, and described in Copperwheat et al. [14]. The aim of the code is to model the

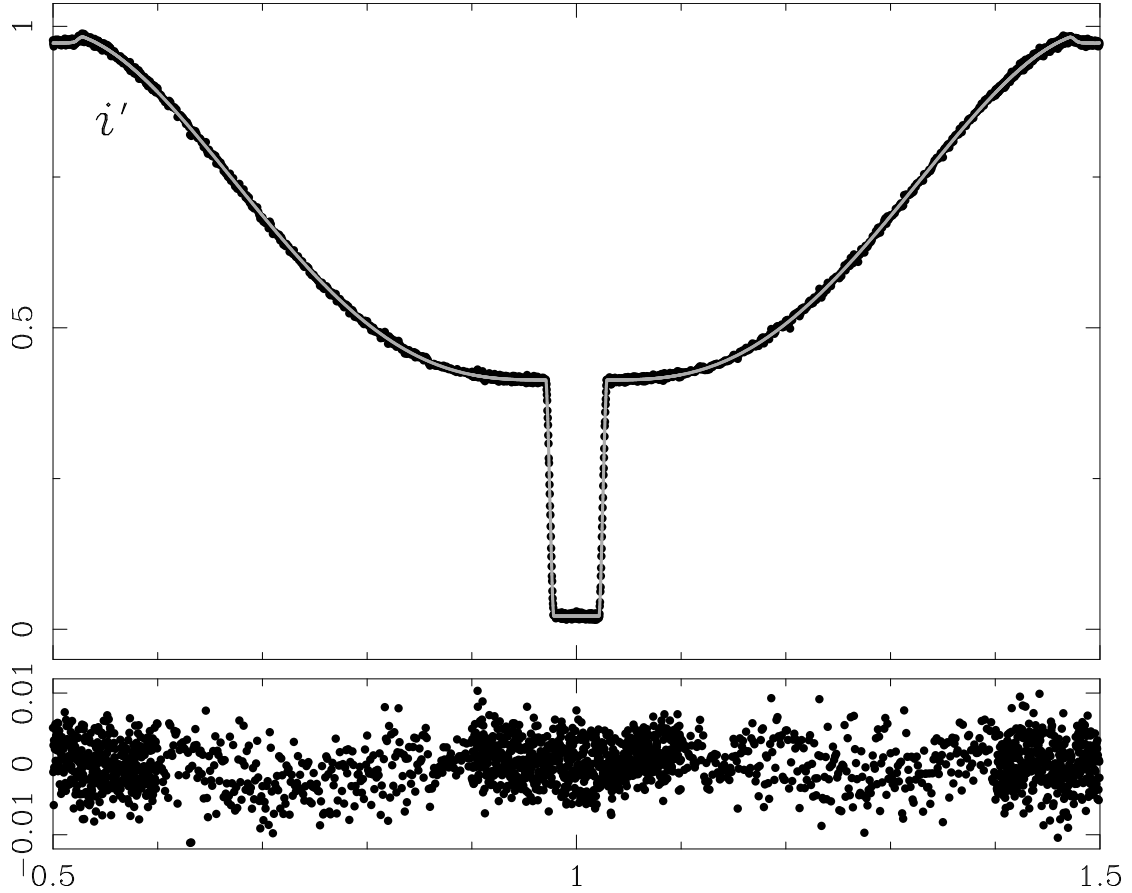


FIGURE 2.4: Lightcurve of NN Ser in the i' band. Note the strong reflection effect, about ~ 10 times the light of the in-eclipse lightcurve. From Parsons et al. [46]

lightcurves of eclipsing accreting and detached white dwarf red dwarf binary stars.

The program can use up to four components, the white dwarf, red dwarf, an accretion disk and a bright spot (spot where the accretion flow impacts the accretion disk). Detached systems (like PTF1108ag) only use the stars. A full list of parameters and their description can be found in appendix B. All components of the model are built up using flat elements with a specified area, position, orientation and brightness. The program calculates the total light by summing over all components, taking into account the orientation and blocking of light. The exposure time is taken into account by calculating multiple points covering an exposure and using trapezoidally-weighted averaging.

Two main methods of minimization are used, the simplex method and the Levenburg-Marquardt method. The simplex method is robust, while the Levenburg-Marquardt method can give error estimates of the parameters. For complex fits, these methods were both not sufficient, which is why a Markov Chain Monte Carlo (MCMC) method is also implemented. This method uses random jump and checks by using the χ^2 value to accept or reject the jump. By using a chain of 10000 or more

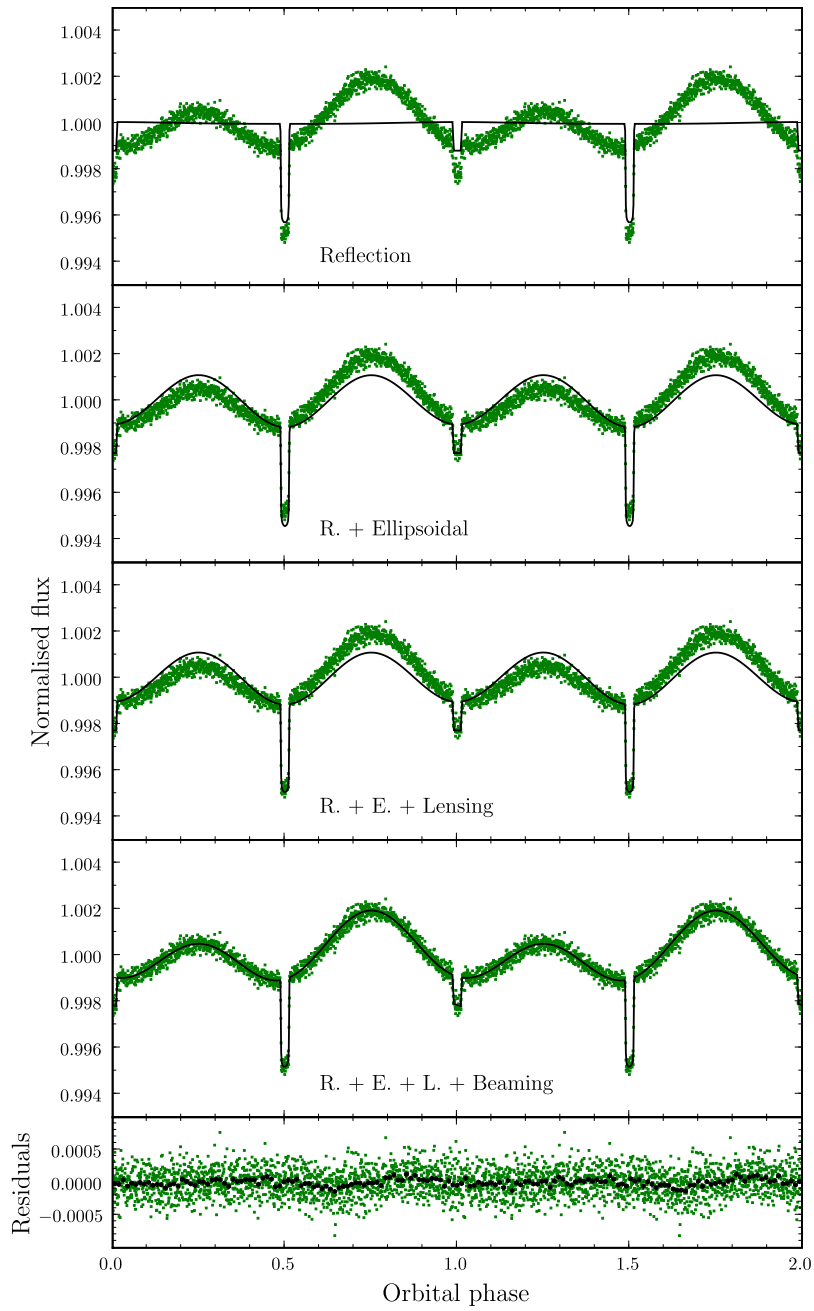


FIGURE 2.5: Lightcurve of KDP 1946+4340. This figure shows the different effects needed to fit the lightcurve correctly of this binary correctly. Taken from Bloemen et al. [7]

models, the parameter space of solutions is sampled, which gives the best model, but also the error on the parameters.

A significant problem with the Lcurve MCMC (LCMCMC) program is the parameter degeneracy. This causes narrow, curved parameter space solution for example in q and i , and for r_1, r_2 and i . If a linear jump distribution is used, the probability of jumping in the 'right' direction is small, and jumps to outside the solution space common. The result is that the chain is stuck in a small part of the solution space. This can be solved by using a correlated jump distribution, which increases the probability to jump along the direction of the correlation. For example, solutions with a large r_1 , require a smaller value for r_2 , see 2.14.

The correlations between parameters in the jump distribution are only linear, while in reality they can be curved. This can make it difficult to correctly sample the outer edges of the parameter space of the solution, since the jump distribution is aimed in the right direction for that part of the solution space.

Chapter 3

Data and reduction

PTF1108ag is a newly discovered eclipsing red dwarf - white dwarf binary. It stood out in the PTF survey because it 'dropped out'; some images did not show a star at the location of PTF1108ag. This was reason for D. Levitan to do followup spectroscopy with the Hale telescope at the end of January of 2012. During the same night, Ultracam followup done using the William Herschel Telescope on La Palma (observers P.J. Groot, C.M. Copperwheat and J.C.J. van Roestel). A complication with the data is a star located about $1.5''$ from the eclipsing binary, which is called 'interloper' in the rest of this thesis. This chapter discusses the different data sets and the reduction of the data.

3.1 Palomar transient factory data

PTF1108ag was identified as a variable target by the PTF survey. This section discusses the PTF survey and the data used in this research.

3.1.1 Palomar transient factory

The Palomar Transient Factory (PTF) is a survey aimed at exploring the transient sky of the northern hemisphere. The survey uses two telescopes: the automated 48 inch Palomar Samuel Oschin telescope (P48), and the automated Palomar 60-inch telescope (P60) which is used for followup of transients found in the survey. The camera used in the survey is a 101 mega pixels mosaic camera, with a 8.1 square degree field of view with a 1 arc second sampling. The observations are done in broad band filters (Mould-R and SDSS-g'). The magnitude limit in good conditions is $m_{g'} \approx 21.3$ and $m_R \approx 20.6$ for the standard 60 seconds exposure time. The data reduction is, like the observations, done fully automatically, as well as a preliminary identification of the source.

The observing strategy is a composite of four different programs (5-day cadence, dynamic cadence, Orion field and H α), all using P48. The two most important, the

5-day cadence and dynamic cadence programs use the combination of Mould-R and SDSS-g' filters. The reasons to use two different filters is to optimize the survey for the varying Moon conditions. During a full-moon, the R-band is used because the sky background depends less on moon phase. During dark-sky conditions, the worse quantum efficiency of the chip in the g' filter is compensated by the darker sky and bluer color of most transients. The cadence is the main difference between the two programs. The 5 day cadence project is taking 2 exposures, one minute apart, every 5 days of fields more than 30 degrees from the galactic plane ($|b| > 30^\circ$). The dynamical cadence program is aimed at finding transient object varying on \sim 1day timescales, like CV's, RR Lyrae and flaring stars. The cadence is not fixed, and changes depending on the results obtained. The Orion field program observes one field with a high cadence to be able to find potential exoplanets transiting their parent star. The H α program is using four narrow band filters to find and identify object out to 200Mpc. Further information about PTF can be found in Law et al. [32], Rau et al. [52] and references therein.

3.1.2 PTF1108 photometry

The data obtained from the PTF pipeline requires little further calibration. However, the time format used by PTF is MJD or HJD. In order for the data to be comparable to the Ultracam data, the HJD calibration is insufficient, and thus BTD_{tt} have been calculated from MJD times. The data are also converted from magnitudes to Jansky, and outliers have been removed. The data from both bands are shown in figure 3.1. The reasons for the clustering of points is that PTF1108ag has a declination of 33 degrees, and is thus only observable a few months a year.

3.2 Ultracam photometry

Followup photometry was done using Ultracam camera at the William Herschel telescope. This section discusses the data acquisition and reduction with Ultracam.

3.2.1 Ultracam

Ultracam is a high-speed, three-color CCD camera designed for (very) high frequency imaging photometry (up to 500Hz). It was mounted on the William Herschel Telescope (WHT), a 4.2 meter Cassegrain telescope on La Palma (Spain). The camera uses three 1024x1024 CCDs, which gives a 5 arcminutes field of view on the Cassegrain-focus of the WHT (0.3 arcsec/pixel). It uses two dichroic beam-splitters to split the beam in 3 colors. The colors used can be different combinations of filters, for example u', g' and r'. The instrumental throughput is about 50% in the green and red arms of Ultracam and 30% in the blue arm. This gives about 2000 counts for a $m_V = 18$ star on the Cassegrain focus of the WHT.

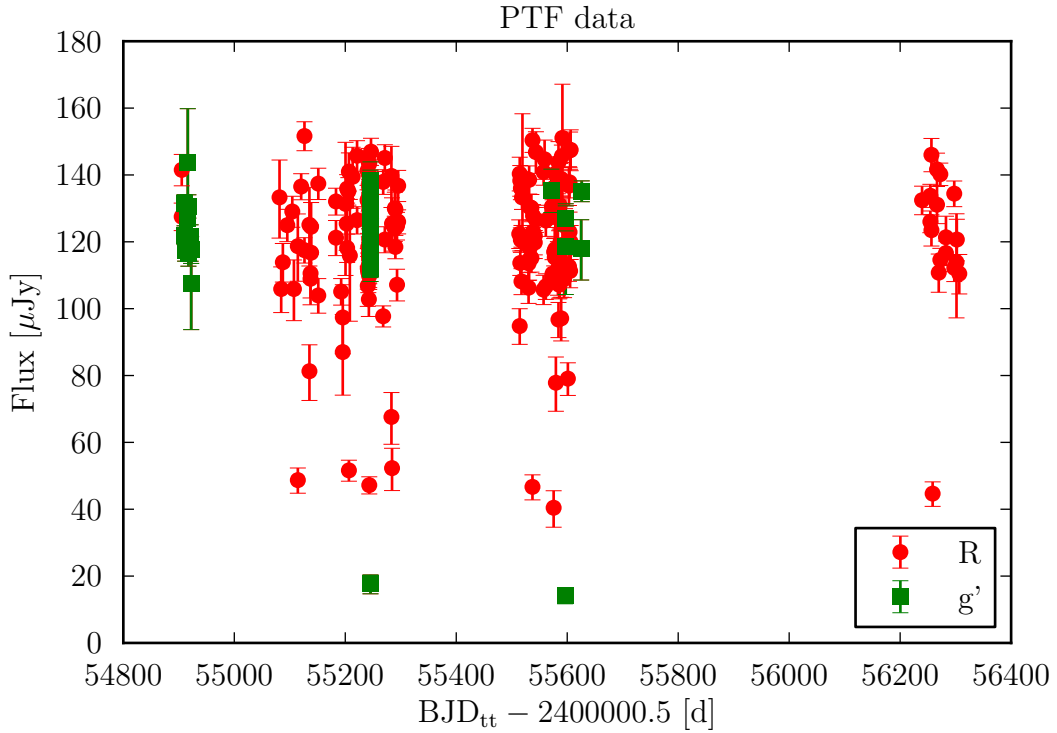


FIGURE 3.1: Data from PTF in Mould-R (R) and SDSS-g' (g'). The data is converted from magnitude to flux and the time is converted from MJD to BJD

Ultracam is specifically designed for very high exposure frequencies. The problem with standard CCD chips is that it can take a long time to readout the data, in the order of several seconds. Ultracam circumvents this problem by using a frame transfer CCD. A frame transfer CCD is divided in two halves, one half is used as a standard CCD chip, while the other half is used as storage. Instead of reading out the image directly, it is moved to the storage frame, which takes only 24 milliseconds. After this operation a new image can be taken, while the storage area is read out. This reduces the dead-time to only 24 milliseconds instead of 2 seconds it takes to readout the CCD.

The frequency can even be increased by using different readout modes. The standard readout mode is the full-frame readout, which uses the whole frame. Reading the whole frame takes about 2 seconds, so if higher frequencies are required, parts of the chip can be used, windowed mode. This significantly reduces the readout time, but is still not the fastest mode. The fastest readout is obtained with the driftmode. In this mode only one window, which is positioned on the border between the imaging and storage area, is read out. The storage area stores *multiple* exposures while reading out and digitizing these, see figure 3.2 c. This greatly reduce the deadtime, allowing for a frame rate of 500 Hz. This readout mode is not capped by the readout time anymore, but by the speed at which the charge can be moved. A downside of this mode is that pixels spend a longer time on the chip, which causes more dark current to accumulate. An overview of the different

modes is shown in figure 3.2. See Dhillon et al. [15] for more information about Ultracam.

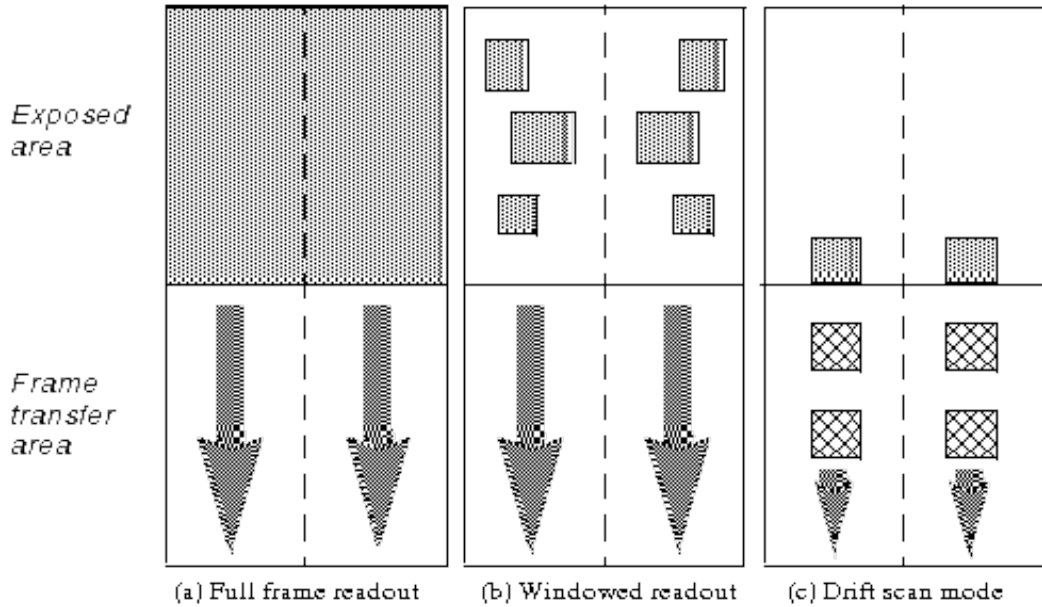


FIGURE 3.2: Different readout modes for Ultracam. (a) show the full frame readout, (b) shows the windowed mode and (c) the Drift scan mode. Taken from Beard et al. [5].

3.2.2 The data

The data were obtained on 30-01-2012 and 31-01-2012, the log files can be found in appendix A. The first night in u',g' and r'' filters and the second night in u',g' and i' filters'. Both nights the fullframe readout mode was used but with a binning factor¹ of 2x2 to reduce readout time. The total exposure time was 19616 seconds and 18759 with exposures of 3.0527 and 2.0527 seconds.

A 'bias' frame with a 2x2 binning was taken at the end of the first night, and 'flat'-frames were taken during dusk and dawn. Feige 66, a well known calibration star, was observed at the end of both nights. The weather was good, with a variable seeing between 1" and 2" for the first night and a seeing of 1" increasing to 2" the second night.

3.2.3 Image corrections

The data reduction and extraction was carried out using the Ultracam reduction software, see Marsh [35]. Before any data extraction can be done, the images

¹Grouping pixels to function as one large pixel

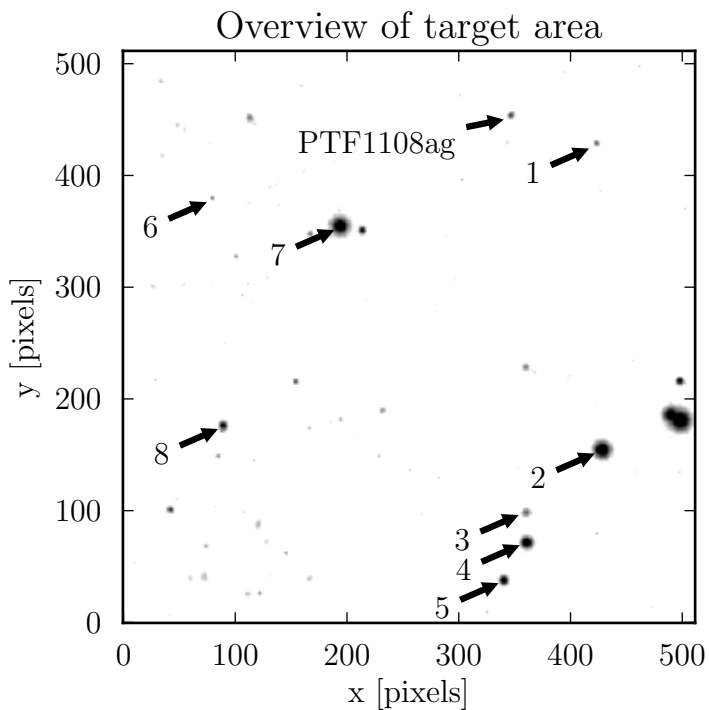


FIGURE 3.3: The target, PTF1108ag, and the comparison stars indicated by a number.

need to be corrected for systematic error by the telescope and camera. The image processing is done using the Ultracam pipeline. The first correction is subtracting the 'bias' frame from all other exposures. A bias frame is a zero second exposure, which measures the initial value of pixels. This zero-second pixel value is offset by a fixed amount to ensure the values are always positive, as not to cause problems with the analog-digital converter. But more important are difference between the zero-second counts between pixels. Some pixels can have excessive amount of zero-second counts, so-called hot pixels. By taking a bias-frame and subtracting this from all other exposures, these offset are removed.

The second operation is to remove any sensitivity differences over the chip. This difference is caused by a combination of the optics and the detector. The sensitivity difference can be measured by taking an exposure of a homogeneous field, usually the sky at dusk and/or dawn, (a 'sky flat'). It is possible that a star is already visible during dusk or dawn, which would make the flatfield useless. To counter this, a number of exposures are made while slightly changing the position on the sky. This moves the stars over the image, and are then filtered out by taking the median of all individual flatfields. This final flatfield is then normalized to an average of 1 and all images are divided by this final flatfield frame.

3.2.4 Aperture photometry

Aperture photometry is used to determine the total flux of a target, see figure 3.4. It works by defining circle around the target. All pixels in the inner ring are summed up. The area between the second and third circle is used to determine the background flux, and is used to remove the background flux from the inner ring. Ultracam can use different methods of adjusting the apertures between frames. First the position is checked between every frame and adjusted. To get an optimal signal to noise, it is possible to define the apertures in FWHM of the profile. This works by first fitting a Gaussian or Moffat profile and then doing the extraction based on the FWHM of the profile. This method results in the highest signal to noise per frame and was used for the extraction initially.

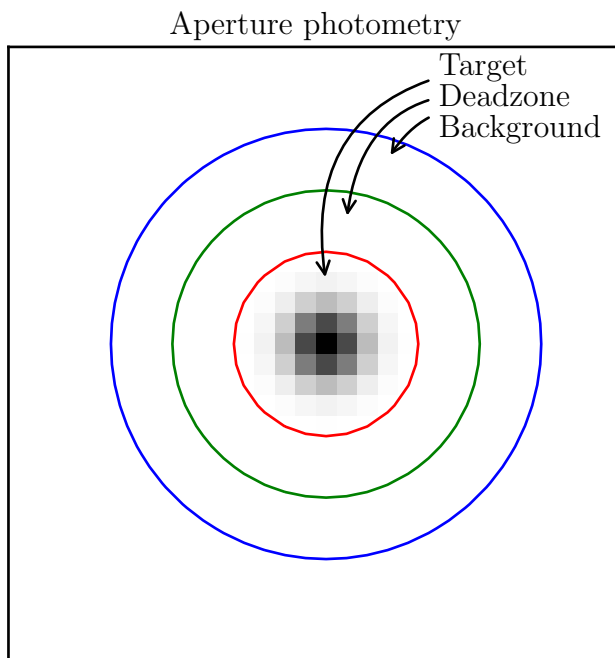


FIGURE 3.4: Aperture photometry uses three radii to extract the signal. The central ring defines the area used to sum over to get the signal. The area between the red and green ring is ignored. The outer ring is used to determine the background.

However the extraction revealed strange results; the number of counts increased when then seeing got worse. This is caused by an red star about 2 pixels away from the target, see figure 3.5, and is called 'interloper'. The contamination by the interloper increases as the seeing gets worse. To resolve this issue, a fixed position and large, 10 pixel radius, fixed aperture is used. By using a large aperture both stars, PTF1108ag and the interloper are in the aperture and the resulting lightcurve is thus a combination of the binary PTF1108ag and the interloper.

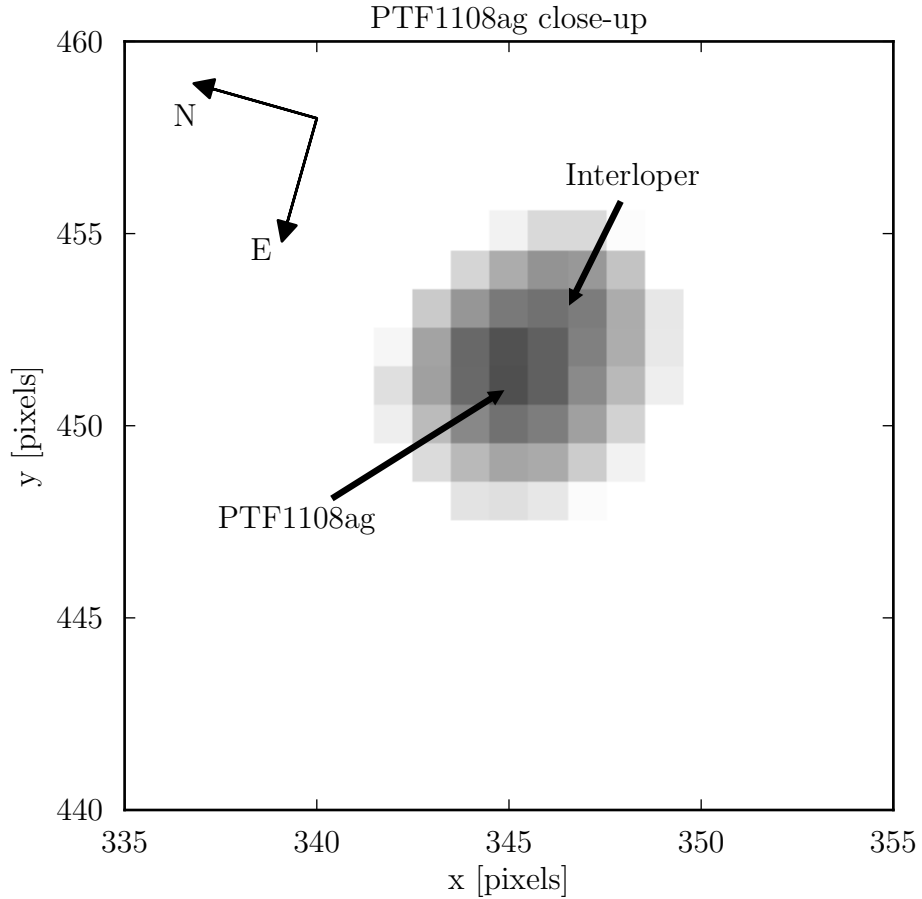


FIGURE 3.5: A closeup of an Ultracam image in the r' band. This shows that PTF1108ag has an interloper about 2 pixels away. The performed aperture photometry contains both stars and thus the contribution of the interloper has to be subtracted before fitting the lightcurves.

3.3 Interloper contamination

To determine the fraction light of the total measured light by the interloper, averaged Ultracam images per filter from before, after (200seconds) and during the individual eclipses are used. The profile of the 2 stars is fitted with a double 2D Gaussian. The parameters of this profile are the background, height and position of both components, and a standard deviation for both the Gaussian. To find the best fitting values the χ^2 value of the fit was minimized. The minimizer used is the TNC method (a truncated Newton algorithm) from the python scipy package. This method allows for boundaries to be set to keep the fit from drifting away.

To be sure the real minimum is found the minimization is started for a grid with varying position for both components. This is done to be sure that the minimizer did not get stuck in a local minimum. To check if the combination of 2 Gaussian so close together causes any biases to the fit, artificial data with noise is created

with the best fit parameters and fitted again. The in- and output values do not differ significantly. The standard deviations for the final fit are determined using the bootstrap method.

The fit to the u' outside of the eclipse does not fit the interloper, as the difference in counts is too high. The in eclipse data for the u' filter also fails, as the signal is just to low for both PTF1108ag and the interloper. The g' is also difficult to fit, as the white dwarf is a lot brighter than the interloper. The in-eclipse data has a relative low signal to noise and to improve the fit, the distance between the two components was fixed by using information from the r' and i' . The signal to noise in these bands is higher (since the interloper is red), and a better contrast because both components have similar intensities. The average values are $dx = 1.69 \pm 0.04$ pixels and $dy = 1.92 \pm 0.04$ pixels, which are the weighted average values determined from the out eclipse data. This corresponds to a total distance of 1.54 ± 0.06 arcsec if the Ultracam pixel scale of 0.600 pixels per arcsec is used. By determining the rotation of the field from 2 stars, 119.1 degrees, the offset is $-1.49''$ RA, $-0.32''$ DEC.

As a confirmation of the distance, SDSS images in 'i' and 'r' bands are used. The fits files from the SDSS survey were fitted with the same method as described above. To translate the distance between the two components from the SDSS data to the Ultracam data, a rotation and scaling is required. The translation between the two images is determined by measuring the position of star 4 and 5 in both fields. With this information the translation can be calculated from the SDSS image to the Ultracam image. The result is the corresponding x distance, $dx = 1.68 \pm 0.02$ pixels, and the corresponding y distance is $dy = 1.83 \pm 0.02$ pixels. For the r' filter the result is $dx = 1.75 \pm 0.03$ pixels and $dy = 1.70 \pm 0.02$. These distances are very similar to the once found with the Ultracam data, but not within errorbars. Possible differences are the differences in zenith angle at which the observation were taken, which could change the position of the components, depending on color.

The reduced χ^2 value of the fits is more than 1 in most cases. A possible cause is either the errors are underestimated or that the profile is not exactly Gaussian. An improvement could be to use a Moffat profile, but this requires an extra free parameter, which would complicate the fitting even further. The final result is shown in table 3.1.

TABLE 3.1: The percentage of light from the interloper of the total light measured, weighted average of all 8 eclipses. No data for the u' band is available as the interloper is faint.

Filter	in-eclipse cont.	out-eclipse cont.
g'	$73.18 \pm 1.33\%$	$8.58 \pm 0.75\%$
r'	$76.42 \pm 1.36\%$	$25.50 \pm 0.88\%$
i'	$81.78 \pm 1.44\%$	$57.07 \pm 0.81\%$

TABLE 3.2: Calibration using Feige66. Magnitudes taken from Smith et al. [59]

date	filter	counts/s	magnitude	Flux/counts [$\mu\text{Jy}/\text{c}$]
30	u'	576725 ± 487	9.926	0.673955
	g'	3542568 ± 1174	10.271	0.07985
	r'	1617081 ± 799	10.747	0.11284
31	u'	3576388 ± 579	9.926	0.01868
	g'	3283517 ± 536	10.271	0.08615
	i'	905222 ± 287	11.114	0.14376

3.3.1 Calibration

To determine how much energy every CCD count represents, it is necessary to measure a source with a known luminosity. The usual way of doing this if measure a standard star every night, in this case Feige66. Since both observations are done using the same instrument, with (roughly) the same atmospheric conditions, the only difference between the total amount of counts is the intrinsic brightness of both stars. By using the known magnitudes per band of Feige66, the amount of flux represented by one count can be calculated, see equation 3.1. This can then be used to calculate the energy corresponding to the obtained photons of PTF1108ag.

$$\text{Flux/counts}[\mu\text{Jy}] = 3631 \cdot 10^6 \cdot 10^{-0.4m} / (\text{counts/s})[\mu\text{Jy}] \quad (3.1)$$

The ugriz filters are made so that the total flux of a magnitude 0 star is equal to 3631 Jansky. There are however some small systematic offset, in the order of 0.04 mag, see [57]. The magnitude system for stars is a logarithmic scale in which each magnitude is a factor of 2.5 in energy. For further information about the magnitude conversion, see Hale [20, p.238].

Feige66 is bright subdwarf O star with a magnitude of ~ 10 . This star was measured with Ultracam at the end of both nights (30-01-2012 and 31-01-2012) and can thus be used to calibrate the photometry of PTF1108ag. In table 3.2 the measured counts per second and the magnitude of Feige66 is given for the different filters. By using equation 3.1, the amount of flux per electron count can be calculated.

A discrepancy in the data here is the large difference in the u' bands between the two days. The reasons for this is that the u' band is saturated on the 30-01-2012. This underestimates the total amount of counts from Feige66, and thus overestimate the energy per counts, resulting in a incorrect correction. The difference in the g' band calibration is smaller, and this difference is likely due to a difference in atmospheric conditions, which were a bit worse during the second day, resulting in a slightly higher flux/counts.

The second method for calibrating the data is using SDSS magnitudes from star in the same field of view. The advantage of this method is that the calibration data is taken at the same time as the target. In addition, multiple calibration stars can be used, but this depends on the field of view and the availability of magnitudes from

SDSS. Aperture photometry has been done on 9 different targets, PTF1108ag and 8 targets in the field potentially useful for calibration. An overview of all targets can be seen in figure 3.3.

However, not all of the 8 calibrators have been used. The brightest star would give a very good signal to noise, but unfortunately was overexposed at some times. This occurs when the seeing gets better, which causes the PSF to be more peaked, saturating the central pixels. Number 3 and 6 were excluded because these are galaxies, and thus extended sources, which respond different to seeing variations. Targets 7 and 8 are unusable due to a close companion. For target 7, these close companions were masked, but the star is still an outlier in compared to the other remaining stars. Useful remaining stars are 1,4 and 5, of which star 1 is too faint and has a very low signal to noise ratio to be useful. The final calibration is thus done using star 4 and 5, by summing both lightcurves and determining the joint magnitude. The position and magnitude of star 4 and 5 can be found in table 3.3.

TABLE 3.3: Position and magnitudes of the target and reference stars from the SDSS survey. The errors on all magnitudes is 0.01 or less. Note that PTF1108ag is a combination of the binary PTF1108ag and the interloper and is classified as a galaxy in SDSS.

Star	RA	DEC	u'	g'	r'	i'
PTF1108ag	08:57:13.26	+33:18:43.04	18.44	18.50	18.55	17.94
4	08:57:28.82	+33:16:46.08	16.75	15.54	15.16	15.03
5	08:57:30.69	+33:16:47.09	18.04	16.89	16.49	16.35

To illustrate why this method is preferred over the use of the calibration star Feige66, the energy per count value for the calibration stars 4 and 5 and Feige66 are plotted in figure 3.6. This shows the variability of the energy calibration over the night. The scatter is cause by the fluctuations in atmosphere. The steady increase is caused by the change in airmass. At the start of the observation the stars were near zenith ($\sim 85^\circ$) and at the end of the observation the stars had a altitude of $\sim 30^\circ$. It is of course possible to remove these effects by first using the stars in the field of view, and then calibrating using Feige66. This detour is not necessary since SDSS has very accurate (error ~ 0.04 mag, see [57]) magnitudes available.

This methods is applied to all the data obtained, in the three filters. The final result is shown in figure 3.7. This clearly shows a decrease in flux, almost disappearing in the u' filter. The period of the dropout is about 2.5 hours and sinusoidal variation is also present with the same period.

3.4 Spectroscopy

Spectroscopic data of PTF1108ag are obtained with the double beam spectrograph on Hale telescope by D. Levitan during the same period as the Ultracam data.

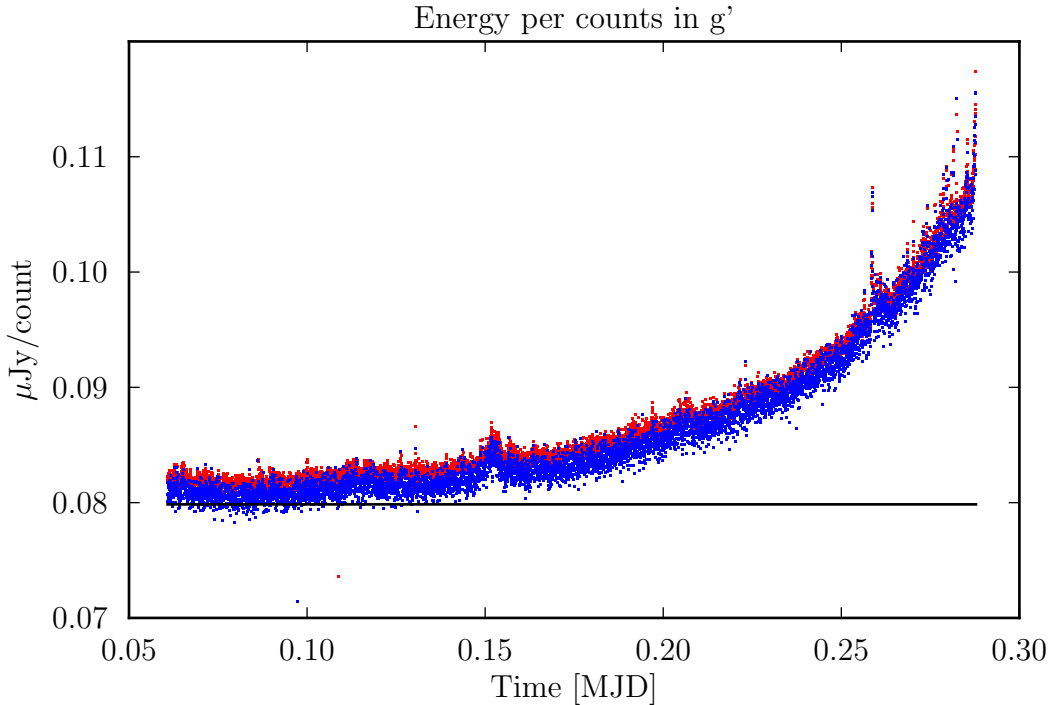


FIGURE 3.6: Comparison of the different calibration stars. The black line indicates Feige66, the red and green dots are star 4 and 5. The counts per second were calibrated using the magnitude from SDSS, using equation 3.1. The increase of energy/counts is caused by the increase of airmass.

The reduction of the data is done using IRAF using the guide by Massey et al. [37].

3.4.1 Double beam spectrograph

The Double Beam Spectrograph (DBSP) is mounted on the 200 inch (5.1m) Hale telescope, built in 1948 located on Palomar Mountain (California, USA). The instrument itself was built in 1982, and was designed to work in the spectral range from 3000Å to 11000Å (DBS [1]). To obtain a good efficiency in both the red and the blue range, the light is split at 5500Å by a dichroic, sending the red and blue beam to two different CCDs. These CCDs have been replaced many times since commissioning, and currently are a 4096x2048, 15 m pixels chip in the red and a 2048x4096 chip in the blue arm. The typical detector throughput is 12%, resulting in count values of 2100 detected photons/Å/second for a (monochromatic) magnitude 10 star. For more information see DBS [1], Oke, J.B. and Gunn, J.E. [42].

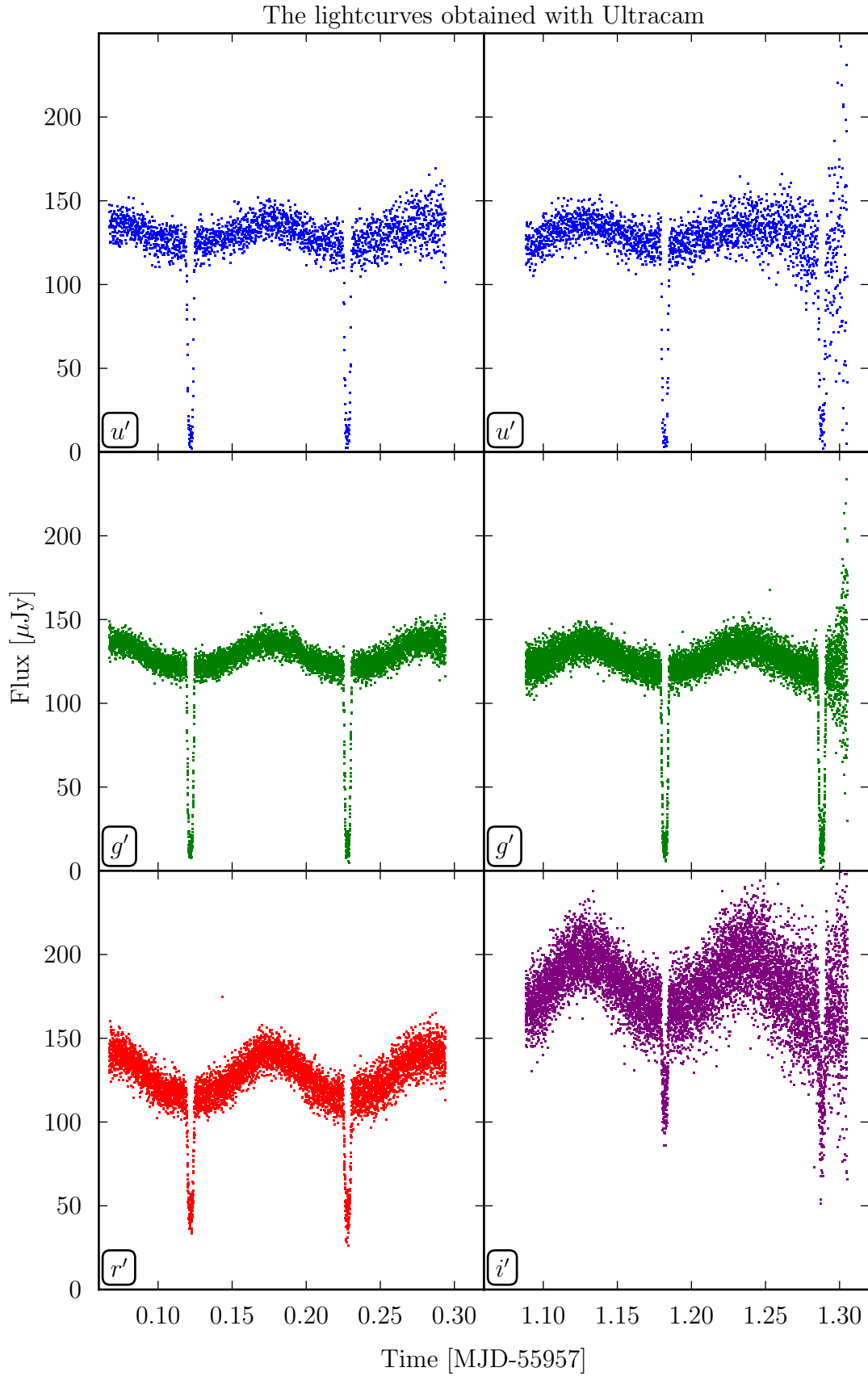


FIGURE 3.7: The lightcurves of PTF1108ag, containing both PTF1108ag and the interloper. The left panels show the data obtained on the night of 30-01-2012, the right panels is data obtained on the night of 31-01-2012. The reduction is described in the text.

3.4.2 The data

The data were taken during the same days as the Ultracam run, from the 29th to the 31st of January. The first night 4 exposures were taken but only in the blue arm². The bulk of the data were taken on the second night, with 33 exposures. There is however a gap halfway in the data due to bad weather, this is also visible in the quality of the data just before the interruption. The last night 4 additional spectra of PTF1108ag were taken and a single exposure the interloper $\sim 2''$ away (designated as PTF1108ag.comp). The exposure time of all spectra of the target in red and blue are 300 seconds.

In addition to the object data, calibration measurements were also taken. To correct for instrument and telescope systematic errors, 10 bias frames and 10 flat frames were taken at the beginning of the first night. In order to do a wavelength calibration, spectra of FeAr and HeNeAr lamps with the blue and red arm (called 'arc' frames) are obtained every night. To calibrate the flux, a calibration star (G191B2B) was measured during the three different nights. For an overview of all data, see appendix A.

3.4.3 Reduction

As with the photometry, the systematic offset of the zero-level of the detector can be corrected by subtracting the median of the bias frames from all other exposures. Correcting for differences in sensitivity is a bit different for spectroscopy when using a 'skyflat'. The skyflat is a combination of the CCD sensitivity and the spectrum of the sky at dawn/dusk. The goal is to obtain a frame which only contains the CCD pixel sensitivity, which means that the sky-spectrum has to be removed. This is usually done by summing over all rows in the spatial direction, and fitting the obtained spectrum using a polynomial of an appropriate order. This fit is then used to divide out the spectrum of the 2D flat-frame, and results in only the pixel sensitivity. The applied method is slightly different, instead of fitting the spectrum, a boxcar smoothing function (order 6) is used to obtain the sky-spectrum. From here the procedure is the same, the 2D skyflat is divided by the obtained sky-spectrum. All other frames can then be divided by the sensitivity to remove the difference per pixel.

A common problem with CCD-imaging are cosmic ray hits. These particles can hit the CCD-chip, resulting in a high pixel count in a few clustered pixels as can be seen in figure 3.8. The chips of the DBS are also affected by these cosmic rays, and these need to be removed so the data won't be contaminated. The program used to remove these cosmic rays, LAcosmic. This program identifies the sharp edges of cosmic rays instead of the difference in profile. This way it can reliably distinguish cosmic rays of arbitrary shapes, but removing cosmic rays in the spectrum is still difficult, see van Dokkum [65].

²The red data are missing for unknown reasons...

The cleaned 2D images now need to be converted to a spectrum. This is done by summing over the pixels in the spatial direction, adding all pixels measuring the same wavelength. The procedure is to determine the center of the profile for every line of pixels in the spatial direction. The location of all maxima is fitted with a third order Legendre polynomial. As can be seen in figure 3.8, it is important to remove the background. The background is determined with pixels 15-30 away from the center. These pixels are then fitted with a first order polynomial and subtracted from the other pixels. The pixels around maximum are summed up, with the limit set by 5% of the maximum value, about ~ 6 pixels in either direction. This results in a 1D spectrum, with the total number of counts versus the dispersion axis in pixels. [36]

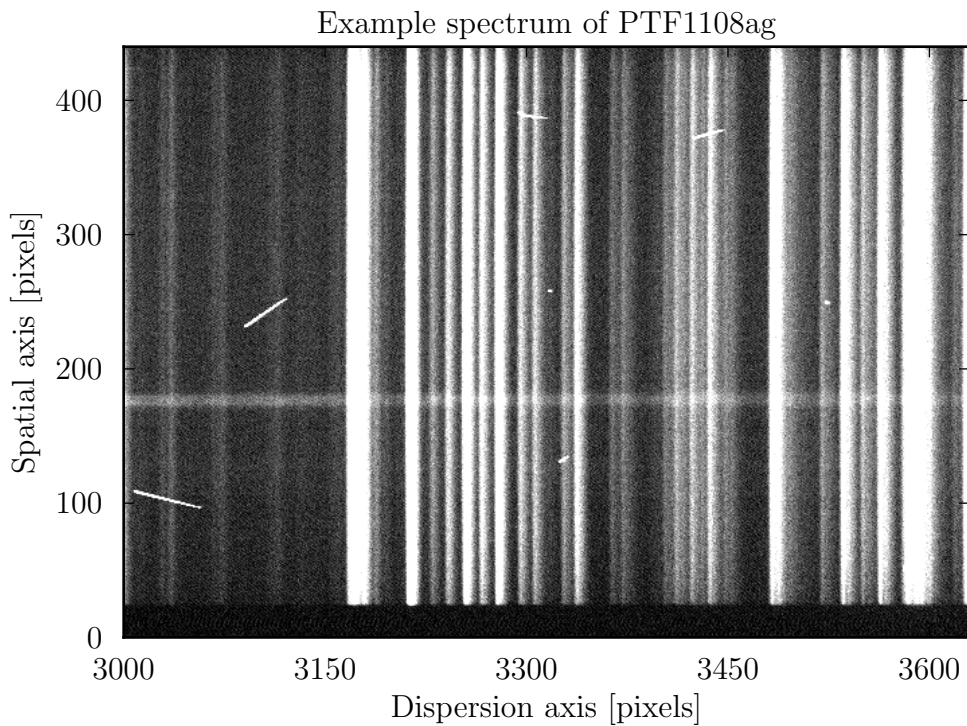


FIGURE 3.8: An example of a raw fits file. The horizontal is the dispersion axis and the vertical the spatial axis. The spectrum of PTF1108ag is the horizontal line crossing the figure. The vertical lines are emission lines by the atmosphere. The short stripes and dots are cosmic rays.

3.4.4 Wavelength calibration

To calibrate the dispersion axis to a wavelength the calibration lamp spectra, which show sharp emission lines with a known wavelength, are used. By assigning a wavelength to each emission line, the correlation between pixel and wavelength can be fitted. For the red arm 25 lines are used, resulting in a RMS scatter of ~ 0.08 pixels, and 52 lines are used for the blue arm resulting in a typical RMS of ~ 0.07 pixels. This fit can then be applied to all other spectra by a linear combination of

the two closest calibration files (in time), which results in a spectrum with counts vs wavelength.

3.4.5 Flux calibration

The number of counts need to be converted in an energy, which is why the calibration stars is needed. These calibration star has a known spectrum (called a 'spectrophotometric standard'), which can be used to determine the counts/energy for every wavelength. The ratio between the measured data and the real spectrum (taken from the 'onedstds' database in IRAF) is fitted with a cubic spline function of order 5, resulting in a RMS of ~ 0.07 and ~ 0.08 in red and blue.

Before this efficiency can be used to convert counts to flux the airmass needs to be taken into account. The airmass is different for every exposure and absorbs a different percentage of the energy per wavelength. The function used to correct this airmass is the standard formula used by IRAF, see 3.2. The extinction factor is ~ 1 for 3000\AA and decreases exponentially to ~ 0.1 at 10000\AA .

$$F_{corrected} = F_{measured} 10^{(0.4 \cdot airmass \cdot extinction\ factor)} \quad (3.2)$$

The final result is the 'sensitivity function', which is used to calculate the energy per bin. This sensitivity function is then used to convert photon counts to an energy in units of F_λ .

The final flux calibrated spectrum of PTF1108ag is shown in figure 3.9. It does show some atmospheric features, for example at $\sim 7600\text{\AA}$. Besides these, weird oscillations are visible in the blue part the spectrum, which are detector artifacts.

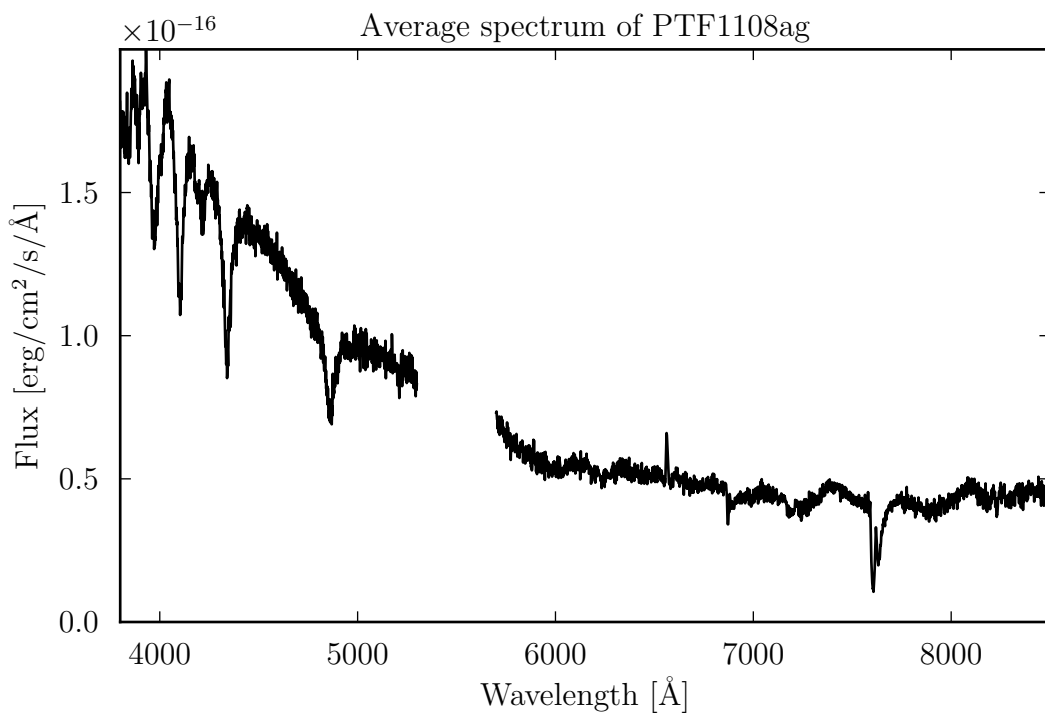


FIGURE 3.9: The averaged spectrum of PTF1108ag. The blue part of the spectrum clearly shows the white dwarf absorption lines. The red part of the spectrum shows atmospheric absorption bands, H α emission and TiO lines.

Chapter 4

Analysis and results

4.1 Orbital period and ephemeris

To determine the orbital period from the PTF data, the PDM method is used (see section 2.2). The PTF data have a very long (4 year) baseline, which is useful to determine the orbital period. However, PTF is severely undersampling the orbital period, making it difficult to keep track of the total number of orbits between eclipses. This results in so-called alias frequencies, as seen in figure 4.1. This figure shows the power spectral density versus the orbital period, but shows multiple solutions for the orbital period, the alias frequencies. This degeneracy can be broken by adding data which do not undersample the orbital period.

Ultracam is sampling the lightcurve every 2-3 seconds, easily meeting this criterion. To determine the orbital period with Ultracam data, the g' lightcurve is fitted using Lcurve. The free parameters in the fit are the ephemeris and the orbital period and result in $P_{\text{orb}} = 0.10602762 \pm 6.4 \cdot 10^{-7} \text{d}$ with an ephemeris $E = 55957.1219182 \pm 4.4 \cdot 10^{-6} \text{BJD}_{\text{TT}}$. This clearly breaks the degeneracy between the alias frequencies.

This solves the problem of the alias frequencies, and allows for a more accurate orbital period using the 4 year baseline of PTF. To determine the error of the PDM method on the PTF data, a bootstrap procedure is applied, see section 2.2. As can be seen in figure 4.2, the period obtained with the PTF data is more accurate, despite the lower sampling rate. The orbital period using the PTF lightcurve is determined to be $P_{\text{orb}} = 0.10602724 \pm 1.3 \cdot 10^{-7} \text{d}$. This higher accuracy is then used to constrain the frequency for the fit on Ultracam data, resulting in a slight more accurate ephemeris $55957.1219210 \pm 3.8 \cdot 10^{-6}$. The final result for the mid-eclipse times is:

$$BJD_{\text{TT}} = 55957.12192(1) + 0.106027(6) \cdot N \quad (4.1)$$

In figure 4.3 the PTF data are shown, folded on the orbital period determined above. The data points which show a significant lower flux are now all located

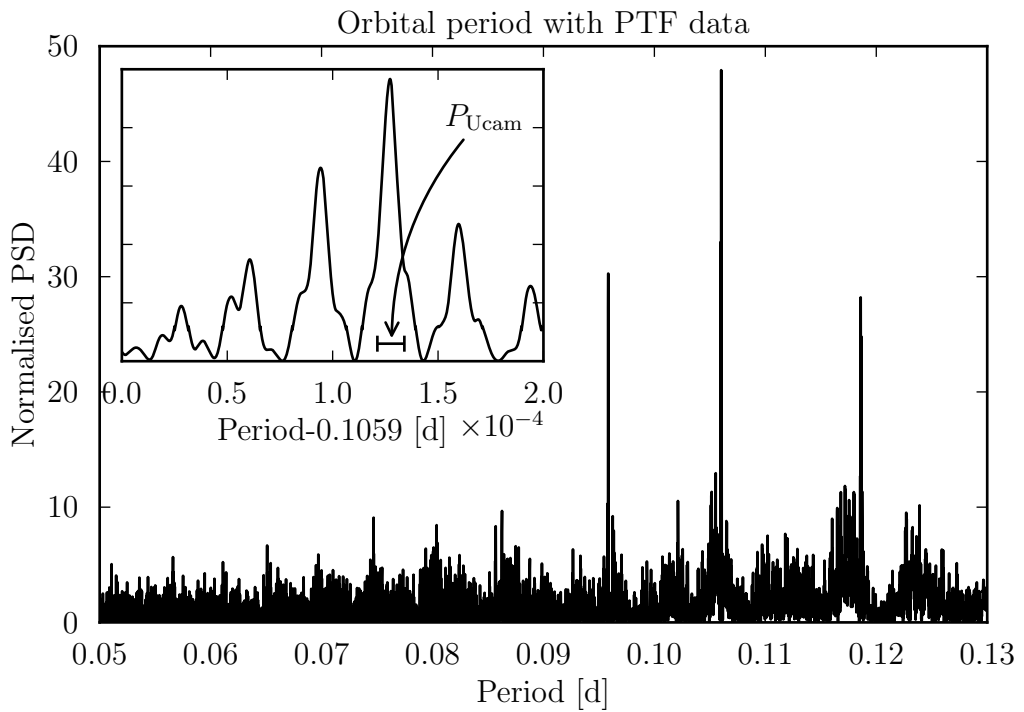


FIGURE 4.1: The results of the PDM analysis on the PTF R filter data. The y-axis shows the normalized power spectral density (PSD) and the x-axis gives the orbital period. The close-up plots the PSD near the main peak with the same y-scale. The errorbar show the Ultracam orbital period, with error multiplied by 10 for visibility.

near phase zero, the primary eclipse. The data also clearly shows a sinusoidal component, but features a few outliers. This is possibly the result of an incorrect measurement due to the nearby interloper.

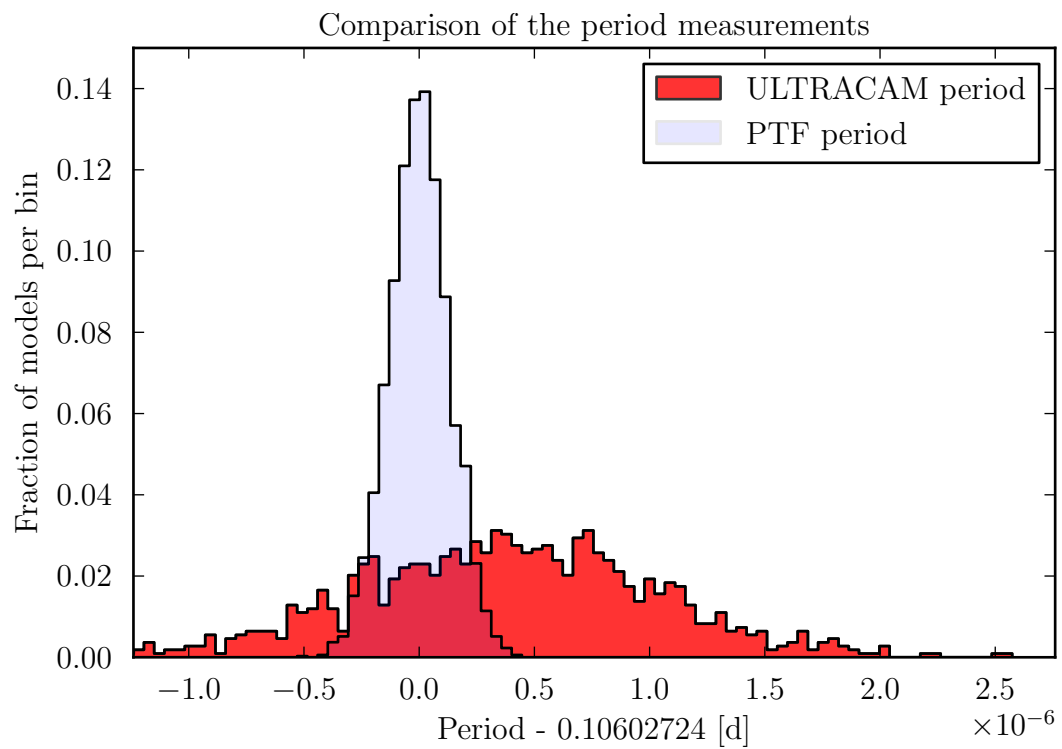


FIGURE 4.2: The orbital period of PTF1108ag. The red histogram is the orbital period with Ultracam, the blue histogram is using PTF.

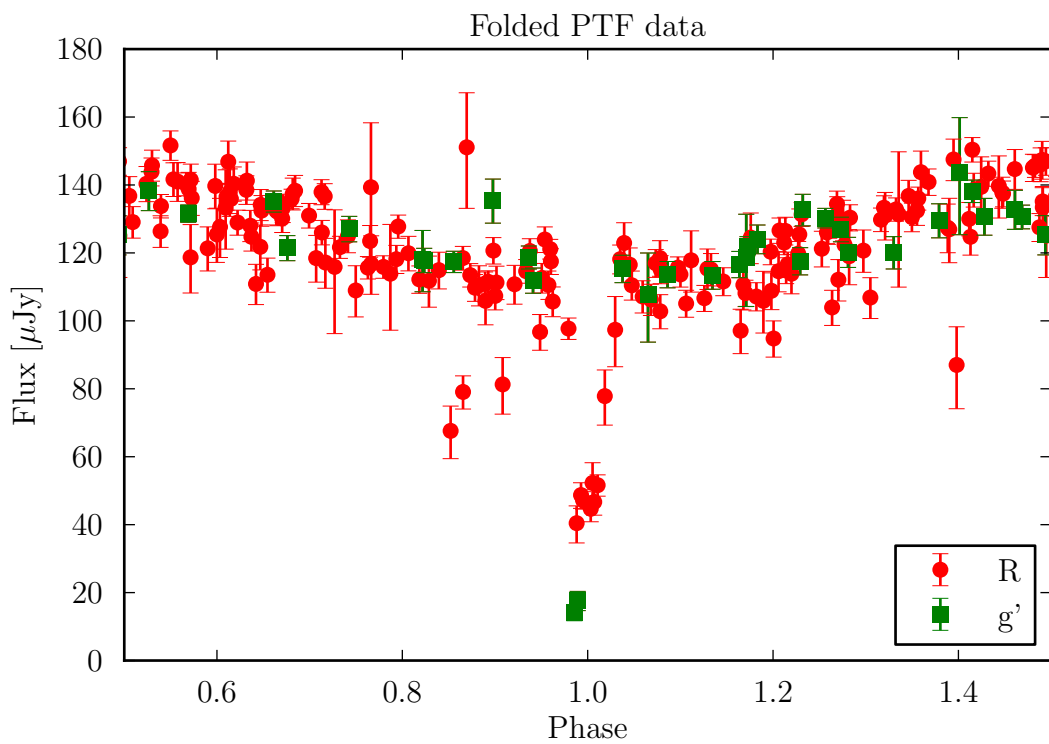


FIGURE 4.3: The PTF data folded on the orbital period. Red dots show the data from the Mould R filter, green squares show the SDSS g' data from PTF. The data have been converted to Janskys for easy comparison with the Ultracam data.

4.2 Luminosity and color

By combining the calibrated lightcurve and the fractions of the light contributing (see section 3.2), the individual flux can be calculated. To do this, the fraction is multiplied with the total amount of flux, determined from the extracted lightcurves. The red dwarf of PTF1108ag can now be calculated by subtracting the interloper from the in eclipse light. The flux of the white dwarf is relatively simple: this is the difference between the in- and out-eclipse light. The assumption made here is that the white dwarf is totally eclipsed. This is justified by the flat in eclipse lightcurve and the (almost) total absence of any light in the u' filter. The resulting magnitude per filter are given in table 4.1.

TABLE 4.1: The flux of the three components. The flux in the u' band is only determined for the white dwarf since no flux is measured during the eclipse.

Filter	Flux [μJy]		
	White dwarf	Red dwarf	Interloper
u'	114.8 ± 1.0	—	—
g'	106.0 ± 0.3	4.1 ± 0.4	10.9 ± 0.3
r'	69.6 ± 0.7	12.4 ± 0.8	33.0 ± 0.6
i'	54.3 ± 1.4	18.8 ± 1.6	94.7 ± 1.1

These luminosities in different bands can be used to calculate the colors. The color is the difference in magnitude between two filters, calculated with equation 4.2. Comparing these colors with colors of standards star or models gives information about the stellar properties. The red dwarfs are compared to the colors of SDSS red dwarfs from Bochanski et al. [8], see figure 4.5. The red dwarf of PTF1108ag is bluer than a M0 red dwarf, both in $r' - i'$ and $g' - r'$. The interloper corresponds to an M2-3 red dwarf, but the $g' - r'$ is lower (more blue) than the SDSS red dwarfs.

$$g' - r' = -2.5 \log_{10} \left(\frac{f_{g'}}{f_{r'}} \right) \quad (4.2)$$

Figure 4.4 shows the white dwarf and DA white dwarf models from Bergeron et al. [6], PTF1108ag corresponds roughly to a white dwarf of 25000K and a $\log(g)$ of less than 7.0. An import systematic error is the the interstellar reddening. This is a result of absorption of light by dust between us and PTF1108ag. This decreases the total amount of light received on earth in all wavelengths, but the effect is stronger in blue. The star thus looks redder than it really is. The correction shifts the star diagonally in a color-color diagram to more blue colors, the lower left in figure 4.4. The reddening determined by Schlafly and Finkbeiner [56] (taken from NED [40]) of a star 1kpc away is indicated by the dashed line. The correction moves the star to the higher temperatures and decrease the surface gravity slightly.

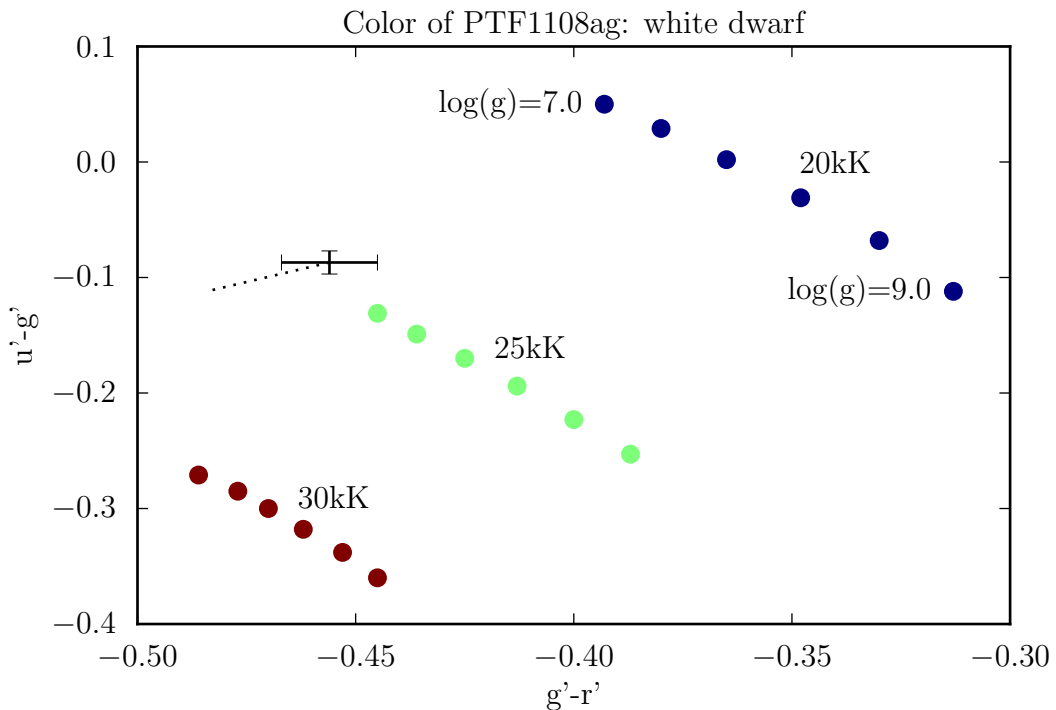


FIGURE 4.4: White dwarf colors (uncorrected for reddening), compared with data from Bergeron et al. [6]. The different track are for a $\log(g)$ range from 7.0 to 9.0, with 0.5 steps. The numbers indicate the lowest and highest $\log(g)$ values. The dashed line indicates the correction of reddening for a distance of 1kpc.

4.3 White dwarf temperature and red dwarf spectral type and distance

Stellar spectra are a valuable source of information to determine the temperature of a star. To determine the temperature and surface gravity ($\log(g)$) of the white dwarf and the spectral type of the red dwarf, the spectra are fitted with model spectra. A grid of models as used in Verbeek [66, p.177] is used. This is a combination of white dwarf model spectra (range: $T=5000\text{--}80000\text{K}$, $\log(g)=7.0\text{--}9.0$) taken from Koester et al. [29] and red dwarf spectra from Pickles [47], M0 to M6 spectral type. The spectra are normalized to a star at 10 pc and combined by taking the sum. To determine the best fitting model, a χ^2 minimization is used. The model spectra are resampled to the data (using linear interpolation) and multiplied by a factor to find the optimal fit. This multiplication factor (f) scales the total amount of flux received, and is related to the distance by $d = 10/\sqrt{f}\text{pc}$.

Data below 3930\AA are ignored in the fit as they show known artifacts from the DBS, as well as the region between $5000\text{--}6000\text{\AA}$ which is in between the red and blue arm. The red arm is fitted up to 8500\AA , with the atmospheric bands (O_2 absorption) at $\sim 6884\text{\AA}$ and $\sim 7621\text{\AA}$ ignored. Multiple data sets are used for the

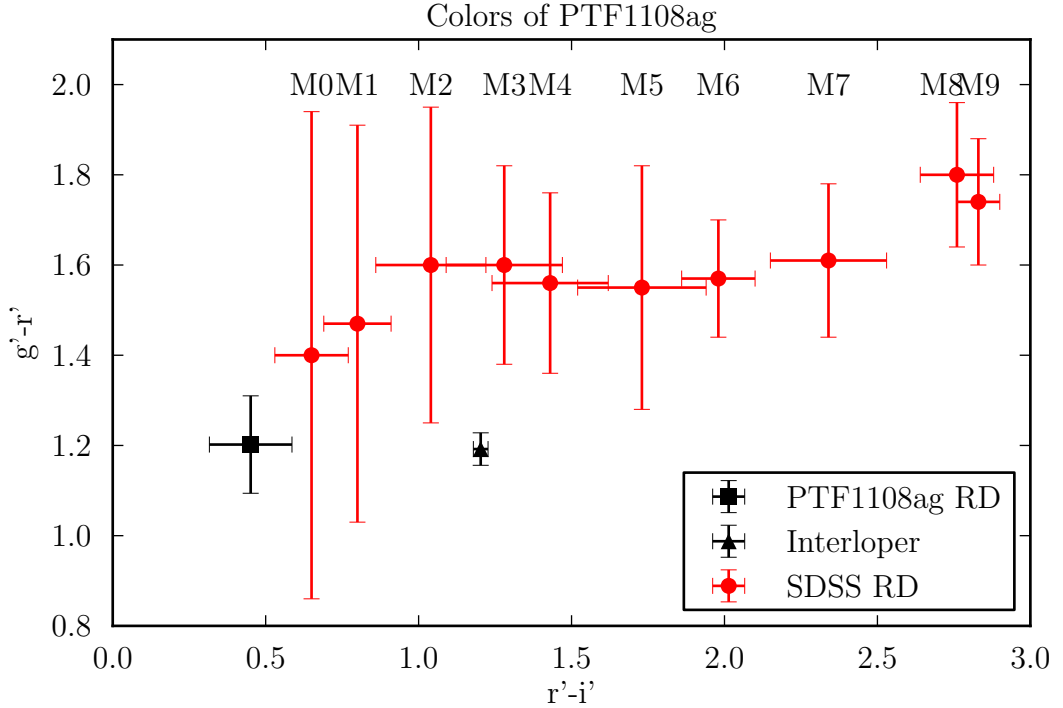


FIGURE 4.5: Red dwarf colors of the red dwarf in PTF1108ag (square) and the interloper (triangle). For comparison the data from Bochanski et al. [8] is plotted (circles).

fit, the average of all data, but also the averages of data between phases 0.4-0.6 and 0.8-0.2. This is done to see the effects of the irradiation of the red dwarf, which varies with phase (0.5 maximum irradiation, 0.0 minimum irradiation).

To determine the white dwarf temperature the average of all spectra is used, assuming the white dwarf does not vary with phase. A problem here is the Balmer emission from the red dwarf, filling the white dwarf absorption lines, complicating the fit. To determine the white dwarf temperature and $\log(g)$ only the blue part of the spectrum was fitted, but the central 16Å for every Balmer line was ignored. The result is shown in figure 4.6, with a minimum $\chi^2_{red} = 1.9$. The temperature of the white dwarf is 26000 ± 4000 K, with $\log(g) = 7.5 \pm 1$, with a distance of 835^{+142}_{-292} pc, see figure 4.8. This is checked by fitting the spectra from phase 0.8-0.2 only and using the complete Balmer line, which does not show any emission at these phases. This confirms the temperature and $\log(g)$, but the errors are larger due to a significant lower signal to noise (only 6 spectra are available in this phase range). Important to note is that the models have as lowest value a $\log(g)$ of 7.0. Figure 4.6 shows that the 1σ contour should contain lower surface gravity white dwarfs, of which models are not available.

Next the white dwarf and red dwarf are fitted simultaneously using the blue and red part of the spectrum. Using the average of all spectra and ignoring center of the Balmer lines, the red dwarf is determined to be a of spectral type $M5 \pm 1$, see

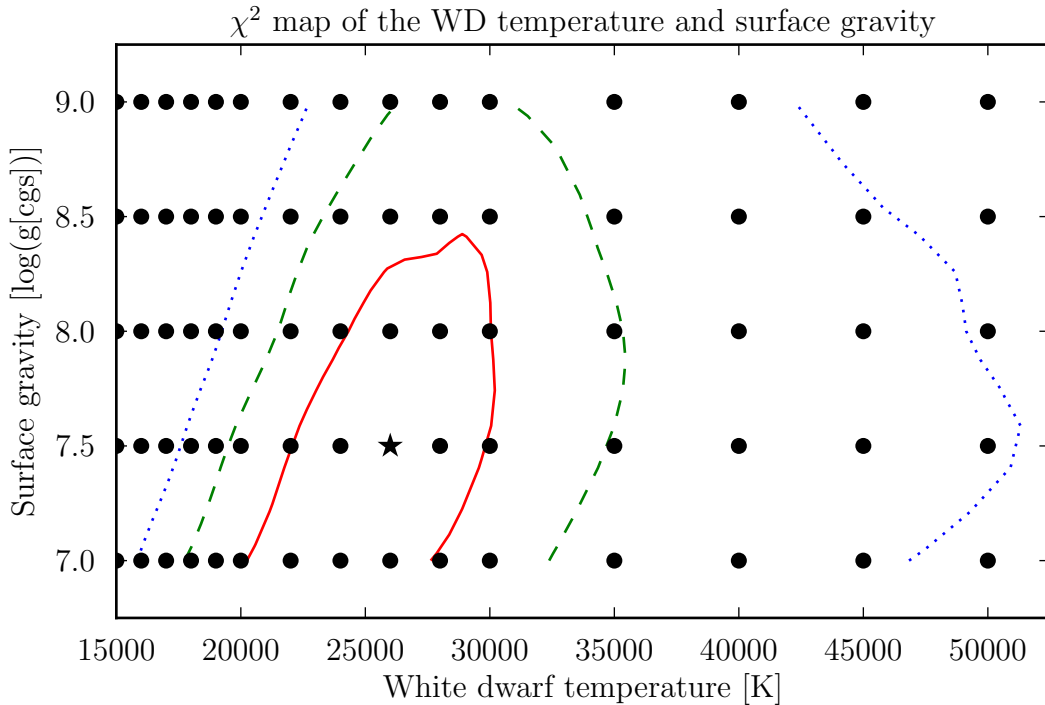


FIGURE 4.6: The χ^2 map of the spectrum fits on the white dwarf only. The dots indicate the model grid, the star indicates the best model and the lines give the $1\sigma, 2\sigma$ and 3σ contours.

figure 4.9. The spectral type is strongly correlated to the white dwarf temperature, because the white dwarf and red dwarf are fixed at the same distance, which fixes the luminosity ratio. If the white dwarf would have a higher temperature, the red dwarf also needs to be hotter, so the ratio between white dwarf - red dwarf luminosity is preserved. This can be seen in the shape of the 3σ contour in figure 4.9. Interesting to note is that the residual of the best fit seemed to peak in the middle, about 5500Å. This effect is also noted by van den Besselaar [61, p.100] and is possibly a result of interstellar reddening.

As was the case with the photometry, an important systematic error is the interstellar reddening. This absorbs the bluer photons more than the red photons. The result is that the white dwarf temperature is underestimated, and thus the luminosity. This also has an effect on the red dwarf, since both stars are forced to have the same distance. By fitting both spectra simultaneously, the ratio between the red dwarf and white dwarf flux is conserved. An underestimation of the white dwarf temperature causes the red dwarf temperature to be underestimated as well. Since the white dwarf has a higher flux and has a higher signal to noise ratio, it dominates the solution of the fit.

The result is that the spectrum fits the white dwarf reasonably, but the fit on the red dwarf is poor and only the slope of the continuum is fitted. To test if the features of the red dwarf (the TiO lines, see section 1.4) can be fitted as well, the

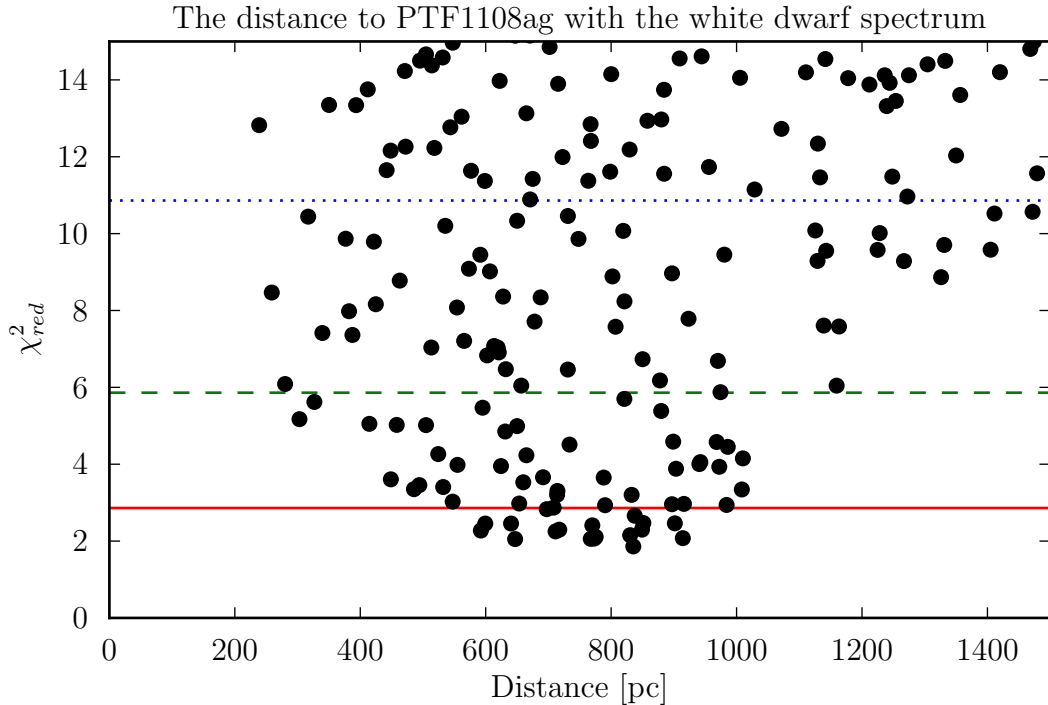


FIGURE 4.7: The distance determined using the white dwarf spectra and the model grid from figure 4.6. The best fit ($T = 26000\text{K}$, $\log(g) = 7.5$) has a reduced $\chi^2 = 1.9$. The lines dots indicate fits to spectra, the horizontal lines are the 1σ , 2σ and 3σ lines

best fit white dwarf model spectrum is subtracted from the data. The residual is fitted with the models of individual red dwarfs. The spectrum available for the interloper, suspected to be a red dwarf as well, is also fitted with these model spectra. The results are shown in figure 4.10.

The spectral type of the PTF1108ag red dwarf is an $M4V \pm 1$ a distance of 1340^{+416}_{-424} pc¹, which is consistent with the fit of both components. A note however is that only the average of the spectrum between 0.8 and 0.2 is fitted. The fit of the average spectrum between 0.4 and 0.6 as well, and resulted in a lower spectral type, $M3V \pm 1$, with the corresponding distance 1060^{+405}_{-249} pc. But looking at the fit, only the general trend is fitted, and the features of for example the TiO lines were underestimated. This is likely the result of the strong irradiation, which distorts the spectrum and the line profiles.

Another method to determine the spectral type is to look at the TiO5 index. Reid et al. [54] determined the correlation between the TiO 5 line band and the spectral type:

$$S_p = -10.775 \text{ TiO5} + 8.2 \quad (4.3)$$

¹The error on the distances are determined from the fits to the M3V and M5V spectral types

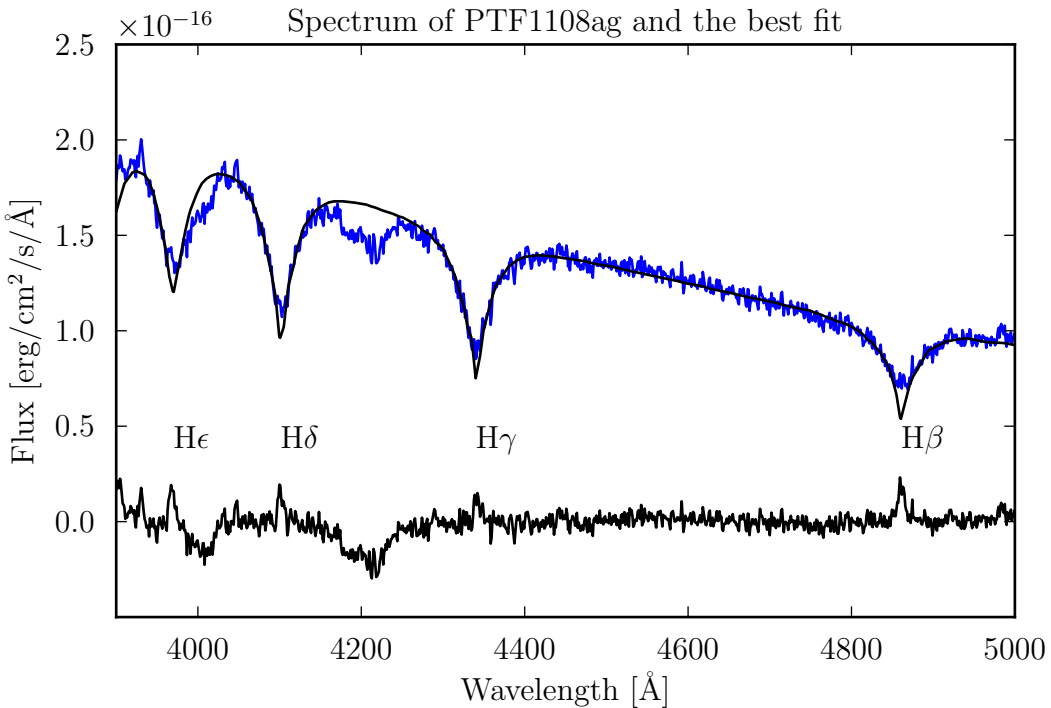


FIGURE 4.8: The average spectrum of the white dwarf, the best fit and the residual. The best fit ($T = 26000\text{K}$, $\log(g) = 7.5$) has a reduced $\chi^2 = 1.9$. The residuals clearly show a peak near the Balmer lines, which are the result of the irradiation effect on the red dwarf. The variations on the blue side are detector artifacts.

with the TiO5 index defined as the flux at $7126 - 7135\text{\AA}$ divided by the flux at $7042 - 7046\text{\AA}$. This method has been applied to the individual spectra, after fitting and subtracting the white dwarf, the result is shown in figure 4.11.

The figure shows a large variability in spectral type, decreasing when the irradiated side comes into view. This is not surprising, as the irradiated side of the red dwarf is hotter, and thus has a lower spectra type. The magnitude of the difference is larger than expected, while the fit of the spectrum at phase 0.5 give a spectral type of $M3 \pm 1$, the TiO5 index is a lot lower.

This discrepancy could be due to the fact that the lines are affected different by irradiation than the entire spectrum. Another possibility is that the white dwarf is not subtracted correctly. At 7000\AA , the white dwarf is still contributes significantly to the total flux, and incorrectly subtracting the white dwarf in order to calculate the ratio, can lead to significant systematic errors.

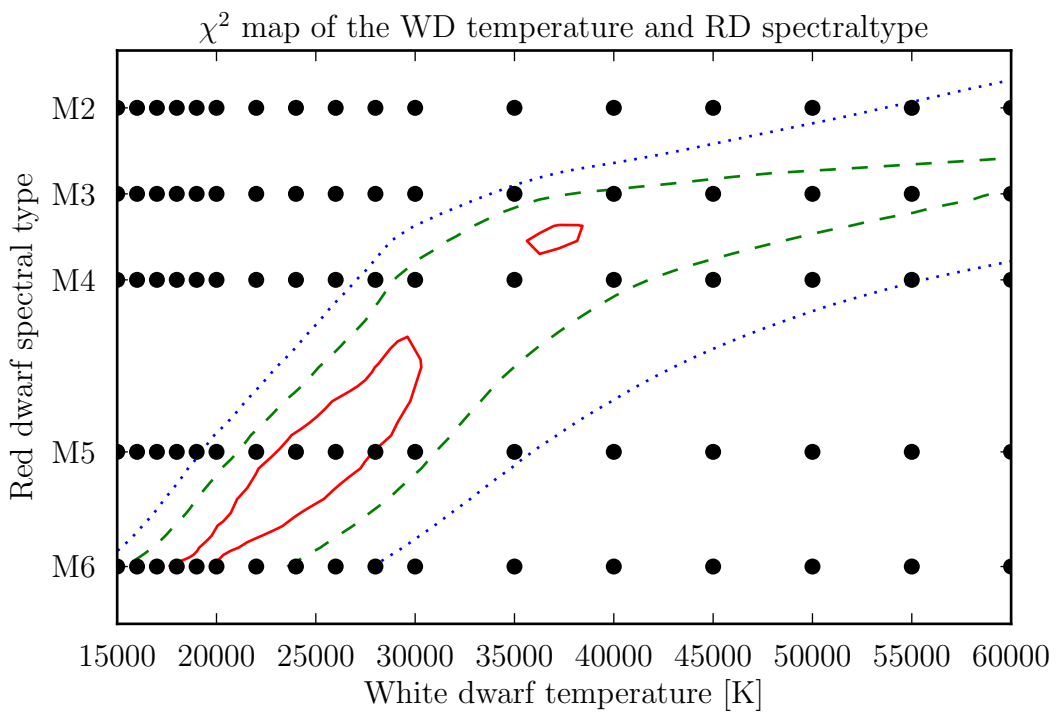


FIGURE 4.9: The χ^2 map of the spectrum fits on the white dwarf ($\log(g)=7.5$) vs the red dwarf temperature. The dots indicate the model grid, the star indicates the best model and the lines give the $1\sigma, 2\sigma$ and 3σ contours.

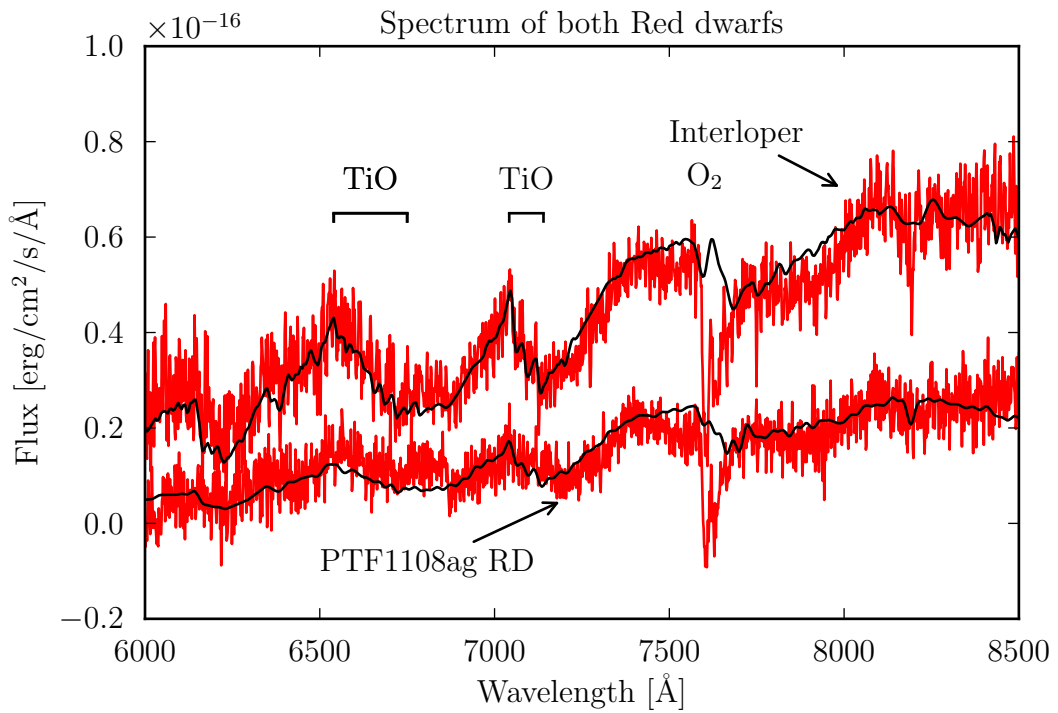


FIGURE 4.10: The spectrum of PTF1108ag at phase 0.8-0.2 with the white dwarf subtracted and the spectrum of the interloper with the best fit. The spectral type of the PTF1108ag RD is an M4V, but both M5V and M3V have similar χ^2 values (about 2.5). The interloper is best fitted with an M3V spectrum with an uncertainty of 1 spectral type (best fit $\chi^2 = 1.2$).

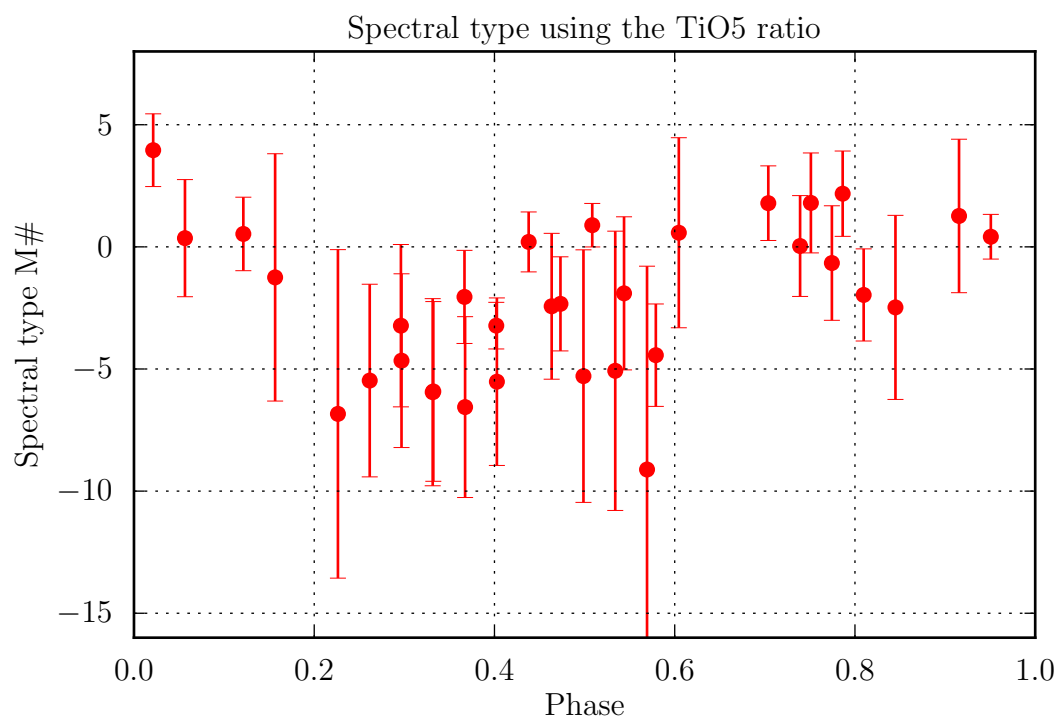


FIGURE 4.11: The spectral type versus phase, determined using the TiO₅ index.
The spectral type is clearly lower at the phase 0.5.

4.4 Radial velocity variations

The radial velocity is important because it can be used to calculate the mass of both components in the binary, see chapter 2. Since PTF1108ag features absorption and, in part of the orbit, emission lines, this should be measurable. The complication arises because the emission and absorption lines all have the same wavelengths, the hydrogen Balmer lines. To measure both the white dwarf and the red dwarf radial velocities multiple methods are applied.

The first method is to cross-correlate the individual spectra with the average, using the RV/fxcor package in IRAF. Before doing the actual cross-correlation, the continuum of the spectra is fitted and used to normalise the spectra, and all spectra are used to make an average spectrum. To determine the radial velocity of the white dwarf, the absorption lines $H\beta - \epsilon$ are used, and for the red dwarf radial velocity, the $H\alpha$ emission line. The result is shown in table 4.2 as method A, with the radial velocity as function of phase shown in figure 4.12.

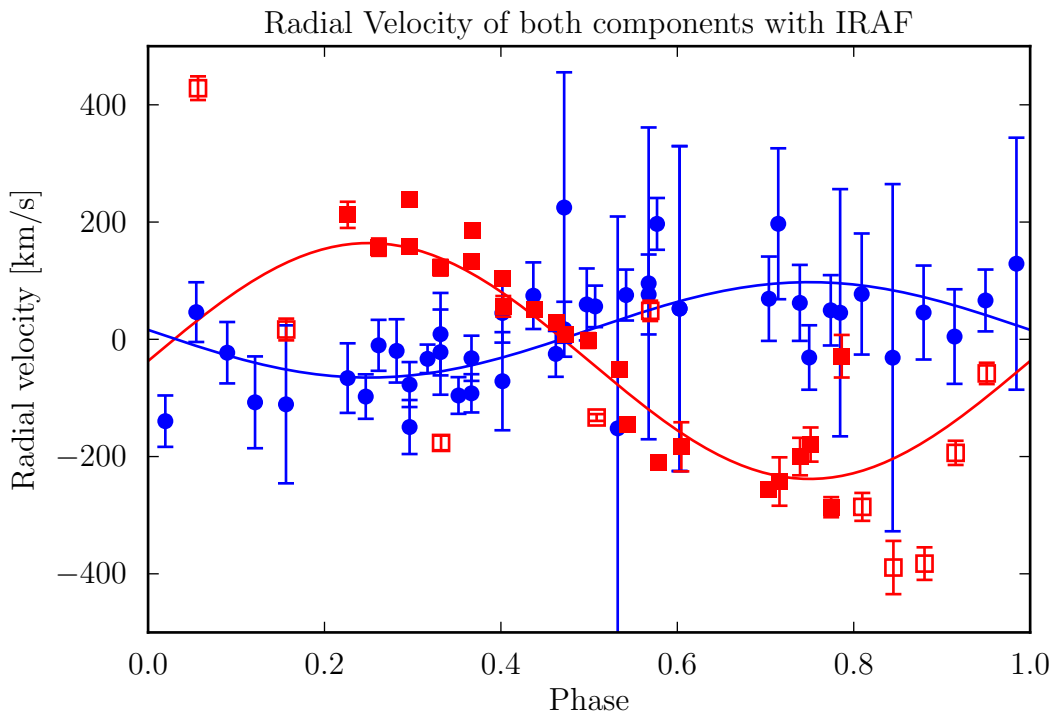


FIGURE 4.12: The radial velocity of the $H\alpha$ emission line and White Dwarf Balmer absorption lines as measured with cross-correlation with IRAF. Filled symbols indicate they are used in the fit, open symbols not used. Squares indicate the red dwarf radial velocity, dots indicate the white dwarf radial velocity.

The data is fitted with a sinusoidal using a chisquare minimization method. The phase of the spectra is determined using the orbital period obtained from the photometry. Since the orbital period is known very accurately, the phase offset of the fit is forced to zero, eliminating one free parameter. The two remaining

parameters of the fit are the amplitude of the sinusoid and a constant velocity. All points for the red dwarf between phase 0.8 and 0.2 are ignored, as very little to no emission is measured. The errors are determined using the bootstrap method with errors on the data points rescaled to $\chi^2 = 1$. In addition, outliers which are more than 5 sigma away from the fit are rejected, using a few iterations.

The cross-correlation method as applied has a few drawbacks. The average spectrum used for the cross-correlation has not been corrected for the shift of the individual spectra. This will tend to widen the absorption and emission lines, which could influence the cross-correlation. Another problem is the emission of the red dwarf, which has not been removed in the cross-correlation.

To improve the radial velocity measurements, the lines are also fitted with a Gaussian profile. The software package used for this is MOLLY, written by T. Marsh. Before fitting, the continuum is removed by fitting a polynomial to the continuum between the absorption lines. The H α line is fitted with a single Gaussian, with free parameters the shift due to the radial velocity and the height of the emission line. The width is determined using the average spectra between phases 0.4 and 0.6, 8Å. This is fixed in the fitting procedure to avoid the fitting to move to very wide and shallow Gaussian fits.

The radial velocity of the absorption lines are more difficult to measure. These are fitted with a double Gaussian, one in emission and one in absorption, both with fixed widths, determined using the average. The depth of the profiles are allowed to vary, to account for differences in irradiation and possible problems with normalization. Since the absorption profiles are very wide and the shift is less than one pixel, measuring the shift of the individual absorption lines is not possible. Using the same radial velocity shift for all absorption lines does give a high enough precision to measure the radial velocity variation. The result of this method is shown in table 4.2 as method B and in figure 4.13.

This method does have the advantage of separating the emission and absorption components of the Balmer lines. However the assumption of a Gaussian profile is unlikely to be correct for the absorption lines, potentially distorting the radial velocity. Another difficulty is the interplay between the two components, especially if the emission is on the edge of an absorption line. This could shift the fitted absorption profile more than is required, as it is most sensitive to the minimum of the lines.

In an attempt to investigate the influence of the double peaked profile on the radial velocity, a third method is attempted. The model spectra of the white dwarf were first fitted and subtracted, so only the red dwarf remained. The remaining emission lines are now fitted with a single Gaussian. The result is shown in figure 4.14, method C in table 4.2.

The radial velocity of the white dwarf is consistent between the two different methods applied. However the errors are very large, and the scatter in the fit of method B high. It is uncertain if the real radial velocity is fitted by both these fits

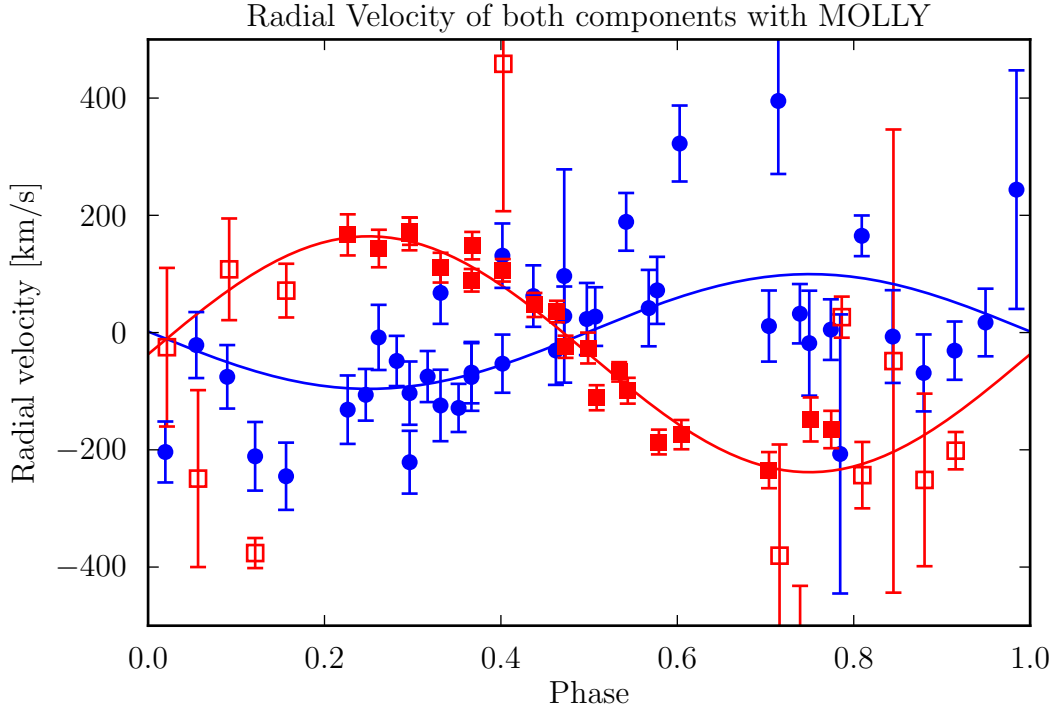


FIGURE 4.13: The radial velocity measurements and fit of the H α emission line and white dwarf Balmer absorption lines as measured with line fitting with MOLLY.

TABLE 4.2: Radial velocity measurements. E/A=Emission/Absorption. Methods are explained in the text.

E/A	method	Radial velocity [km/s]				
		H α	H β	H γ	H δ	H ϵ
E	A	236 \pm 14	-	-	-	-
	B	201 \pm 13	229 \pm 18	203 \pm 29	269 \pm 30	-
	C	193 \pm 14	196 \pm 16	191 \pm 21	221 \pm 18	231 \pm 12
A	A	-		-81 \pm 15		-
	B	-		-98 \pm 22		-

and how much these measurements suffer from mixing with the red dwarf spectral features.

The radial velocity of the emission features is mostly consistent with each other, except for one outlier, the radial velocity of H ϵ . The difference between methods are small, with slightly higher velocities for method A&B versus C. The differences are however within the error margins. The differences between emission lines are also within error margins. Emission lines are formed by layers of different depth in the red dwarf atmosphere. These differences are however small, and are not be detectable with such large uncertainties.

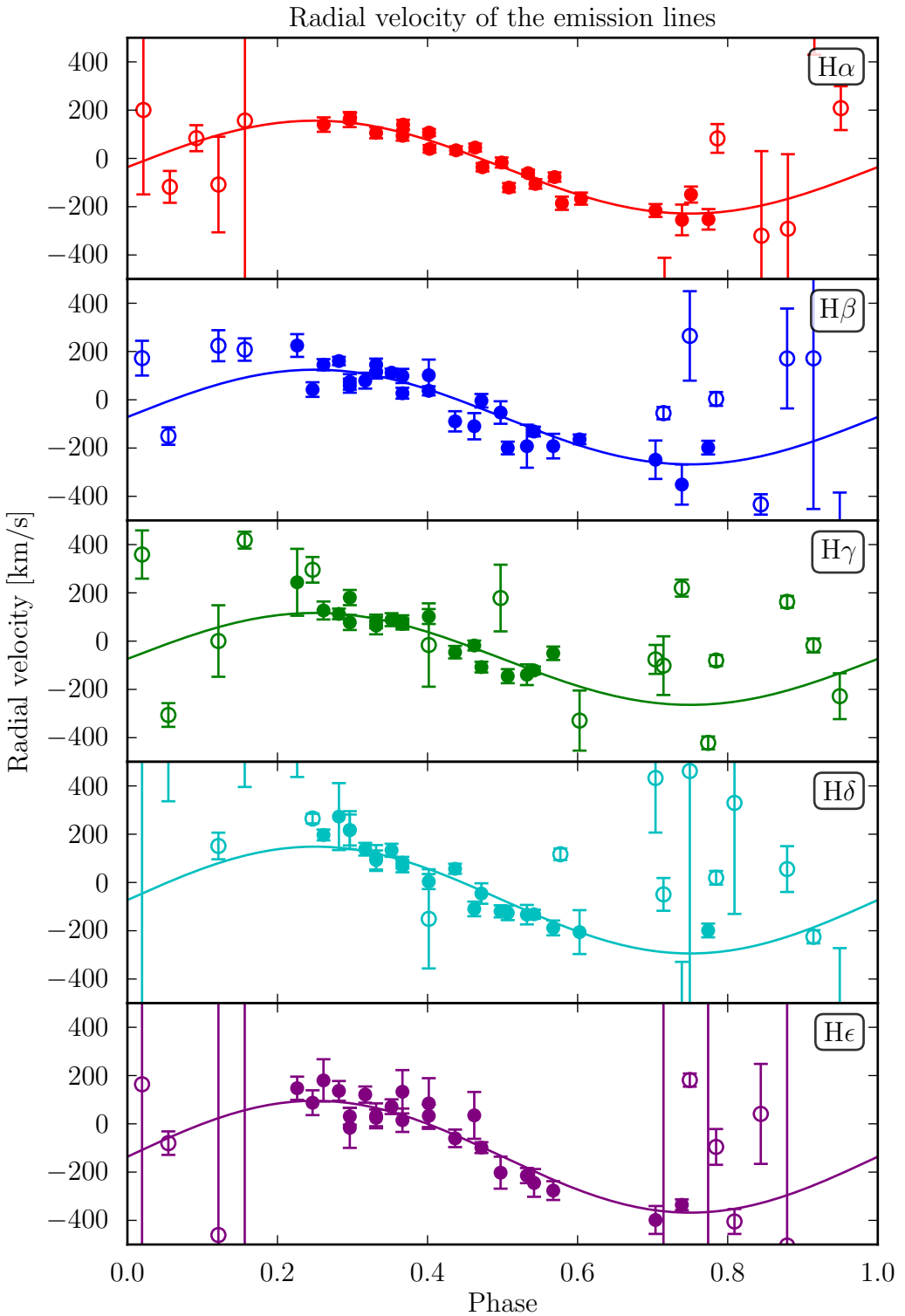


FIGURE 4.14: The radial velocity measured by fitting a single Gaussian to the emission line profile after subtracting the white dwarf.

The average of all lines over all methods is 215 ± 6 km/s for the emission line, and 85 ± 15 km/s for the absorption lines. This results in a mass ratio $m_2/m_1 = q = 0.40 \pm 0.07$. The given errors are the statistical errors and systematic errors should also be considered. One of systematic errors caused by the fact that the radial velocities for both stars are determined from spectral features at the same wavelength. Despite the effort made to counter this, the radial velocity measurements could still be affected by this. A second problem is that the emission from the red dwarf originates from the irradiated side of the red dwarf. Since the red dwarf has a non-zero radius, the irradiated side is moving at a lower orbital velocity than the center of mass. The measured radial velocity is thus an underestimate of the center of mass radial velocity.

An attempt to determine the magnitude of this effect is made by modeling an irradiated sphere, with the approximate dimensions of a white dwarf - red dwarf binary. The result is that the radial velocity is underestimated by 20%, see figure 4.15, and the amount of emission has a distinct shape as function of phase. This is of course a very crude model, as it assumes a zero Kelvin spherical star, a point source as irradiator and a one-to-one relation between irradiation and emission. But this does illustrate the magnitude of the effect. To determine the real irradiation correction, a more advanced model needs to be used. This model should also be able to predict the amount of emission as function of phase, which can be used to put additional constraints on the effect. See for a similar system featuring this effect Parsons et al. [46] and a more extreme binary van der Hooft et al. [63].

The amount of emission as function of phase could potentially be used to determine the irradiation correction. Figure 4.16 shows the equivalent width of the emission lines in the spectrum of PTF1108ag. The equivalent width is defined as:

$$EW = \int_{line} \frac{F_{line}(\lambda) - F_{cont.}(\lambda)}{F_{cont.}(\lambda)} d\lambda \quad (4.4)$$

and measures the flux in the line compared to the continuum level. The equivalent width of all emission lines shows variability correlated with the orbital phase. The signal peaks at a phase of 0.5, when the largest amount of irradiated red dwarf surface is visible. This supports the assumption that the emission lines are a result of the reflection effect. The exact shape of the emission as function of phase depends on the shape, local surface brightness, and optical depth of the red dwarf. The differences between these models are quite small, and thus high signal to noise spectra are needed to do this analysis, see Parsons et al. [46] for an example.

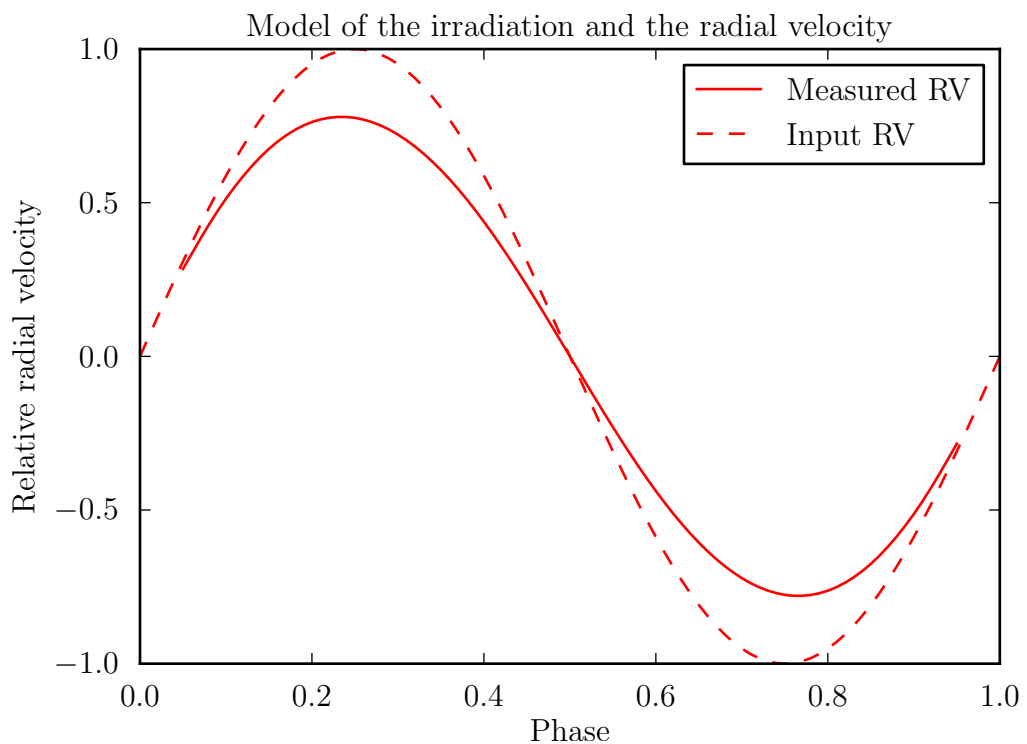


FIGURE 4.15: The radial velocity as measured from the light compared to the input radial velocity. The parameters are $q = 0.34$ and $R_{RD}/a = 0.25$. The result is a 20% difference in radial velocity from the center of light compared to the center of mass.

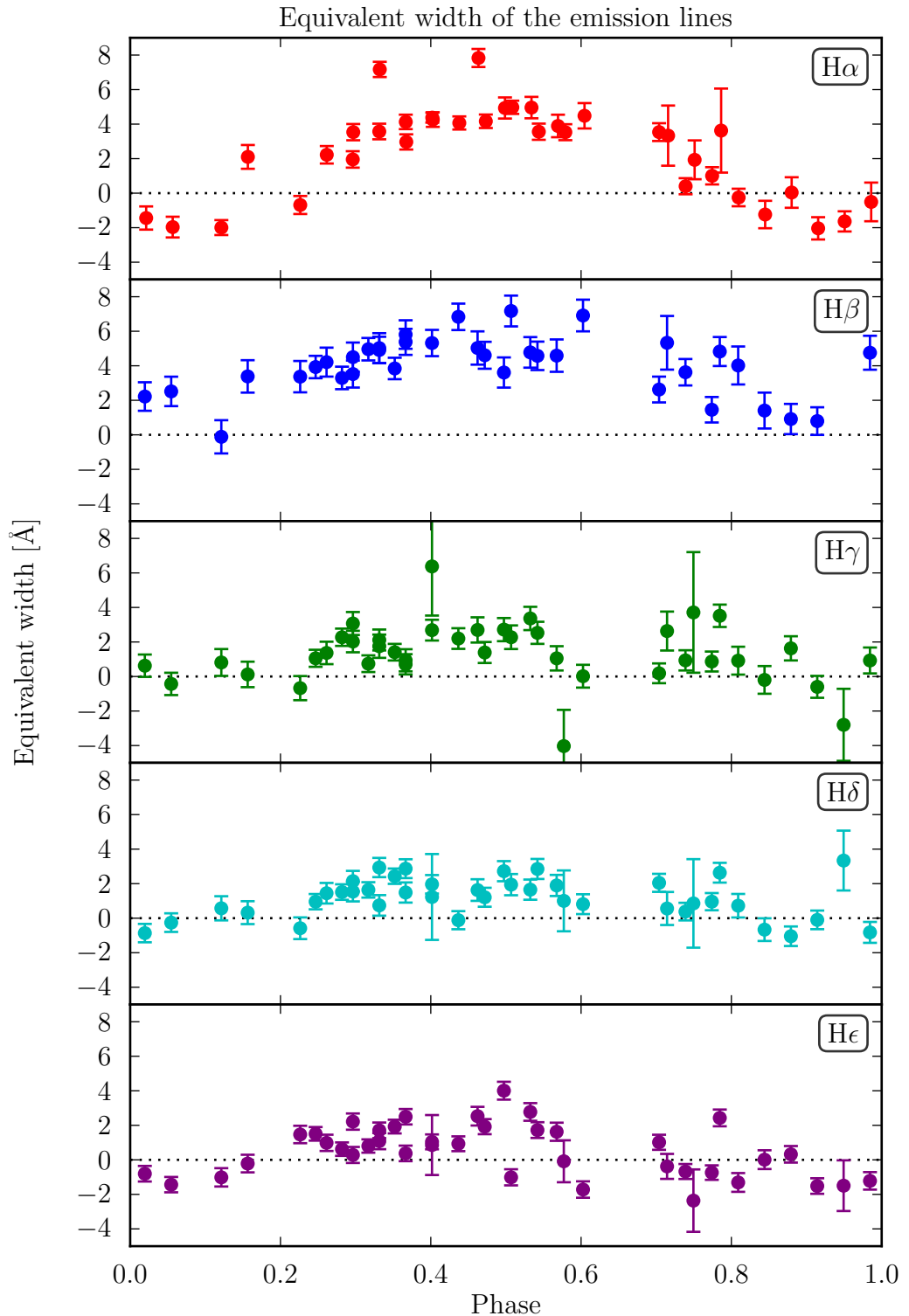


FIGURE 4.16: The equivalent width of the emission lines as function of phase. The equivalent width is measured after subtraction the white dwarf model spectrum.

4.5 Light curves

To model the lightcurves of PTF1108ag, a Lcurve model with a white dwarf and red dwarf is used. The free parameters in the fit are the relative radii (R_1/a and R_2/a), inclination (i), absorption coefficient/albedo (α) and the mass ratio (q). The mass ratio is not fixed, as there is a large uncertainty (both statistical and systematic) in both radial velocities. The temperature of the white dwarf is kept fixed at 26000K, as determined by the spectral fits. The reasons for this is that if both temperatures and absorption factor are free parameters, these three parameters are totally degenerate.

The limb darkening and gravity darkening of the red dwarf are kept fixed. Taken from Claret and Bloemen [13], for a red dwarf with temperature $T = 3000$ and a $\log(g)$ of 5.0. The limb darkening formula used is the quadratic formula:

$$I(\mu) = 1 - a(1 - \mu) - b(1 - \mu)^2 \quad (4.5)$$

with μ the incident angle, see Claret and Bloemen [13] and appendix B. The gravity darkening is power law related to the local gravity, normalised to the surface gravity nearest to the second Lagrange point (g_r) (see Claret and Bloemen [13]):

$$I(g) \propto (g/g_r)^\gamma \quad (4.6)$$

The values for the parameters given in table 4.3. For the white dwarf no limb darkening and gravity darkening is used.

TABLE 4.3: Limb darkening parameters and gravity darkening parameters from from Claret and Bloemen [13] for a 3000K, $\log(g)=5$ star per filter as used in the Lcurve models. Parameters as in the formulas 4.5 and 4.6

	u'	g'	r'	i'
a	0.5866	0.6720	0.6364	0.4193
b	0.2959	0.2660	0.2521	0.4109
γ	0.2896	0.5360	0.3957	0.2896

The data used for the fit are detrended, folded on the orbital period and binned. The phases near the eclipses ($\phi = 0.95 - 0.05$ and $\phi = 0.45 - 0.55$) are sampled at 4000 bins/orbits, and the rest is sampled at 400 bins per orbit in g', r' and i' . The u' filter has been binned to half these values, since the sampling is a lot lower. This is done to speed up the model calculations.

These parameters solutions are strongly correlated, see section 2.2 and figure 4.17. The reason the white dwarf temperature is kept fixed is to constrain the solution space. Despite this, all parameters show strong correlations in the parameter spaces. This caused the problem that the Markov Chain has difficulties reaching the outer ends of the narrow valleys in χ^2 space. To combat this correlated jump distributions are used. This was done in an interactive way until the differences between the parameters ranges was negligible, typically after 3 iterations. Despite

TABLE 4.4: The results from fitting the lightcurves with Lcurve. R_1/a and R_2/a are the radii relative to the orbital separation of the white dwarf and red dwarf. The inclination i , q the mass ratio, T_2 the red dwarf temperature and α the reflection efficiency.

Parameter	u'	g'	r'	i'
$r1/a$	0.0256 ± 0.0054	0.0273 ± 0.0023	0.0330 ± 0.0034	0.028 ± 0.0044
$r2/a$	0.280 ± 0.064	0.280 ± 0.026	0.232 ± 0.026	0.25 ± 0.040
i [deg]	79.5 ± 3.0	80.1 ± 1.1	81.6 ± 1.3	80.0 ± 2.0
T_2 [K]	5206 ± 542	3805 ± 154	4313 ± 299	3860 ± 421
q	0.22 ± 0.13	0.150 ± 0.037	0.130 ± 0.036	0.198 ± 0.075
α	1.94 ± 0.25	1.270 ± 0.086	1.60 ± 0.30	1.31 ± 0.43

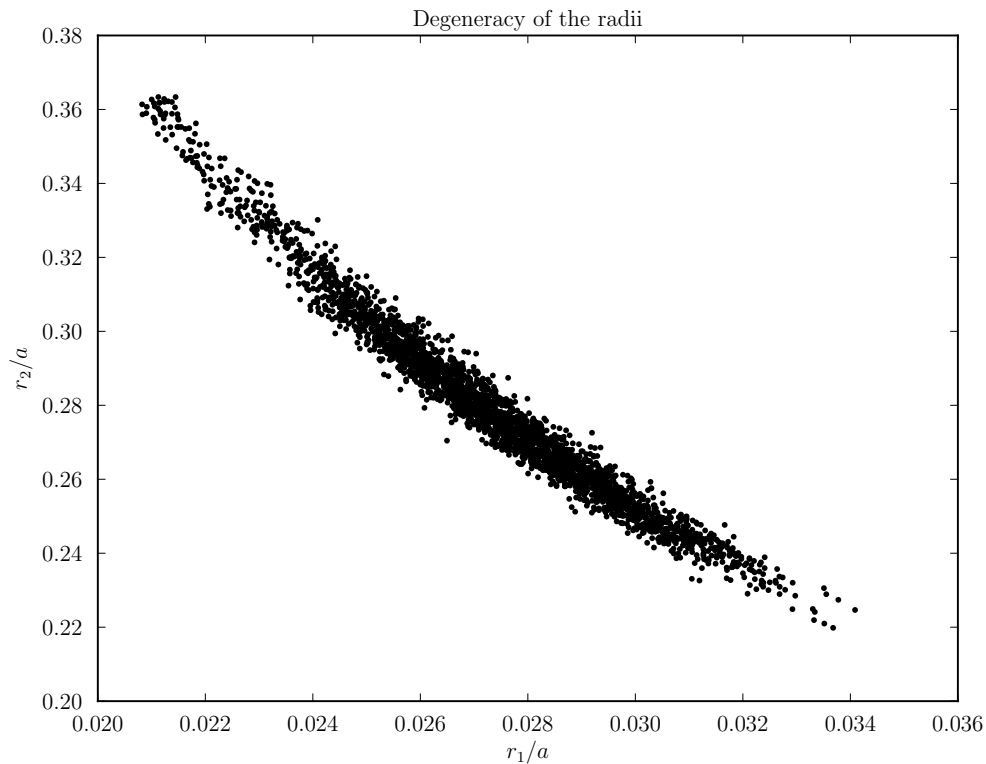


FIGURE 4.17: An example of a chain in the g' , showing the degeneracy between the radii of both stars. Only a tenth of the datapoints is shown for clarity.

this the χ^2 maps still show signs of a cutoff at the sides, and the errors on the parameters could still be underestimated. The errors which are giving in table 4.4 are determined using the Lcurve. The spread in solutions is mainly caused by degeneracies, and thus combining the measurements of the different bands would underestimate the real spread in solutions. An example of the degeneracies are the radii and inclination. For a higher inclination the white dwarf radius increases and the red dwarf radius decreases, which is expected by looking at equation 2.14.

4.6 Mass and orbital separation

The mass of both components is determined using equation 2.3. This requires the radial velocities, the orbital period and the inclination. The mass for the white dwarf is $0.221 \pm 0.027 M_{\odot}$ and the red dwarf $0.088 \pm 0.025 M_{\odot}$, which gives an orbital separation $a = 0.63 \pm 0.03 R_{\odot}$. However, the measured radial velocity of the red dwarf measures the radial velocity of the center of light, not the center of mass. The radial velocity of the center of mass results in a higher mass, especially for the white dwarf.

To determine how this increase in radial velocity changes the mass, a range red dwarf radial velocities is used to calculate corresponding range in mass, see 4.19. As can be seen in the figure, the mass of the white dwarf depends strongly on the red dwarf radial velocity, K_2 . For example, an increase 20% of K_2 results in a mass of $0.34 \pm 0.04 M_{\odot}$, an increase of 50% in mass. The mass of the red dwarf and the orbital separation increase as well, but not that drastically, $0.12 \pm 0.03 M_{\odot}$ and $0.72 \pm 0.03 R_{\odot}$.

4.7 Mass and radius

Using all the data obtained, the mass and radius of both stars can be calculated. A word of warning interpreting this data, the inconsistency of the mass ratio and the more than 100% reflection efficiency are unresolved problems. These are not solved in this paper and require more data or better models, see chapter 5.

The white dwarf mass and radius, $M = 0.22 \pm 0.03 M_{\odot}$ & $R = 0.017 \pm 0.003 R_{\odot}$, is compared to theory and other observations in figure 4.20. As can be seen in the figure, the mass and radius of PTF1108ag are position below the zero temperature relation of Eggleton (from Verbunt and Rappaport [68]). This changes when the irradiation correction is taken into account, increasing the mass and radius of the white dwarf to $M = 0.34$ & $R = 0.020 R_{\odot}$ for a 20% increase in radial velocity. This puts it near region of the expected values since the temperature increases the radius, but comparing it to models by Panei et al. [44], it is still to small that specific temperature and mass. Looking at other white dwarfs in post common

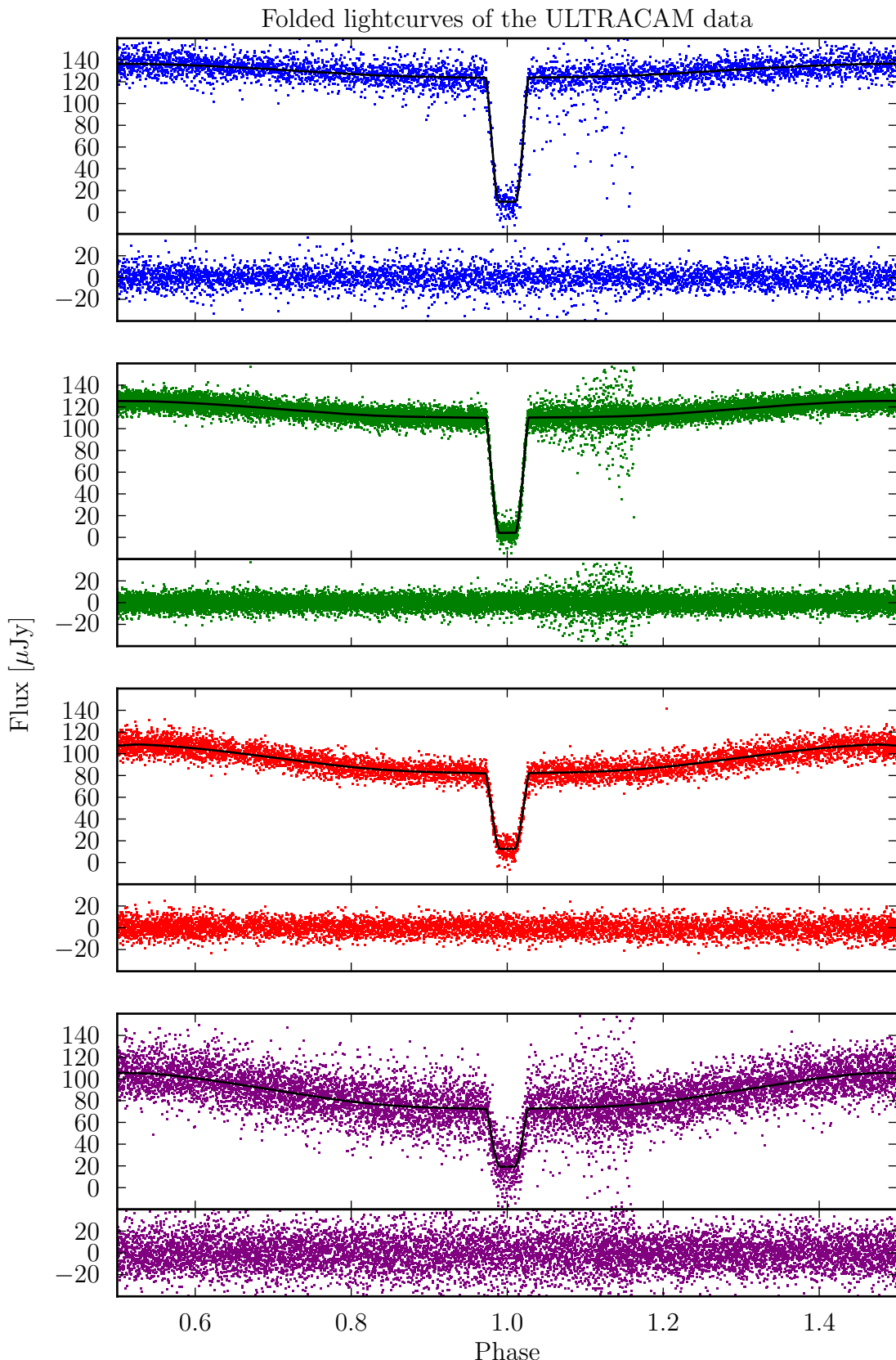


FIGURE 4.18: The lightcurves of the ULTRACAM data folded to the orbital period. The points show the data, the black line the best fit and the lower panel give the residual. The filters are from top to bottom u' , g' , r' and i' .

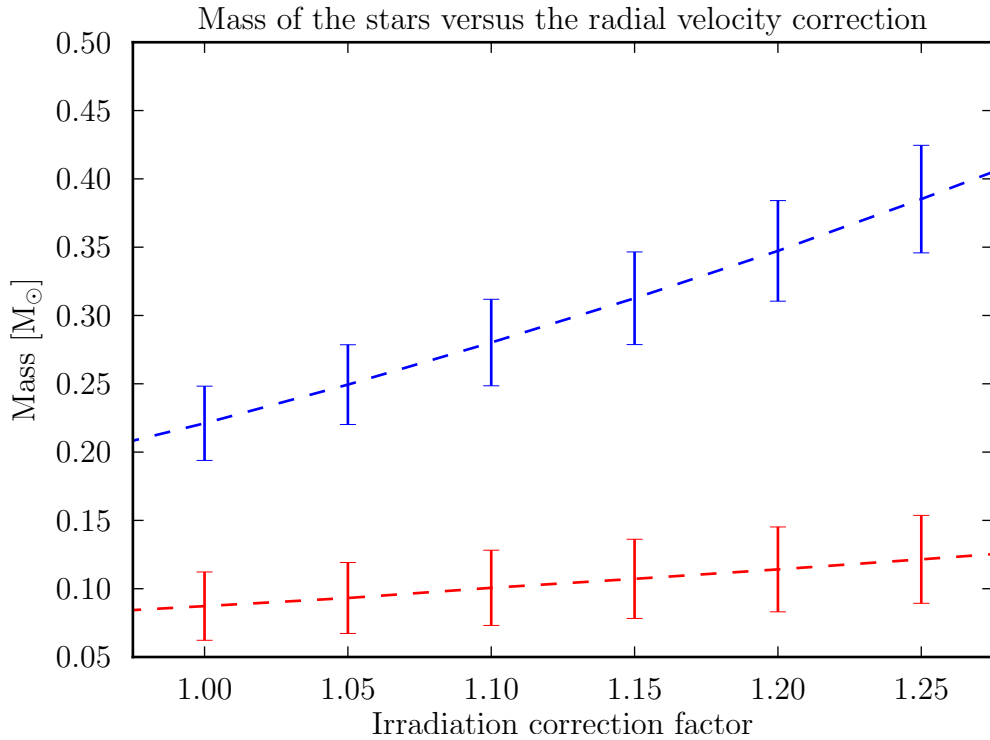


FIGURE 4.19: The mass of the white dwarf (blue) and the red dwarf (red) as function of the radial velocity correction. The white dwarf mass is affected stronger since this is mainly determined by the red dwarf radial velocity.

envelope binaries, PTF1108ag has a low mass, even taking into account the irradiation correction. Comparing the mass and radius to the surface gravity, shows that it is consistent with the measurements from the spectra, about $\log(g) = 7.5$.

The red dwarf mass and radius, $M = 0.08 \pm 0.02 M_{\odot}$ & $R = 0.016 \pm 0.03 R_{\odot}$, are plotted in a similar way, see figure 4.21. Comparing data with the theoretical mass radius of 1Gyr old red dwarfs from Baraffe et al. [4]. This shows that the red dwarf is larger than expected from the mass. This is not surprising, as this difference is also found in other close red dwarf binary systems, see section 1.4. A high correction for the red dwarf radial velocity would result in a more consistent result with the measurement of the spectra type (a 20% correction results in: $M = 0.11 M_{\odot}$ & $R = 0.018 R_{\odot}$), which is $M4 \pm 1$. The difference however remains large, which could be a result of the irradiation effect, increasing the temperature of the red dwarf, and thus decreasing the spectral type.

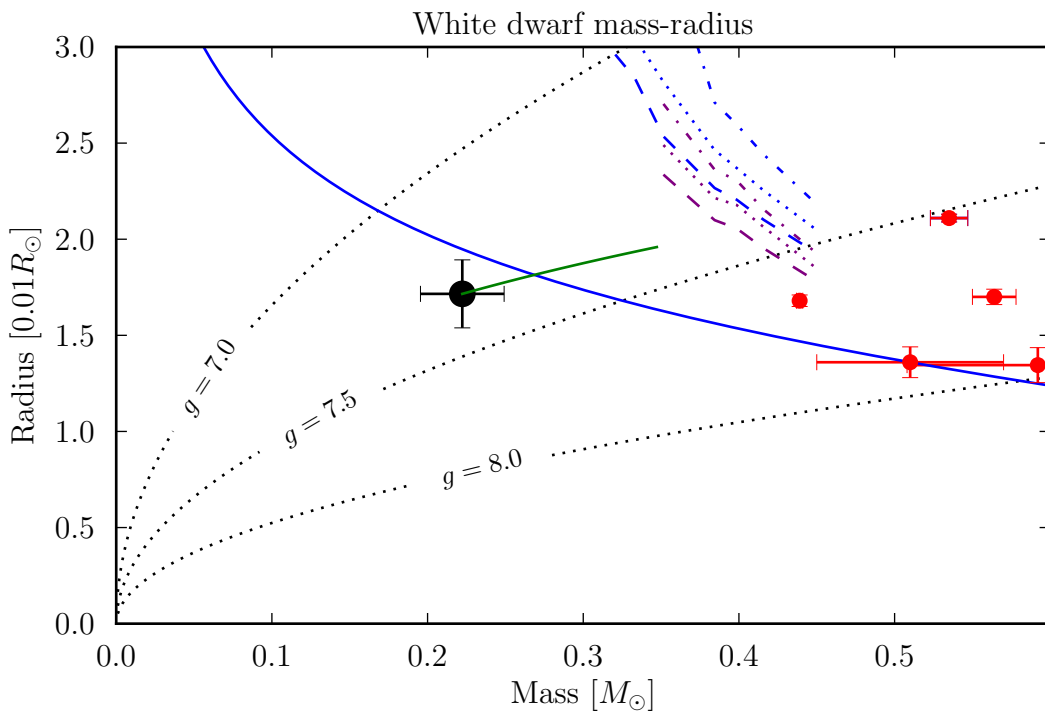


FIGURE 4.20: The mass and radius of the white dwarf in PTF1108ag. The dotted lines indicate the surface gravity, the blue line is the zero-temperature white dwarf mass radius relation from Eggleton, as quoted by Verbunt and Rappaport [68], the blue dashed-dotted lines are non-zero temperature Helium white dwarf models, purple dashed-dotted lines are CO white dwarf models, both from Panei et al. [44]. The red points are white dwarfs in other eclipsing binary stars, see [39, 45, 46, 62]

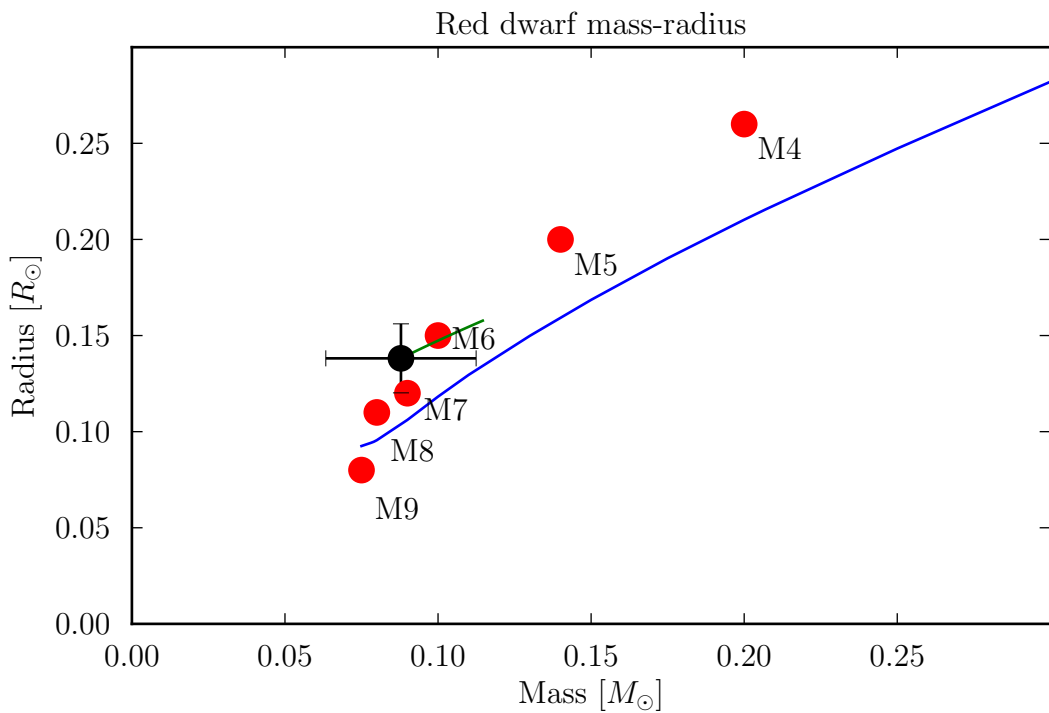


FIGURE 4.21: The mass and radius of the red dwarf in PTF1108ag. The green line indicates the systematic correction for the red dwarf radial velocity, the blue line is the theoretical model for 1Gyr old red dwarfs from Baraffe et al. [4].
The red points are taken from table 1.1

Chapter 5

Discussion and conclusion

5.1 Summary and conclusion

PTF1108ag is an eclipsing binary composed of a red dwarf and a white dwarf. Photometry shows deep, flat-bottom eclipses and a strong reflection component, but no secondary eclipse. Spectroscopy shows both the white dwarf, which is dominating the blue part of the spectrum and shows Balmer absorption lines, and the red dwarf, dominating in the red part of the spectrum and showing Balmer emission lines. These data sets are used to determine the system parameters of the binary star. A complication in the reduction of the data is a red dwarf about 1.5 arcseconds away (called ‘interloper’), and the data is corrected for this contamination.

The orbital period is determined using data from Ultracam with a high cadence with a baseline of 2 days, and with photometry from the Palomar transient factory which has an irregular cadence but a baseline of 4 years. The most accurate measurement is by PTF, with an orbital period of $P_{\text{orb}} = 0.10602724 \pm 1.3 \cdot 10^{-7}$ d.

The white dwarf spectrum shows only hydrogen absorption lines, and is thus a DA white dwarf. Fitting the spectrum with models gives a value of 26000 ± 4000 K for the temperature and surface gravity $\log(g) = 7.5 \pm 1$ for the white dwarf. The red dwarf spectral type is determined to be a $M4 \pm 1$ by fitting the spectra between phase 0.2 and 0.8. Spectra of the interloper show that this is a $M3 \pm 1$ red dwarf. The colors of the binary determined with the Ultracam photometry indicate a temperature of ~ 25000 K and a lower surface gravity, in agreement with the spectroscopic temperature. The red dwarf color shows a different result than the spectroscopy for both the red dwarf and interloper, $M0$ and $M3$ with an error of ~ 1 spectral type.

The absorption features from the white dwarf and the emission features from the red dwarf are used to determine the radial velocity of both stars. The measured velocities are 85 ± 15 km/s and 215 ± 6 km/s, giving a mass ratio $m_2/m_1 = q = 0.40 \pm 0.07$. The emission lines from the red dwarf are only visible between the

phases 0.2 and 0.8, and are a result of the irradiation, supported by the variations of the equivalent width with phase. This means that the measured radial velocity is a lower limit; it measures the center of light which moves slower than the center of mass. The amplitude of this effect is not determined, but estimates are in the order of 20%.

The Ultracam lightcurves are fitted with Lcurve to determine the radii of the stars and inclination of the system. The solutions space of the parameters show partial degeneracies, which dominate the errors. The lightcurve results in the g' give a best fit of $r1/a = 0.0273 \pm 0.0023$ and $r2/a = 0.280 \pm 0.026$ for the relative radii, with the other bands (u' , r' and i') showing similar values. The inclination for the system $i = 80.1 \pm 1.1$, and is also consistent between the different bands. The temperature, $T_2 = 3805 \pm 154\text{K}$ in g' , shows more scatter with in the u' a temperature 1200K higher, which is not within error bars. The mass ratio for the best fit is $q = 0.150 \pm 0.037$, and varied between 0.13 and 0.18 in the other filters. The reflection efficiency factor is consistently higher than 1, between ~ 1.3 and ~ 2.0 .

The results has a few problems: a discrepancy in the mass ratio and a problem with the reflection effect in lightcurve, see the next section for a discussion. Using the measured values to determine the mass and radius, the stars are compared to theory and other post-common-envelope binaries. The white dwarf has a low mass, between $0.22\text{--}0.33M_\odot$, compared to other PCEB white dwarfs, and making it an interesting object for further study. The red dwarf radius is larger than expected from the mass, but this is common in close binary stars. The spectral type expected for the mass and radius is $\sim M6$, which does not corresponds to the measurement from the spectra. This could be due to the irradiation effect heating the red dwarf.

Unfortunately the errors and systematic uncertainties are to high to draw any firm conclusion about the evolution of the system. If the mass and radius of the red dwarf are measured correctly, this system is not a hibernating cataclysmic variable in the period gap. Red dwarfs in the period gap have a mass of typically $0.2M_\odot$ and a radius $\sim 0.23 - 0.30R_\odot$, see figure 1.6. It is thus a red dwarf white dwarf binary which emerged from the common envelope phase as it is now. The time since this happened is determined using the white dwarf cooling age, which is about $\sim 25\text{Myr}$, see Panei et al. [44]. The core composition of the white dwarf has to be helium, *if* the mass is really as low as measured. This means that the precursor went through the common envelope phase as a red giant.

Using the crude distance measurements indicating a distance of about 800-1000 parsec and the galactic latitude of 39 degrees, putting it about 500 to 600 pc above the galactic plane. The distance to the interloper keeps the possibility open that it is physically close to the binary PTF1108ag.

5.2 Remaining problems and solutions

A problem in the analysis are uncertainties of the measured radial velocities. The white dwarf radial velocity has a significant measurement errors, which dominates the uncertainty on the mass. However despite the low statistical error on the red dwarf velocity, it is also uncertain as it suffers from a systematic error of unknown magnitude due to the reflection effect. Estimates for the correction indicate a velocity 20% higher, but the model, and thus the estimate, is very crude. Another cause of systematic error is that all features which are measured are a mix between absorption lines from the white dwarf and emission features from the red dwarf. It is possible that this can either increase or decrease the radial velocity measurements of the red dwarf or white dwarf.

Assuming the radial velocities are correct, the resulting mass ratio ($q = 0.40 \pm 0.07$) is inconsistent with the mass ratio determined from the lightcurves ($q = 0.150 \pm 0.037$). The correction for the reflection effect would lower the mass ratio from the radial velocities, but even than they are still inconsistent. This could be caused by systematic effect in the radial velocity measurements as described above, but it is also possible that the lightcurve model is incorrect. The q factor from the lightcurve is determined from the ellipsoidal variations, which are also influenced by the limb darkening and gravity darkening effects. The description used for these effects are determined for single stars, which the red dwarf clearly is not, as it is deformed and irradiated. However, the results without using any limb darkening and gravity darkening do not differ by a huge amount, indicating that this is only a minor effect.

Another problem with the lightcurve analysis is the irradiation effect which has an efficiency higher than 1. This indicates that the reflection effect is stronger than expected by just using the parametrization described in section 2.2. A related problem is the high temperature for the red dwarf in the lightcurve models, around 4000K. This would correspond to a spectral type of M0V, as was found by the color of the red dwarf, but not by the spectroscopy. This assuming a correlation between spectral type and temperature, which might be incorrect for strongly irradiated red dwarfs in binaries. It could be a result of an incorrect white dwarf temperature, and to compensate, reflection efficiency and the red dwarf temperature are incorrect. Another possibility is that the simple description of the reflection effect is not applicable, as it does not take into account any flow of energy to the backside of the star. A simple calculation using measured data and data from table 1.1, shows that the red dwarf receives a factor of ~ 2 more energy than it produces, which could have an impact on the temperature and structure.

An incorrect subtraction of the interloper flux could also cause a problem with the temperatures and reflection effect. Despite the best efforts, it is possible that the interloper contamination is wrong. This would result in a different overall flux, which would percentage wise have the largest effect during the primary eclipse, which determines the temperature ratio (see section 2.2). A hint of this can be seen in the u' results (see table 4.4), which could not be corrected for the interloper

contamination. The high red dwarf temperature is likely caused by a higher flux during the primary eclipse, which is a combination of the red dwarf and interloper.

These uncertainties can be solved by obtaining higher signal to noise and higher resolution spectra. This would really help in the analysis of the radial velocities for both components, since the higher resolution would help in distinguishing the two components. In addition, the temperature determination of the white dwarf could be improved, especially if more of the blue spectrum below ~ 4000 would be available. A higher signal to noise would also help in the red part of the spectrum, as the spectral type and variation of the emission features can help in determining the nature of the red dwarf and help to solve the temperature discrepancy of the red dwarf. Ideally one would want a spectrum taken during the eclipse, however the red dwarf has a magnitude of about 20, and the eclipse is only 2 minutes long, making this a challenge even with a large telescope.

Higher signal to noise spectra would also allow modeling of the equivalent width of the emission lines as function of phase which can be used to determine the irradiation correction of the red dwarf velocity. This was not attempted in this work since the signal to noise of the spectra was relatively low and a better phase coverage is needed. A more accurate value for the mass ratio can then be implemented in the lightcurve fitting, confining the solution space.

Another improvement would be to get a measurement of the secondary eclipse in the lightcurve, which would also lift one of the parameter degeneracies. To obtain a higher signal to noise measurement of the secondary eclipse multiple things can be done. One is looking a longer wavelength in which the red dwarf is brighter, and would thus give a higher signal to noise. Second is to use a larger telescope or multiple measurements of the eclipse. A third improvement would be to improve the photometry extraction, either by getting data with very good seeing and using point spread photometry, which was not possible with the Ultracam data.

If all these problems can be solved, the evolution of the system can be investigated further. A question which can already be partially answered is the age of the system since the common envelope phase. Using the temperature cooling models for a low mass white dwarf gives an age of about 25Myr, but depends on temperature and mass of the white dwarf. If the mass of both stars is known accurately, they can be used to model the evolution backwards, which would give the initial mass of both progenitors stars. An interesting question is the nature of the white dwarf, does it have a carbon-oxygen core or a helium core, which could be answered better if a more accurate mass and radius is known. Of course modeling the system forward in time is also possible, which can be used to determine the amount of angular momentum loss and determine when the red dwarf will overfill its Roche lobe.

Appendix A

ULTRACAM logs

The log files of the Hale observation run and the Ultracam run on the WHT.

TABLE A.1: Blue arm spectra

Filename	Object	Time [d utc]	Exposuretime [s]
b120130_0001.fits	bias	29 23:44:12.1	0
b120130_0002.fits	bias	29 23:44:33.4	0
b120130_0003.fits	bias	29 23:44:54.8	0
b120130_0004.fits	bias	29 23:45:16.2	0
b120130_0005.fits	bias	29 23:45:37.5	0
b120130_0006.fits	bias	29 23:45:58.9	0
b120130_0007.fits	bias	29 23:46:20.2	0
b120130_0008.fits	bias	29 23:46:41.6	0
b120130_0009.fits	bias	29 23:47:03.0	0
b120130_0010.fits	bias	29 23:47:24.3	0
b120130_0013.fits	FeAr	29 23:55:08.3	60
b120130_0014.fits	FeAr	29 23:56:29.6	60
b120130_0021.fits	G191B2B	30 02:08:20.7	30
b120130_0022.fits	G191B2B	30 02:09:12.0	30
b120130_0023.fits	G191B2B	30 02:10:59.8	30
b120130_0024.fits	G191B2B	30 02:11:51.1	30
b120130_0040.fits	PTFS1108ag	30 07:01:23.7	300
b120130_0041.fits	PTFS1108ag	30 07:06:45.1	300
b120130_0042.fits	PTFS1108ag	30 07:12:06.4	300
b120130_0043.fits	PTFS1108ag	30 07:17:27.8	300
b120130_0080.fits	internal flat	30 11:44:19.0	2
b120130_0081.fits	internal flat	30 11:46:34.3	2
b120130_0082.fits	internal flat	30 11:46:57.6	2
b120130_0083.fits	internal flat	30 11:47:21.0	2
b120130_0084.fits	internal flat	30 11:47:44.4	2
b120130_0085.fits	internal flat	30 11:48:07.7	2
b120130_0086.fits	internal flat	30 11:51:08.6	2
b120130_0087.fits	internal flat	30 11:51:32.0	2

Continued on next page

Table A.1 – Continued from previous page

Filename	Object	Time [d utc]	Exposuretime [s]
b120130_0088.fits	internal flat	30 11:51:55.3	2
b120130_0089.fits	internal flat	30 11:52:18.7	2
b120131_0056.fits	G191B2B	31 05:03:51.1	60
b120131_0057.fits	G191B2B	31 05:05:12.5	60
b120131_0062.fits	PTFS1108ag	31 05:36:22.0	300
b120131_0063.fits	PTFS1108ag	31 05:41:43.3	300
b120131_0064.fits	FeAr	31 05:47:32.8	60
b120131_0065.fits	FeAr	31 05:48:54.1	60
b120131_0066.fits	PTFS1108ag	31 05:52:23.3	300
b120131_0067.fits	PTFS1108ag	31 05:57:44.6	300
b120131_0068.fits	PTFS1108ag	31 06:03:06.0	300
b120131_0069.fits	PTFS1108ag	31 06:08:27.4	300
b120131_0070.fits	PTFS1108ag	31 06:13:48.7	300
b120131_0071.fits	PTFS1108ag	31 06:19:10.1	300
b120131_0072.fits	PTFS1108ag	31 06:24:31.4	300
b120131_0073.fits	PTFS1108ag	31 06:29:52.8	300
b120131_0074.fits	PTFS1108ag	31 06:35:14.1	300
b120131_0075.fits	PTFS1108ag	31 06:40:35.5	300
b120131_0076.fits	PTFS1108ag	31 06:45:56.9	300
b120131_0077.fits	FeAr	31 06:52:22.4	60
b120131_0078.fits	PTFS1108ag	31 07:06:55.6	300
b120131_0079.fits	PTFS1108ag	31 07:12:16.9	300
b120131_0080.fits	PTFS1108ag	31 07:17:38.3	300
b120131_0081.fits	FeAr	31 07:27:43.1	60
b120131_0082.fits	FeAr	31 07:29:04.5	60
b120131_0083.fits	PTFS1108ag	31 09:01:06.4	300
b120131_0084.fits	PTFS1108ag	31 09:06:27.8	300
b120131_0085.fits	PTFS1108ag	31 09:11:49.1	300
b120131_0086.fits	PTFS1108ag	31 09:17:10.5	300
b120131_0087.fits	PTFS1108ag	31 09:22:31.9	300
b120131_0088.fits	FeAr	31 09:29:08.0	60
b120131_0089.fits	FeAr	31 09:34:05.8	60
b120131_0090.fits	PTFS1108ag	31 09:37:59.2	300
b120131_0091.fits	PTFS1108ag	31 09:43:20.5	300
b120131_0092.fits	PTFS1108ag	31 09:48:41.9	300
b120131_0093.fits	PTFS1108ag	31 09:54:03.3	300
b120131_0094.fits	PTFS1108ag	31 09:59:24.6	300
b120131_0095.fits	PTFS1108ag	31 10:04:46.0	300
b120131_0096.fits	PTFS1108ag	31 10:10:07.3	300
b120131_0097.fits	PTFS1108ag	31 10:15:28.7	300
b120131_0098.fits	PTFS1108ag	31 10:20:50.0	300
b120131_0099.fits	PTFS1108ag	31 10:26:11.4	300
b120131_0100.fits	PTFS1108ag	31 10:31:32.7	300
b120131_0101.fits	PTFS1108ag	31 10:36:54.1	300

Continued on next page

Table A.1 – Continued from previous page

Filename	Object	Time [d utc]	Exposuretime [s]
b120131_0102.fits	FeAr	31 10:44:11.2	60
b120131_0103.fits	FeAr	31 10:45:32.5	60
b120201_0003.fits	G191B2B	1 02:11:50.5	60
b120201_0004.fits	G191B2B	1 02:13:11.9	60
b120201_0029.fits	FeAr	032 07:26:36.5	60
b120201_0030.fits	PTFS1108ag	1 07:29:54.9	300
b120201_0031.fits	PTFS1108ag	1 07:35:16.3	300
b120201_0032.fits	PTFS1108ag	1 07:40:37.7	300
b120201_0033.fits	PTFS1108ag	1 07:45:59.0	300
b120201_0034.fits	PTFS1108ag_comp	1 07:54:10.4	600
b120201_0035.fits	FeAr	1 08:06:49.5	60
b120201_0036.fits	FeAr	1 08:08:10.9	60

TABLE A.2: Red arm spectra

Filename	Object	Time [d utc]	Exposuretime [s]
r120130_0001.fits	bias	29 23:44:12.9	0
r120130_0002.fits	bias	29 23:44:36.1	0
r120130_0003.fits	bias	29 23:44:59.2	0
r120130_0004.fits	bias	29 23:45:22.4	0
r120130_0005.fits	bias	29 23:45:45.5	0
r120130_0006.fits	bias	29 23:46:08.6	0
r120130_0007.fits	bias	29 23:46:31.8	0
r120130_0008.fits	bias	29 23:46:54.9	0
r120130_0009.fits	bias	29 23:47:18.1	0
r120130_0010.fits	bias	29 23:47:41.2	0
r120130_0013.fits	HeNeAr	30 00:14:51.5	0.4
r120130_0014.fits	HeNeAr	30 00:15:15.0	0.4
r120130_0021.fits	G191B2B	30 02:08:23.9	30
r120130_0022.fits	G191B2B	30 02:09:17.1	30
r120130_0023.fits	G191B2B	30 02:11:02.5	30
r120130_0024.fits	G191B2B	30 02:11:55.6	30
r120130_0080.fits	internal flat	30 11:45:12.6	1
r120130_0081.fits	internal flat	30 11:46:22.2	1
r120130_0082.fits	internal flat	30 11:46:46.4	1
r120130_0083.fits	internal flat	30 11:47:10.5	1
r120130_0084.fits	internal flat	30 11:47:34.6	1
r120130_0085.fits	internal flat	30 11:47:58.8	1
r120130_0086.fits	internal flat	30 11:51:12.2	1
r120130_0087.fits	internal flat	30 11:51:36.3	1
r120130_0088.fits	internal flat	30 11:52:00.5	1
r120130_0089.fits	internal flat	30 11:52:24.6	1
r120131_0058.fits	G191B2B	31 05:03:51.5	60
r120131_0059.fits	G191B2B	31 05:05:14.6	60
r120131_0064.fits	PTFS1108ag	31 05:36:22.5	300
r120131_0065.fits	PTFS1108ag	31 05:41:45.6	300
r120131_0066.fits	HeNeAr	31 05:50:08.8	0.4
r120131_0067.fits	HeNeAr	31 05:50:32.4	0.4
r120131_0068.fits	PTFS1108ag	31 05:52:24.1	300
r120131_0069.fits	PTFS1108ag	31 05:57:47.2	300
r120131_0070.fits	PTFS1108ag	31 06:03:10.4	300
r120131_0071.fits	PTFS1108ag	31 06:08:33.5	300
r120131_0072.fits	PTFS1108ag	31 06:13:56.6	300
r120131_0073.fits	PTFS1108ag	31 06:19:19.8	300
r120131_0074.fits	PTFS1108ag	31 06:24:42.9	300
r120131_0075.fits	PTFS1108ag	31 06:30:06.0	300
r120131_0076.fits	PTFS1108ag	31 06:35:29.2	300
r120131_0077.fits	PTFS1108ag	31 06:40:52.3	300
r120131_0078.fits	PTFS1108ag	31 06:46:15.4	300
r120131_0080.fits	PTFS1108ag	31 07:07:08.4	300

Continued on next page

Table A.2 – Continued from previous page

Filename	Object	Time [d utc]	Exposuretime [s]
r120131_0081.fits	PTFS1108ag	31 07:12:31.6	300
r120131_0082.fits	PTFS1108ag	31 07:17:54.7	300
r120131_0085.fits	PTFS1108ag	31 09:01:17.5	300
r120131_0086.fits	PTFS1108ag	31 09:06:40.7	300
r120131_0087.fits	PTFS1108ag	31 09:12:03.8	300
r120131_0088.fits	PTFS1108ag	31 09:17:26.9	300
r120131_0089.fits	PTFS1108ag	31 09:22:50.1	300
r120131_0090.fits	HeNeAr	31 09:30:37.5	0.4
r120131_0091.fits	HeNeAr	31 09:35:18.5	0.4
r120131_0092.fits	PTFS1108ag	31 09:37:59.6	300
r120131_0093.fits	PTFS1108ag	31 09:43:22.7	300
r120131_0094.fits	PTFS1108ag	31 09:48:45.9	300
r120131_0095.fits	PTFS1108ag	31 09:54:09.0	300
r120131_0096.fits	PTFS1108ag	31 09:59:32.1	300
r120131_0097.fits	PTFS1108ag	31 10:04:55.3	300
r120131_0098.fits	PTFS1108ag	31 10:10:18.4	300
r120131_0099.fits	PTFS1108ag	31 10:15:41.5	300
r120131_0100.fits	PTFS1108ag	31 10:21:04.7	300
r120131_0101.fits	PTFS1108ag	31 10:26:27.8	300
r120131_0102.fits	PTFS1108ag	31 10:31:51.0	300
r120131_0103.fits	PTFS1108ag	31 10:37:14.1	300
r120131_0079.fits	HeNeAr	31 06:53:34.5	0.4
r120131_0083.fits	HeNeAr	31 07:30:39.0	0.4
r120131_0084.fits	HeNeAr	31 07:31:02.5	0.4
r120131_0104.fits	HeNeAr	31 10:43:06.3	0.4
r120131_0105.fits	HeNeAr	31 10:43:29.9	0.4
r120201_0003.fits	G191B2B	1 02:11:51.2	60
r120201_0004.fits	G191B2B	1 02:13:14.4	60
r120201_0034.fits	HeNeAr	1 07:28:24.2	0.4
r120201_0035.fits	PTFS1108ag	1 07:29:53.1	300
r120201_0036.fits	PTFS1108ag	1 07:35:16.3	300
r120201_0037.fits	PTFS1108ag	1 07:40:39.4	300
r120201_0038.fits	PTFS1108ag	1 07:46:02.6	300
r120201_0041.fits	PTFS1108ag_comp	1 07:57:32.5	400
r120201_0042.fits	HeNeAr	1 08:09:42.0	0.4
r120201_0043.fits	HeNeAr	1 08:10:05.5	0.4

TABLE A.3: ULTRACAM log of 30-01-2012

file	object	date	utc start	utc end	num	flag	mode	exp	cycle	filter	nblue	
run001	POWON											
run002	Bias	30/01/2012	16:34:40	16:35:38	11	bias	FFCLR	.5	5807.6	u' g' r'	1	
run003	Bias	30/01/2012	16:38:09	16:38:56	9	bias	FFCLR	.5	5807.6	u' g' r'	1	
run004	Bias	30/01/2012	16:40:34	16:41:20	9	bias	FFCLR	.5	5807.6	u' g' r'	1	
run005	Bias	30/01/2012	16:42:51	16:43:26	7	bias	FFCLR	.5	5807.5	u' g' r'	1	
run006	Bias	30/01/2012	16:44:57	16:45:43	9	bias	FFCLR	.5	5807.6	u' g' r'	1	
run007	Bias	30/01/2012	16:47:01	16:51:52	51	bias	FFCLR	.5	5807.6	u' g' r'	1	
run008	Bias	30/01/2012	16:51:59	16:54:29	51	bias	FFCLR	.5	2986.5	u' g' r'	1	
run009	Bias	30/01/2012	16:54:36	16:55:58	51	bias	FFCLR	.5	1639.0	u' g' r'	1	
run010	Bias	30/01/2012	16:57:24	16:57:35	51	bias	2-WIN	.5	224.6	u' g' r'	1	
run011	Bias	30/01/2012	16:57:41	16:58:00	51	bias	2-WIN	.5	385.8	u' g' r'	1	
run012	Bias	30/01/2012	16:58:56	16:59:22	101	bias	2-WIN	.5	262.5	u' g' r'	1	
run013	Bias	30/01/2012	17:00:30	17:01:34	19	bias	4-WIN	.5	3544.5	u' g' r'	2	
run014	Bias	30/01/2012	17:02:01	17:04:58	51	bias	4-WIN	.5	3544.5	u' g' r'	1	
run015	Bias	30/01/2012	17:05:09	17:07:11	51	bias	4-WIN	.5	2447.6	u' g' r'	1	
run016	Bias	30/01/2012	17:07:18	17:09:21	51	bias	4-WIN	.5	2452.7	u' g' r'	1	
run017	SDSS J065133.33+284423.3	30/01/2012	22:00:11	22:02:26	67	data caution	FFNOC	500.5	2045.2	u' g' r'	4	
run018	SDSS J065133.33+284423.3	30/01/2012	22:02:32	23:23:45	2343	data	2-WIN		2080.6	u' g' r'	4	
run019	SDSS J065133.33+284423.3	30/01/2012	23:29:46	23:30:13	15	data	2-WIN		1800.5	1959.4	u' g' r'	4
run020	SDSS J065133.33+284423.3	30/01/2012	23:33:12	01:16:30	2979	data	2-WIN		1800.5	2081.2	u' g' r'	4
run021	SDSS J085713.26+331843.0	31/01/2012	01:21:07	01:27:31	77	data caution	FFNOC	3500.5	5047.4	u' g' r'	4	
run022	SDSS J085713.26+331843.0	31/01/2012	01:27:36	06:54:33	6427	data	FFNOC	1500.5	3052.7	u' g' r'	3	
run023	Feige 66	31/01/2012	06:57:09	06:58:37	11	data caution	FFCLR	3000.5	8777.1	u' g' r'	2	
run024	Feige 66	31/01/2012	06:58:45	06:59:42	10	data caution	FFCLR	500.5	6252.1	u' g' r'	2	
run025	Feige 66	31/01/2012	06:59:52	07:01:40	19	data	FFCLR	250.5	6043.7	u' g' r'	1	
run026	Feige 66	31/01/2012	07:01:49	07:03:24	17	data	FFCLR	150.5	5948.3	u' g' r'	1	
run027	Flat	31/01/2012	07:07:15	07:08:54	18	flat	FFCLR	.5	5807.7	u' g' r'	1	
run028	Bias	31/01/2012	07:10:11	07:10:39	101	bias	2-WIN	.5	281.4	u' g' r'	1	
run029	Bias	31/01/2012	07:10:54	07:13:34	101	bias	FFCLR	.5	1601.4	u' g' r'	1	
run030	Flat	31/01/2012	07:15:02	07:38:21	244	flat	FFNOC	.5	5758.9	u' g' r'	1	

TABLE A.4: ULTRACAM log of 31-01-2012

file	object	date	utc start	utc end	num	flag	mode	exp	cycle	filter	nblue
run001	POWON	31/01/2012	16:16:44	16:18:11	16	bias	FFCLR	.5	5807.6	u' g' r'	1
run002	Bias	31/01/2012	16:21:04	16:21:39	7	bias	FFCLR	.5	5807.5	u' g' r'	1
run003	Bias	31/01/2012	16:22:45	16:23:20	7	bias	FFCLR	.5	5807.5	u' g' r'	1
run004	Bias	31/01/2012	16:23:32	16:24:07	7	bias	FFCLR	.5	5807.6	u' g' r'	1
run005	Bias	31/01/2012	16:25:27	16:35:08	101	bias	FFCLR	.5	5807.6	u' g' r'	1
run006	Bias	31/01/2012	16:35:32	16:36:04	12	bias	FFCLR	.5	2986.4	u' g' r'	1
run007	Bias	31/01/2012	16:36:39	16:41:38	101	bias	FFCLR	.5	2986.5	u' g' r'	1
run008	Bias	31/01/2012	16:42:03	16:44:47	101	bias	FFCLR	.5	1639.0	u' g' r'	1
run009	Bias	31/01/2012	19:11:20	19:30:32	201	flat	FFNOC	.5	5758.9	u' g' r'	1
run010	Flat	31/01/2012	19:31:57	19:32:51	8	data caution	FFCLR	2000.5	7799.2	u' g' r'	1
run011	Feige 22	31/01/2012	19:33:01	19:35:35	21	data	FFCLR	2000.5	7707.7	u' g' r'	1
run012	Feige 22	31/01/2012	19:35:44	19:37:33	17	data	FFCLR	1000.5	6805.0	u' g' r'	1
run013	Feige 22	31/01/2012	19:40:29	19:42:44	66	data caution	2-WIN	1800.5	2077.4	u' g' r'	4
run014	SDSS J065133.33+284423.3	31/01/2012	19:42:48	19:48:27	164	data	2-WIN	1800.5	2078.4	u' g' r'	4
run015	SDSS J065133.33+284423.3	31/01/2012	19:48:30	23:20:02	6099	data	2-WIN	1800.5	2081.2	u' g' r'	4
run016	SDSS J065133.33+284423.3	31/01/2012	23:27:06	00:50:21	2401	data	FFNOC	500.5	2048.9	u' g' i'	4
run017	SDSS J065133.33+284423.3	01/02/2012	01:53:35	01:57:55	128	data caution	FFNOC	500.5	2052.7	u' g' i'	4
run018	SDSS J085713.26+331843.0	01/02/2012	01:57:58	07:10:57	9149	data	FFCLR	3000.5	8437.6	u' g' i'	1
run019	SDSS J085713.26+331843.0	01/02/2012	07:13:25	07:14:07	6	data caution	FFCLR	500.5	6252.1	u' g' i'	1
run020	Feige 66	01/02/2012	07:14:16	07:15:13	10	data caution	FFCLR	500.5	6283.8	u' g' i'	2
run021	Feige 66	01/02/2012	07:15:22	07:17:34	22	data	FFCLR	500.5	5758.9	u' g' i'	1
run022	Feige 66	01/02/2012	07:39:23	216	flat	FFNOC	.5	5758.9	u' g' i'	1	
run023	Flat										

Appendix B

Lcurve

This appendix shows a parameter list for the Lcurve lightcurves, copied from the manual.

TABLE B.1: Binary and star parameters

q	Mass ratio, $q = M_2/M_1$
iangle	Inclination angle, degrees
r1	Radius of star 1, scaled by the binary separation
r2	Radius of star 2, scaled by the binary separation. The radius is measured along the line of centres towards star 1.
cphi3	Third contact phase (star 1 starting to emerge from eclipse). This is an alternative way to specify the radii, based on a spherical approximation for the two stars, i.e. unless the stars are spherical, it is not quite the true third contact. The radii will be computed from the contact phases according to the two equations $r2 + r1 = \sqrt{(1 - \sin^2 i \cos^2(2 * \pi * cphi4))}$ and $r2 - r1 = \sqrt{(1 - \sin^2 i \cos^2(2 * \pi * cphi3))}$. The radii returned are precise, just the interpretation as contact phases that is not precise. cphi3 and cphi4 need the boolean use_radii set to 0 to enabled. The reason for using them is to help with MCMC iterations as they prevent the nasty curved correlation between r1, r2 and i. This can save a huge amount of CPU time.
cphi4	Fourth contact phase, star 1 fully emerged from eclipse. See cphi3 for details.
spin1	This is the ratio of the spin frequency of star 1 to the orbital frequency. In this case a modified form of the Roche potential is used for star 1
spin2	This is the ratio of the spin frequency of star 2 to the orbital frequency. In this case a modified form of the Roche potential is used for star 2

t1	Temperature of star 1, Kelvin. This is really a substitute for surface brightness which is set assuming a black-body given this parameter. If it was not for irradiation that would be exactly what this is, a one-to-one replacement for surface brightness. Irradiation however introduces bolometric luminosities effectively and breaks the direct link. Some would then argue that one must use model atmospheres except at the moment irradiated model atmosphere are in their infancy.
t2	Temperature of star 2, Kelvin. Set $\neq 0$ in order that it does not get scaled when using the iscale parameter.
ldc1_1, etc	Limb darkening for stars is quite hard to specify precisely. Here we adopt a 4 coefficient approach which can either represent a straightforward polynomial expansion of the form $I(mu) = 1 - \sum_i a_i(1 - mu)^i$, or rather better in some cases Claret's 4-coefficient formula $I(mu) = 1 - \sum_i a_i(1 - mu^{(i/2)})$ ($i=1$ to 4). You specify these by supplying the 4 coefficients for each star (which for form's sake are potentially variable but you would probably be unwise to let them be free) and later on a parameter to say whether it is the polynomial or Claret's representation. The polynomial allows one to use linear and quadratic limb darkening amongst others by setting the upper coefficients = 0. ldc1_1 is the first coefficient of star 1, ldc1_2 is the second, etc, while ldc2_1 is the first coefficient for star 2 etc. See limb1, limb2, mucrit1, mucrit2 below.
velocity_scale	Velocity scale, sum of unprojected orbital speeds, used for accounting for Doppler beaming and gravitational lensing. On its own this makes little difference to the light curve, so you should not usually let it be free, but you might want to if you have independent K1 or K2 information which you can apply as part of a prior.
beaming_factor1	The factor to use for Doppler beaming from star 1. This corresponds to the factor (3-alpha) that multiplies $-v_r/c$ in the standard beaming formula where alpha is related to the spectral shape. Use of this parameter requires the velocity_scale to be set.
beaming_factor1	The factor to use for Doppler beaming from star 2. This corresponds to the factor (3-alpha) that multiplies $-v_r/c$ in the standard beaming formula where alpha is related to the spectral shape. Use of this parameter requires the velocity_scale to be set.

TABLE B.2: Lcurve: General parameters

t0	Zero point of ephemeris, marking time of mid-eclipse (or in general superior conjunction) of star 1
period	Orbital period, same units as time.
deltat	Time shift between the primary and secondary eclipses to allow for small eccentricities and Roemer delays in the orbit. The sign is defined such that deltat $\gtrless 0$ implies that the secondary eclipse suffers a delay compared to the primary compared to precisely 0.5 difference. deltat $\nmid 0$ implies the secondary eclipse comes a little earlier than expected. Assuming that the "primary eclipse" is the eclipse of star 1, then, using the same sign convention, the Roemer delay is given by $= P*(K1-K2)/(Pi*c)$ where P is the orbital period, K1 and K2 are the usual projected radial velocity semi-amplitudes $Pi = 3.14159..$, and c = speed of light. See Kaplan (2010) for more details. The delay is implemented by adjusting the orbital phase according to $\phi' = \phi + (deltat/2/P)*(cos(2*Pi*\phi)-1)$, i.e. there is no change at primary eclipse but a delay of $-deltat/P$ by the secondary eclipse.
gravity_dark	Gravity darkening coefficient. Only matters for the Roche distorted case, but is prompted for always. There are two alternatives for this. In the standard old method, the temperatures on the stars are set equal to $t2*(g/gr)**gdark$ where g is the gravity at a given point and gr is the gravity at the point furthest from the primary (the 'backside' of the secondary). For a convective atmosphere, 0.08 is the usual value while 0.25 is the number for a radiative atmosphere. This is translated into intensity using a blackbody approx. If you want to bypass the BB approx and invoke a direct relation flux $(g/gr)**gdark$ relation you should set gdark_bolom (see below) to 0 (false.)
absorb	The fraction of the irradiating flux from star 1 absorbed by star 2
slope, quad, cube	Fudge factors to help cope with any trends in the data as a result of e.g. airmass effects. The fit is multiplied by $(1+x*(slope+x*(quad+x*cube)))$ where x is the time scaled so that it varies from -1 to 1 from start to end of the data. One should expect these numbers to have absolute value ≤ 1 .

TABLE B.3: Lcurve: Disc parameters

rdisc1	Inner radius of azimuthally symmetric disc. Set = -1 to set it equal to r1 (it should not be allowed to vary in this case)
rdisc2	Outer radius of azimuthally symmetric disc
height_disc	Half height of disc at radius = 1. The height varies as a power law of radius
beta_disc	Exponent of power law in radius of disc. Should be $\zeta = 1$ to make concave disc; convex will not eclipse properly.
temp_disc	Temperature of outer part of disc. This is little more than a flux normalisation parameter but it is easier to think in terms of temperature
texp_disc	Exponent of surface brightness (NB: not temperature) over disc
lin_limb_disc	Linear limb darkening coefficient of the disc
quad_limb_disc	Quadratic limb darkening coefficient of the disc

TABLE B.4: Lcurve: Bright spot

radius_spot	Radius from accretor of bright-spot (units of binary separation).
length_spot	Length scale of spot (units of binary separation).
height_spot	Height of spot (units of binary separation). This is only a normalisation constant.
expon_spot	Spot is modeled as $x^{**n} * \exp(-x/l)$. This parameter specifies the exponent 'n'
angle_spot	This is the angle made by the line of elements of the spot measured in the direction of binary motion relative to the rim of the disc so that the "standard" value should be 0.
yaw_spot	Allows the spot elements effectively to beam their light away from the perpendicular to the line of elements. Measured as an angle in the same sense as angle_spot. 0 means standard perpendicular beaming.
temp_spot	Normalises the surface brightness of the spot.
tilt_spot	Allows spot to be other than perpendicular to the disc. 90 = perpendicular. If less than 90 then the spot is visible for more than half a cycle.
cfrac_spot	The fraction of the spot taken to be equally visible at all phases, i.e. pointing upwards.
beta_disc	Exponent of power law in radius of disc. Should be $\zeta = 1$ to make concave disc; convex will not eclipse properly.
temp_disc	Temperature of outer part of disc. This is no more than a flux normalisation parameter but it's easier to think in terms of temperature
texp_disc	Exponent of surface brightness over disc

lin_limb_disc	Linear limb darkening coefficient of the disc
quad_limb_disc	Quadratic limb darkening coefficient of the disc

TABLE B.5: Lcurve: Computational parameters

delta_phase	Accuracy in phase of eclipse computations. This determines the accuracy of any Roche computations. Example: 1.e-7
nlat1f	The number of latitudes for star 1's fine grid. This is used around the phase of primary eclipse (i.e. the eclipse of star 1)
nlat1c	The number of latitudes for star 1's coarse grid. This is used away from primary eclipse.
nlat2f	The number of latitudes for star 2's fine grid. This is used around the phase of secondary eclipse.
nlat2c	The number of latitudes for star 2's coarse grid. This is used away from secondary eclipse.
npole	True to set North pole of grid to the genuine stellar NP rather than substellar points. This is probably a good idea when modelling well detached binaries, especially with extreme radius ratios because then it allows one to concentrate points over a band of latitudes using the next two parameters
nlatfill	Extra number of points to insert per normal latitude strip along the path of star 1 as it transits star 2. This is designed to help tough extreme radius ratio cases. Take care to look at the resulting grid with visualise as the exact latitude range chosen is a little approximate. This is only enabled if npole since only then do the latitude strips more-or-less line up with the movement of the star.
nlngfill	Extra number of points to insert per normal longitude strip along the path of star 1 as it transits star 2. This is designed to help tough extreme radius ratio cases. Take care to look at the resulting grid with visualise as the exact latitude range chosen is a little approximate.
lfudge	The fine-grid latitude strip is computed assuming both stars are spherical. To allow for departures from this, this parameter allows one to increase the latitude limits both up and down by an amount specified in degrees. Use the program visualise.html to judge how large this should be. However, one typically would like to avoid lfudge > 30*r1/r2 as that could more than double the width of the strip.

phase1	this defines when star 1's fine grid is used abs(phase) \geq phase1. Thus phase1 = 0.05 will restrict the fine grid use to phase 0.95 to 0.05.
llo, lhi	These are experimental. They allow the user to fix the latitude limits of the fine strip which might be useful in preventing chi **2 variations caused by variable grids. The values need to reflect the likely range of inclinations and can only really be set by trial and error using visualise. They are in degrees following the usual convention for latitude on Earth. Set llo high and lhi low to stop them having any effect.
phase1	this defines when star 1's fine grid is used abs(phase) \geq phase1. Thus phase1 = 0.05 will restrict the fine grid use to phase 0.95 to 0.05.
phase2	this defines when star 2's fine grid is used phase2 until 1-phase2. Thus phase2 = 0.45 will restrict the fine grid use to phase 0.55 to 0.55.
nrad	The number of radial strips over the disc
wavelength	Wavelength (nm)
roche1	Account for Roche distortion of star 1 or not
roche2	Account for Roche distortion of star 2 or not
eclipse1	Account for the eclipse of star 1 or not
eclipse2	Account for the eclipse of star 2 or not
glens1	Account for gravitational lensing by star 1. If you use this roche1 must be = 0 and the velocity_scale
use_radii	If set = 1, the parameters r1 and r2 will be used to set the radii directly. If not, the third and fourth contact phases, cphi3 and cphi4, will be used instead (see description for cphi3 for details).
tperiod	The true orbital period in days. This is required, along with velocity_scale, if gravitational lensing is being applied to calculate proper dimensions in the system.
gdark_bolom	True if the gravity darkening coefficient represents the bolometric value where T is proportional to gravity to the power set by the coefficient. This is translated to flux variations using the black-body approximation. If False, it represents a filter-integrated value 'y' coefficient such that the flux depends upon the gravity to the power 'y'. This is itself an approximation and ideally should be replaced by a proper function of gravity, but is probably good enough for most purposes. Please see gravity_dark.

mucrit1	Critical value of mu on star 1 below which intensity is assumed to be zero. This is to allow one to represent Claret and Hauschildt's (2004) results where $I(\mu)$ drops steeply for $\mu \downarrow 0.08$ or so. WARNING: this option is dangerous. I would normally advise setting it = 0 unless you really know what you are doing as it leads to discontinuities.
mucrit2	Critical value of mu on star 2 below which intensity is assumed to be zero. See comments on mucrit1 for more.
limb1	String, either 'Poly' or 'Claret' determining the type of limb darkening law. See comments on ldc1_1 above.
limb2	String, either 'Poly' or 'Claret' determining the type of limb darkening law. See comments on ldc1_1 above.
mirror	Add any light not reprocessed in as if star reflected it or not as a crude approximation to the effect of gray scattering
add_disc	Add a disc or not
opaque	Make disc opaque or not
iscale	Individually scale the separate components or not. If set the each component, star 1, star 2, disc and bright spot will be individually scaled to minimise χ^{**2} . Otherwise a single overall factor will be computed. NB If you set this parameter then all temperature parameters (white dwarf, secondary, disc and bright spot) must be held fixed otherwise near-total degeneracy will result. The only reason it is not total is because of reflection effect from irradiation of the secondary by the white dwarf, but this is often very feeble and will not help, so, you have been warned. Scaling should in general lead to faster convergence than not scaling. You may have some cases where you do not want to include any secondary star component. You can do this by setting $t2 < 0$.

List of Figures

1.1	Hertzsprung-Russel Diagram	3
1.2	White Dwarf mass-radius relation	5
1.3	Red Dwarf mass-radius relation	7
1.4	Roche potential	9
1.5	Critical orbital period	10
1.6	Radius of CV donors	12
2.1	Lightcurve	16
2.2	Example eclipse	17
2.3	Example eclipse	18
2.4	NN Serpentis	20
2.5	KDP 1946+4340	21
3.1	PTF data	24
3.2	Ultracam readout modes	25
3.3	The comparison stars	26
3.4	Aperture photometry	27
3.5	PTF1108ag close-up	28
3.6	Energy per counts	31
3.7	Lightcurves	32
3.8	Example spectrum	34
3.9	Average PTF1108ag spectrum	35
4.1	PDM results	38
4.2	Orbital Period	39
4.3	Folded PTF data	39
4.4	White dwarf colors	41
4.5	Colors	42
4.6	WD Temperature and surface gravity	42
4.7	Distance with the white dwarf	43
4.8	White dwarf spectrum and best fit	44
4.9	WD vs RD temperature	45
4.10	Red dwarf spectra	46
4.11	Radial velocity with MOLLY	47
4.12	Radial velocity with IRAF	48
4.13	Radial velocity with MOLLY	49

4.14 Radial velocity, WD subtracted	51
4.15 Model radial velocity	52
4.16 Equivalent width	53
4.17 Lcurve example	55
4.18 Ultracam lightcurves	56
4.19 Mass vs irradiation correction	57
4.20 White dwarf mass-radius	58
4.21 Red dwarf mass-radius	59

List of Tables

1.1	Red dwarf parameters	6
3.1	Interloper contamination	29
3.2	Feige66 measurements	30
3.3	SDSS position and magnitudes	30
4.1	Flux	40
4.2	Radial velocity	50
4.3	Darkening parameters	54
4.4	Lightcurve results	54
A.1	Blue arm spectra	65
A.2	Red arm spectra	67
A.3	ULTRACAM log of 30-01-2012	69
A.4	ULTRACAM log of 31-01-2012	70
B.1	Binary and star parameters	71
B.2	Lcurve: General parameters	72
B.3	Lcurve: Disc parameters	73
B.4	Lcurve: Bright spot	73
B.5	Lcurve: Computational parameters	74

Abbreviations

CCD	Charge Coupled Device
Dec	Declination
MS	Main Sequence
PCEB	Post Common Envelope Binary
PTF	Palomar Transient Factory
RA	Right Ascension
RD	Red Dwarf
SDSS	Sloan Digitized Sky Survey
WD	White Dwarf
WHT	William Herschell Telescope

Physical Constants

Speed of light	$c = 2.997\ 924\ 58 \times 10^8$ ms (exact)
Gravitational const.	$G = 6.672\ 59 \times 10^{-11}$ $\text{m}^3\text{kg}^{-1}\text{s}^{-2}$
Stefan-Boltzmann const.	$\sigma = 5.670\ 51 \times 10^{-8}$ $\text{Jm}^{-2}\text{s}^{-1}\text{K}^{-4}$
Solar mass	$M_{\odot} = 1.989\ 1 \times 10^{30}$ kg
Solar radius	$R_{\odot} = 6.959\ 8 \times 10^8$ m
Solar luminosity	$L_{\odot} = 3.851\ 5 \times 10^{26}$ Js $^{-1}$
Parsec	$pc = 3.086 \times 10^{16}$ m
Angstrom	$\text{\AA} = 10^{-10}$ m

Bibliography

- [1] Palomar 200-inch telescope: Double spectrograph specs, Mar. 2011.
URL http://www.astro.caltech.edu/palomar/200inch/dbl_spec/dbl_spec.html.
- [2] H. A. Abt. Normal and abnormal binary frequencies. *ARA&A*, 21:343–372, 1983. doi: 10.1146/annurev.aa.21.090183.002015.
- [3] I. Baraffe and G. Chabrier. Mass–Spectral Class Relationship for M Dwarfs. *ApJ*, 461:L51, Apr. 1996. doi: 10.1086/309988.
- [4] I. Baraffe, G. Chabrier, F. Allard, and P. Hauschildt. Evolutionary models for solar metallicity low - mass stars: Mass - magnitude relationships and color - magnitude diagrams. *Astron.Astrophys.*, 337:403–412, 1998.
- [5] S. M. Beard, A. J. A. Vick, D. Atkinson, V. S. Dhillon, T. Marsh, S. McLay, M. Stevenson, and C. Tierney. Ultracam camera control and data acquisition system. In H. Lewis, editor, *Society of Photo-Optical Instrumentation Engineers (SPIE) Conference Series*, volume 4848 of *Society of Photo-Optical Instrumentation Engineers (SPIE) Conference Series*, pages 218–229, Dec. 2002. doi: 10.1117/12.461354.
- [6] P. Bergeron, G. Fontaine, T. P., and P. Kowalski. Synthetic colors and evolutionary sequences of hydrogen- and helium-atmosphere white dwarfs, Oct. 2011. URL <http://www.astro.umontreal.ca/~bergeron/CoolingModels>.
- [7] S. Bloemen, T. R. Marsh, R. H. Ø stensen, S. Charpinet, G. Fontaine, et al. Kepler observations of the beaming binary KPD 1946+4340. 2010.

- [8] J. J. Bochanski, A. A. West, S. L. Hawley, and K. R. Covey. Low-Mass Dwarf Template Spectra from the Sloan Digital Sky Survey. *Astron.J.*, 133:531–544, 2007. doi: 10.1086/510240.
- [9] J. Budaj. The Reflection Effect in Interacting Binaries or in Planet-Star Systems. *aj*, 141:59, Feb. 2011. doi: 10.1088/0004-6256/141/2/59.
- [10] G. Chabrier and I. Baraffe. Theory of low-mass stars and substellar objects. *Ann.Rev.Astron.Astrophys.*, 38:337–377, 2000. doi: 10.1146/annurev.astro.38.1.337.
- [11] G. Chabrier, I. Baraffe, F. Allard, and P. Hauschildt. Evolutionary models for very-low-mass stars and brown dwarfs with dusty atmospheres. *Astrophys.J.*, 542:464–472, 2000. doi: 10.1086/309513.
- [12] G. Chabrier, J. Gallardo, and I. Baraffe. Evolution of low-mass star and brown dwarf eclipsing binaries. *A&A*, 472:L17–L20, Sept. 2007. doi: 10.1051/0004-6361:20077702.
- [13] A. Claret and S. Bloemen. Gravity and limb-darkening coefficients for the Kepler, CoRoT, Spitzer uvby, UBVRIJHK, and Sloan photometric systems. *A&A*, 529, 2011.
- [14] C. M. Copperwheat, T. R. Marsh, V. S. Dhillon, S. P. Littlefair, R. Hickman, et al. Physical properties of IP Pegasi: an eclipsing dwarf nova with an unusually cool white dwarf. 2009.
- [15] V. S. Dhillon, T. R. Marsh, M. J. Stevenson, D. C. Atkinson, P. Kerry, et al. ULTRACAM: an ultra-fast, triple-beam CCD camera for high-speed astrophysics. *Mon.Not.Roy.Astron.Soc.*, 378:825–840, 2007. doi: 10.1111/j.1365-2966.2007.11881.x.
- [16] J. Eastman, R. Siverd, and B. S. Gaudi. Achieving better than one-minute accuracy in the Heliocentric and Barycentric Julian Dates. *Publ.Astron.Soc.Pac.*, 122:935–946, 2010. doi: 10.1086/655938.

- [17] B. Efron. Bootstrap methods: Another look at the jackknife. *The Annals of Statistics*, 7(1):pp. 1–26, 1979. ISSN 00905364. URL <http://www.jstor.org/stable/2958830>.
- [18] P. P. Eggleton. Approximations to the radii of Roche lobes. *ApJ*, 268:368, May 1983. doi: 10.1086/160960.
- [19] J. M. Fernandez, D. W. Latham, G. Torres, M. E. Everett, G. Mandushev, D. Charbonneau, F. T. O’Donovan, R. Alonso, G. A. Esquerdo, C. W. Hergenrother, and R. P. Stefanik. Mass and radius determinations for five transiting m-dwarf stars. *The Astrophysical Journal*, 701(1):764, 2009. URL <http://stacks.iop.org/0004-637X/701/i=1/a=764>.
- [20] B. Hale. *Astronomy Methods*. Cambridge University Press, Cambridge, UK, third printing, 2007 edition, 2004.
- [21] R. W. Hilditch. *An introduction to close binary stars*. Cambridge University Press, Cambridge, UK, 2001.
- [22] J. B. Holberg, T. D. Oswalt, and M. A. Barstow. Observational Constraints on the Degenerate Mass-Radius Relation. 2012.
- [23] N. Ivanova, S. Justham, X. Chen, O. De Marco, C. Fryer, et al. Common Envelope Evolution: Where we stand and how we can move forward. 2012.
- [24] L. Kaltenegger and W. Traub. Transits of Earth-Like Planets. *Astrophys.J.*, 698:519–527, 2009. doi: 10.1088/0004-637X/698/1/519.
- [25] S. Kepler, S. Kleinman, A. Nitta, D. Koester, B. Castanheira, et al. White Dwarf Mass Distribution in the SDSS. *Mon.Not.Roy.Astron.Soc.*, 375:1315–1324, 2007. doi: 10.1111/j.1365-2966.2006.11388.x.
- [26] J. D. Kirkpatrick, T. J. Henry, and D. W. McCarthy, Jr. A standard stellar spectral sequence in the red/near-infrared - Classes K5 to M9. *ApJ*, 77:417–440, nov 1991. doi: 10.1086/191611.
- [27] C. Knigge. The Evolution of Cataclysmic Variables. 2011.

- [28] C. Knigge, I. Baraffe, and J. Patterson. The Evolution of Cataclysmic Variables as Revealed by their Donor Stars. *Astrophys.J.Suppl.*, 194:28, 2011. doi: 10.1088/0067-0049/194/2/28.
- [29] D. Koester, R. Napiwotzki, N. Christlieb, H. Drechsel, H.-J. Hagen, U. Heber, D. Homeier, C. Karl, B. Leibundgut, S. Moehler, G. Nelemans, E.-M. Pauli, D. Reimers, A. Renzini, and L. Yungelson. High-resolution UVES/VLT spectra of white dwarfs observed for the ESO SN Ia progenitor survey (SPY). I. *A&A*, 378:556–568, Nov. 2001. doi: 10.1051/0004-6361:20011235.
- [30] A. L. Kraus, R. A. Tucker, M. I. Thompson, E. R. Craine, and L. A. Hillenbrand. The Mass-Radius(-Rotation?) Relation for Low-Mass Stars. *Astrophys.J.*, 728:48, 2011. doi: 10.1088/0004-637X/728/1/48.
- [31] F. E. Lara and M. Rieutord. Gravity Darkening in Binary Stars. 2012.
- [32] N. M. Law, S. R. Kulkarni, R. G. Dekany, E. Ofek, R. Quimby, et al. The Palomar Transient Factory: System Overview, Performance and First Results. 2009.
- [33] S. Lepine. Nearby stars from the LSPM-North Proper Motion Catalog. 1. Main sequence dwarfs and giants within 33 parsecs of the Sun. *Astron.J.*, 130:1680–1692, 2005. doi: 10.1086/432792.
- [34] J. Liebert, P. A. Young, D. Arnett, J. Holberg, and K. A. Williams. The Age and progenitor mass of Sirius B. *Astrophys.J.*, 630:L69–L72, 2005. doi: 10.1086/462419.
- [35] T. R. Marsh. A Guide to the Reduction of ULTRACAM data, 2006. URL <http://deneb.astro.warwick.ac.uk/phsaap/software/ultracam/html/>.
- [36] P. Massey. A User’s Guide to CCD Reductions with IRAF. 1997.
- [37] P. Massey, F. Valdes, and J. Barnes. A User’s Guide to Reducing Slit Spectra with IRAF. 1992.

- [38] J. C. Morales, I. Ribas, C. Jordi, G. Torres, J. Gallardo, E. F. Guinan, D. Charbonneau, M. Wolf, D. W. Latham, G. Anglada-Escudé, D. H. Bradstreet, M. E. Everett, F. T. O'Donovan, G. Mandushev, and R. D. Mathieu. Absolute Properties of the Low-Mass Eclipsing Binary CM Draconis. *ApJ*, 691:1400–1411, Feb. 2009. doi: 10.1088/0004-637X/691/2/1400.
- [39] P. S. Muirhead, A. Vanderburg, A. Shporer, J. Becker, J. J. Swift, et al. Characterizing the Cool KOIs. V. KOI-256: A Mutually Eclipsing Post-Common Envelope Binary. *Astrophys.J.*, 767:111, 2013. doi: 10.1088/0004-637X/767/2/111.
- [40] NED. Ned coordinate & extinction calculator results.
- [41] K. Nomoto, F.-K. Thielemann, and J. C. Wheeler. Explosive nucleosynthesis and Type I supernovae. *ApJ*, 279:L23–L26, Apr. 1984. doi: 10.1086/184247.
- [42] Oke, J.B. and Gunn, J.E. An Efficient Low Resolution and Moderate Resolution Spectrograph for the Hale Telescope. *Publications of the Astronomical Society of the Pacific*, 94:586, June 1982. doi: 10.1086/131027.
- [43] B. Paczyński. Evolutionary Processes in Close Binary Systems. *ARA&A*, 9: 183, 1971. doi: 10.1146/annurev.aa.09.090171.001151.
- [44] J. A. Panei, L. G. Althaus, and O. G. Benvenuto. Mass-radius relations for white dwarf stars of different internal compositions. *A&A*, 353:970–977, Jan. 2000.
- [45] S. Parsons, T. Marsh, C. Copperwheat, V. Dhillon, S. Littlefair, et al. Orbital Period Variations in Eclipsing Post Common Envelope Binaries. 2010.
- [46] S. G. Parsons, T. R. Marsh, C. M. Copperwheat, V. S. Dhillon, S. P. Littlefair, et al. Precise mass and radius values for the white dwarf and low mass M dwarf in the pre-cataclysmic binary NN Serpentis. 2009.
- [47] A. J. Pickles. A Stellar Spectral Flux Library: 1150–25000 Å. *PASP*, 110: 863–878, July 1998. doi: 10.1086/316197.

- [48] M. Politano. Theoretical Statistics of Zero-Age Cataclysmic Variables. *ApJ*, 465:338, July 1996. doi: 10.1086/177423.
- [49] D. Prialnik. *Stellar Structure and Evolution*. Cambridge University Press, Cambridge, UK, second edition, 2010 edition, 2000.
- [50] J. L. Provencal, H. L. Shipman, E. Hog, and P. Thejll. Testing the White Dwarf Mass-Radius Relation with HIPPARCOS. *ApJ*, 494:759, Feb. 1998. doi: 10.1086/305238.
- [51] S. Rappaport, F. Verbunt, and P. C. Joss. A new technique for calculations of binary stellar evolution, with application to magnetic braking. *ApJ*, 275: 713–731, Dec. 1983. doi: 10.1086/161569.
- [52] A. Rau, S. R. Kulkarni, N. M. Law, J. S. Bloom, D. Ciardi, G. S. Djorgovski, D. B. Fox, A. Gal-Yam, C. C. Grillmair, M. M. Kasliwal, P. E. Nugent, E. O. Ofek, R. M. Quimby, W. T. Reach, M. Shara, L. Bildsten, S. B. Cenko, A. J. Drake, A. V. Filippenko, D. J. Helfand, G. Helou, D. A. Howell, D. Poznanski, and M. Sullivan. Exploring the Optical Transient Sky with the Palomar Transient Factory. *PASP*, 121:1334–1351, Dec. 2009. doi: 10.1086/605911.
- [53] I. N. Reid and S. L. Hawley. *New light on dark stars : red dwarfs, low-mass stars, brown dwarfs*. 2005. doi: 10.1007/3-540-27610-6.
- [54] I. N. Reid, S. L. Hawley, and J. E. Gizis. The Palomar/MSU Nearby-Star Spectroscopic Survey. I. The Northern M Dwarfs -Bandstrengths and Kinematics. *ApJ*, 110:1838, Oct. 1995. doi: 10.1086/117655.
- [55] I. Ribas, J. Morales, C. Jordi, I. Baraffe, G. Chabrier, et al. Fundamental properties of low-mass stars. *Mem.Soc.Ast.It.*, 79:562–568, 2008.
- [56] E. F. Schlafly and D. P. Finkbeiner. Measuring Reddening with Sloan Digital Sky Survey Stellar Spectra and Recalibrating SFD. *ApJ*, 737:103, Aug. 2011. doi: 10.1088/0004-637X/737/2/103.
- [57] SDSS. Sdss: Flux calibration.

- [58] H. L. Shipman. Masses and radii of white-dwarf stars. III - Results for 110 hydrogen-rich and 28 helium-rich stars. *ApJ*, 228:240–256, Feb. 1979. doi: 10.1086/156841.
- [59] J. A. Smith, D. L. Tucker, S. Kent, M. W. Richmond, M. Fukugita, T. Ichikawa, S.-i. Ichikawa, A. M. Jorgensen, A. Uomoto, J. E. Gunn, M. Hamabe, M. Watanabe, A. Tolea, A. Henden, J. Annis, J. R. Pier, T. A. McKay, J. Brinkmann, B. Chen, J. Holtzman, K. Shimasaku, and D. G. York. The u'g'r'i'z' Standard-Star System. *aj*, 123:2121–2144, Apr. 2002. doi: 10.1086/339311.
- [60] R. F. Stellingwerf. Period determination using phase dispersion minimization. *ApJ*, 224:953–960, Sept. 1978. doi: 10.1086/156444.
- [61] E. van den Besselaar. *White Dwarf - Red Dwarf Binaries in the Galaxy*. PhD thesis, Department of Astrophysics, Radboud University Nijmegen, 2007.
- [62] E. van den Besselaar, R. Greimel, L. Morales-Rueda, G. Nelemans, J. Thorstensen, et al. DE CVn: A bright, eclipsing red dwarf-white dwarf binary. *Astron.Astrophys.*, 466:1031, 2007. doi: 10.1051/0004-6361:20066246.
- [63] F. van der Hooft, P. J. Groot, T. Shahbaz, T. Augusteijn, J. Casares, S. Dieters, J. Greenhill, K. Hill, L. H. A. Scheers, R. M. Naber, J. A. de Jong, P. A. Charles, and J. van Paradijs. The black hole transient Nova Scorpii 1994 (=GRO J1655-40): orbital ephemeris and optical light curve. *MNRAS*, 286:L43–L49, Apr. 1997.
- [64] M. van der Sluys. Kleur-magnitude-diagram voor nabije sterren, 2013. URL <http://hemel.waarnemen.com/Informatie/Sterren/cmd.html>.
- [65] P. G. van Dokkum. Cosmic-ray rejection by Laplacian edge detection. *Publ.Astron.Soc.Pac.*, 113:1420–1427, 2001. doi: 10.1086/323894.
- [66] K. Verbeek. Evolved stars in the Galactic Plane surveys. 2013. doi: 10.1086/510240.

- [67] F. Verbunt. On the implications of the period distributions of subclasses of cataclysmic variables. *MNRAS*, 290:L55–L58, Sept. 1997.
- [68] F. Verbunt and S. Rappaport. Mass transfer instabilities due to angular momentum flows in close binaries. *ApJ*, 332:193–198, Sept. 1988. doi: 10.1086/166645.
- [69] D. B. Wood. Theoretical Basis for Analytical Solution of Eclipsing Binary Light Curves. *International Amateur-Professional Photoelectric Photometry Communications*, 12:7, June 1983.
- [70] S. Zucker, T. Mazeh, and T. Alexander. Beaming Binaries - a New Observational Category of Photometric Binary Stars. 2007.